Raman Studies of 2-Dimensional van der Waals Materials

By:

Robert Christopher Schofield

The University of Sheffield

Faculty of Science

Department of Physics and Astronomy

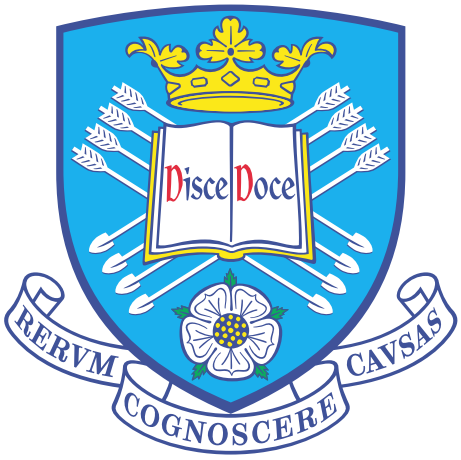

A thesis submitted in partial fulfilment of the requirements for the degree of:

Doctor of Philosophy

Submission date:

February 2018

Dedication

For the love of my parents; Maggie & Peter ...

Abstract

Raman Studies of 2-Dimensional van der Waals Materials

Robert Christopher Schofield

Presented herein are results of optical studies with emphasis on the Raman response, providing significant contribution to the knowledge of the field. In $Mo_xW_{(1-x)}S_2$, confirmation of the behaviour of the excitonic properties is made. Raman measurements performed in this system allow investigation with unprecedented resolution, highlighting deviations in the high frequency A_{1g} optical phonon mode from theoretical predictions, and previous experimental studies. In the low frequency, data confirms the trends in the shear and breathing interlayer modes in alloys between WS_2 and MoS_2 are well described by the modification in the square density. Resonant excitation for [Mo] < 0.4, highlights new evidence for the understanding of the hitherto unexplained 'Peak X' resonant feature. Diverse indium-selenium compounds isolated by novel means are studied. The ULF Raman modes of PDMS exfoliated InSe are documented for the first time, demonstrating the ε-phase with ABA stacking, with flake of thickness N manifesting $(N-1)$ shear modes owing to resonant excitation of few layer samples. InSe flakes encapsulated in hexagonal boron nitride manifest different stacking orders to those of PDMS exfoliated InSe, and were found to have significant contamination, with crystalline degradation of the monolayer flake, and peaks corresponding N_2 & O_2 rotational modes present. In_2Se_3 films grown epitaxially on GaSe display substrate-selective polymorphism, where α-, β-, & γ- phases are identified, in addition to regions of InSe. Laser photo-annealing is shown to drive a phase change from the groundstate $\beta \rightarrow \alpha$ phase, which is against the thermodynamic gradient. $MoSe_2/WS_2$ twisted hetero-bi-layer structures are studied, where shear modes showing a linear softening from AA$'$ stacking towards the AB at 60° indicating reduced interlayer coupling, as expected from the difference in interlayer spacing of AA$'$ and AB ordering. High frequency modes in the heterobilayer also demonstrate some sensitivity in the relative angle, and are analysed in detail.

Acknowledgements

I have been benefitted by a great number of people over the course of my academic studies, here I wish to recognise their contribution, and emphasise my great thanks.

My primary thanks goes to my supervisor, Professor Alexander Tartakovskii *aka* Sasha, or 'Big Sasha'. His excitement for 2D materials, and his skill in communicating their importance and early results, has allowed the rapid growth of the 2D materials sub-group in Sheffield, to which it has been a pleasure to contribute. His enthusiasm has harboured many fruitful collaborations to develop the group's research, and through his efforts, many of the samples I worked with were procured. In the times where I was concerned for the progress of my work, or for the prospects in my scheduled, Sasha provided clarity in the goals and expressed a confidence which kept me going through the times that I struggled. Professor Maurice Skolnick, the principal investigator of the Low Dimensional Structures and Devices (LDSD) group has provided an environment in which all members are welcomed and encouraged, with an excellent spirit of collaboration among its members.

I wish to thank the - now numerous - 2D materials sub-group members who we affectionately refer to as 'Team 2D'. In reverse illogical order [1] they are:

Dr. Tillmann Godde (*Tilly*), who joined Team 2D the very same week that I did, is a skilled experimentalist with a wide range of expertise; he assisted me in the design and building of my ultra low frequency Raman system, which was the basis for my work. His home-made positional stage controllers, 3D printed enclosures, and *LabVIEW*, were crucial in the implementation of the system. His direct manner was always a quality I enjoyed, and led to many discussions on a wide range of topics which I shall always value. In my 5 week collaboration in Dortmund, he couriered my luggage and the samples by plane so that I could cycle the journey from Sheffield, which allowed me to arrive excited and refreshed ready for the scheduled experiments.

Dr. Stefan Schwarz (*Big Ste*), who welcomed me to Sheffield for my interview, and was a full embodiment of the talent and kindness present in the LDSD group. His encouragement and assistance allowed me to attempt measurements to observe the Higgs-mode in exfoliated 2H-$NbSe_2$ due to the coupling of superconducting and charge density wave phonons, although fruitless, those were four of the most exciting weeks of my PhD.

Messrs Alessandro Catanzaro & Daniel Gillard (*Gilly*) who together produced a gamut of

[1] no particular order, for those who look grave at a pun [2]

[2] a line from Lewis Carroll's *'The Hunting of the Snark'*

samples for me to measure, and did so whilst under considerable workloads. Dr. Osvaldo del Pozo Zamudio (*Ozzy*) who allowed me to assist in the lab for his measurments, and from whom I learned a great deal. Dr. Daniel Sercombe, who I met only briefly, but who was immediate in his encouragement, and his willingness to share his knowledge. Dr. Scott Dufferwiel & Tom Lyons who produced excellent experimental works toward which the whole group aspires. Dr. Evgeny Alexeev, who's arrival in Team 2D marked a point where serious efforts in sample fabrication could be made, and the productivity of the group was enhanced. Oleksandr Skrypka (affectionately *Little Sasha*) who's dedication to the work of the group, and his careful experimental work was much admired. Luca Sortino and Panaiot Zotev, a dynamic duo who have made C18 their own, and whose progress I look forward to following.

The wider LDSD group has been a hospitable place, and in particular I'd like to thank Andrew Foster & John O'Hara (like the rum) for their companionship.

My collaborators who have graced me with samples and interesting discussions have been a great boon to my work, especially; Nilanthy Balakrishan who made the In_2Se_3 on GaSe sample, and Matthew Hamer, who made the h-BN Encapsulated InSe samples, and both of whom joined me in the lab for some of the measurements.

The people of the physics department cryo-plant; Chris Vickers and Phil M'dewar demonstrate a professionalism that allows not only the work of the LDSD group, but also that of the SQUID. The staff of the central workshop, especially Paul Kemp-Russell who produce such elegant solutions, and provide consultation in the design for parts of many of Team 2D's laboratory set-ups.

At at TU Dortmund I wish to express gratitude to Professor Manfred Bayer for facilitating my stay, and providing an exciting environment in which to work. My lab mates there were Dennis Kudlacik, and Philipp Waldkirch; together, under the supervision of Jörg Debus, we made a solid effort in searching for spin flips in MoS_2 monolayers on h-BN.

The members of Sheffield University Rowing Club express a unique quality which I had not previously experienced, and as such they have been a refreshing presence, and I have been proud to have served on their committee. In particular, to Louis 'Desttroyer' Fox for his encouragement and sympathy with all my efforts; many fangs.

To Miss Primrose Kate Wilkins for her enabling presence, and a for love I will not forget, thank you.

My parents have supported me unconditionally, and from an early age, gave me the passion for thought and knowledge, which I value to my core.

RCS

Contents

List of Figures

List of Tables

Part I

Preliminaries

Chapter 1

Introduction

With the publishing of Andre Geim and Konstantin Novoselov's 2004 paper 'Electric Field Effect in Atomically Thin Carbon Films' [1], there came a concerted global effort in research into graphene and, soon after, the exploration of other families of planar van der Waals (vdW) materials, particularly the transition metal chalcogenides (TMCs). The impact of Geim and Novoselov's work in establishing a novel field of condensed matter physics was recognised in the awarding of the 2010 Nobel prize:

> For groundbreaking experiments regarding the two-dimensional material graphene.

The Nobel lecture given by Geim [2] and the 2007 review [3] highlight the remarkable stability of single layer materials, widely believed to be thermodynamically unstable due to their high surface-area to volume ratio. Another noteworthy point regards the previous occasions that single layers have been isolated and observed without the consideration and further study the laureates gave the material, indeed, in addition to the observations mentioned in refs. [2], [3], Bob Frindt produced by various methods few and single layers of the TMDs molybdenum disulphide [4], [5] and niobium disulphide [6], performing optical spectroscopy on the resulting flakes without the work attracting the interest that recent work has gathered, most likely due to the lack of facile, high throughput optical systems and other techniques that allow studies at the nanoscale as are widely available in the current time.

Since the seeding of the 2D material field, a diverse range of properties have been identified in planar vdW materials; from insulating hexagonal boron nitride (h-BN); tunable semimetal graphene (Gr); the gamut of semiconducting TMCs; to the more exotic phenomena of charge density waves and superconductivity in Niobium and Tantalum Diselenide. Together, due to the unique vdW coupling of layers the fabrication of vertical heterostructure devices for exploration of the physics relevant to next-generation technologies is possible.

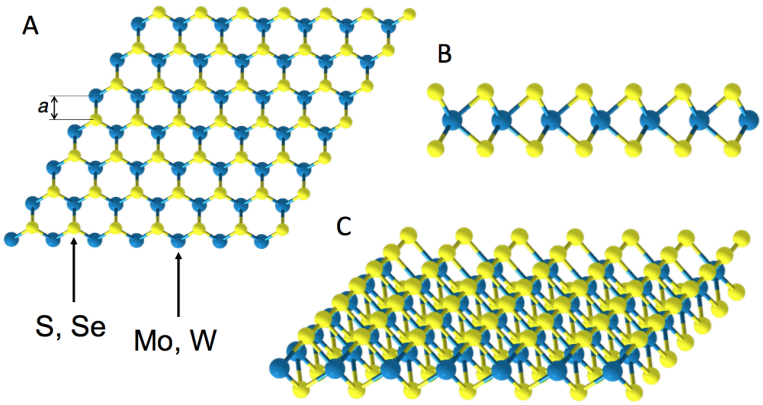

Figure 1.1: A multiview ball-and-stick model of a molecular mono-layer transition metal dichalgogenide material in the typical trigonal prismatic polymorph viewed in; A, plan; B, cross section; and C, in 3D. The blue spheres are metal atoms, molybdenum, tungsten, and the yellow spheres chalcogen atoms, sulphur, selenium, tellurium. Illustration courtesy of Osvaldo Del Pozo Zamudio.

The issue of scalability remains a major barrier to the long term success of the 2D material field delivering technologically significant results. The development of growth techniques to produce wafer scale monolayers of materials is a growing research area with critical materials such as BN, Gr, MoS_2 and WS_2 now capable of manufacture, whilst work on III–VI materials including InSe is beginning to yield results [7]–[9]. Characterisation of the physical phenomena present in these materials is important to improve the growth procedures and to build larger scale devices in a deterministic manner.

1.1 Two Dimensional Transition Metal Chalcogenide Materials

Transition metal chalcogenides in the 2D limit came to prominence with the discovery of an indirect to direct bandgap transition in the semiconductor MoS_2 in 2010 [10], with the same realisations in the materials WS_2, $MoSe_2$, and WSe_2. More exotic phenomena such as: superconductivity in bulk $NbSe_2$ [6], $TaSe_2$ [11]; charge density waves in bulk & monolayer $NbSe_2$ [12], $TiSe_2$ [13], [14]: and type-II Weyl semimetals in $MoTe_2$ [15], WTe_2 [16] have been observed.

This class of materials takes the structure shown in figure 1.1 with the molecular layers structured with chalcogens; X∈[sulphur, selenium, tellurium, ...], and transition metals M∈[molybdenum, tungsten, niobium, tantalum, ...], arranged as X–M–X. They have previously been studied in detail in bulk for their tribological and semiconducting properties, and their bulk forms are well characterised [17].

The presence of the indirect–direct bandgap transition in the monolayer limit allows exploration of the possibility of atomically perfect quantum wells and heterostructures in which optoelectronic effects can be investigated – with the prospect of novel, and superior technologies

to those available with present condensed matter material systems. The large exciton binding energies in molybdenum and tungsten dichalcogenides of (0.5–1) eV, and the corresponding exciton Bohr radius $\alpha_B \approx 1$ nm [18]–[21] make them ideal candidates to attempt room temperature Bose–Einstein condensation of exciton–polaritons. Furthermore, the broken inversion symmetry in the monolayer results in degeneracy in the K valleys, which is lifted by spin-orbit coupling, producing chiral optical selection rules for interband transitions at K and K′. The consequence of this is that for a carrier in one K valley to undergo a spin flip it would have to scatter between valleys, or undergo an energetically unfavourable transition: This spin-valley locking represents a new means to encode or process data.

1.2 Indium Selenide

The III–VI material InSe offers an alternative route to optoelectronic devices to the TMDs – in contrast to those materials, InSe is a direct bandgap semiconductor in bulk form, becoming an indirect bandgap material with emergence of a 'Mexican hat' energy dispersion for the valence band as the thickness approaches the mono-layer limit [22], [23]. This relaxes the requirement in TMDs of mono-layer flakes in order to yield useful optical properties for optoelectronic devices. In fact, the direct bandgap nature of the bulk InSe material allows facile tuning of the optical bandgap transition through control of the quantum confinement due to the material's thickness [24].

The choice of Indium Selenide in this work is partly due to the relatively high stability as compared to other III–VI materials [25]. As compared to MoS_2, InSe has smaller electron effective mass ($m_\star = 0.143\ m_0$) and shows higher mobility, $\mu \approx 103\ cm^2V^{-1}s^{-1}$ versus $m^\star = 0.45\ m_0$ and a range of $50 < \mu < 200\ cm^2V^{-1}s^{-1}$ [26]. Thus, InSe may be useful in fast, high performance electronics where TMDs have proved undesirable. Another prospect that III–VI materials hold is that of the possibility of nanoscale non-linear optoelectronics, due to non-linear optical response and strong second harmonic generation. Indeed, observation has been made of the interplay between bulk and surface nonlinearities in few-layer flakes of InSe [27], and GaSe [28].

Useful, high performance few-layered InSe photodetectors with broad spectral response have been demonstrated on rigid substrates [29], and bendable susbtrates [30].

Presently, there exists no systematic study of the Raman modes of InSe, which should exist in order to properly characterise InSe heterostructure devices and improve their fabrication.

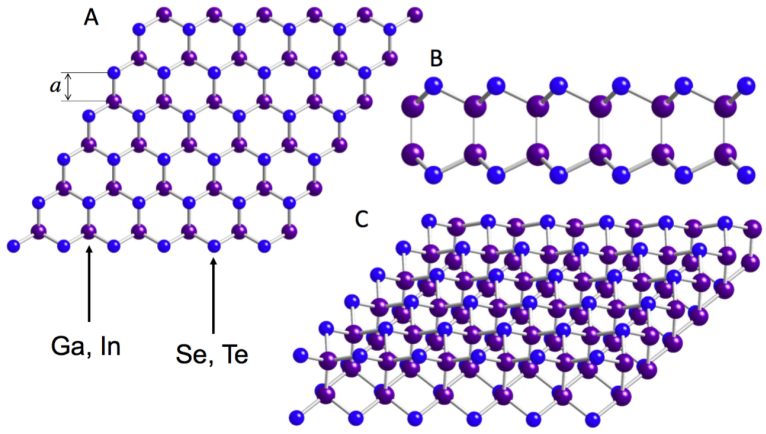

Figure 1.2: A multiview ball-and-stick models of an α-phase molecular mono-layer III–VI material viewed in; A, plan; B, cross section; and C, in 3D. Purple spheres represent metal atoms; indium, gallium, and the blue spheres chalcogen atoms, sulphur, selenium, tellurium. Illustration courtesy of Osvaldo Del Pozo Zamudio.

1.3 Chemical Growth of 2 Dimensional Transition Metal Chalcogenide Materials

Even before the isolation of mono-layers of van der Waals materials, from 1958 TMDs had attracted interest from researchers for the range of properties that they exhibited, particularly their solid-lubricant nature [31].

First studies were made on Molybdenite – naturally occurring molybdenum disulphide crystals – which is the most abundant source of molybdenum in the Earth's crust [32]. Not all metal chalcogenides occur as auspiciously as MoS_2 and must be synthesised chemically; Sn- and Ge-based chalcogenides were the first to be grown from molten compounds using Czochralski, Kyropoulos and Bridgman methods [33].

These techniques, however, were unfeasible for the growth of transition metal chalcogenides: In response, chemical vapour methods were developed, whereby elemental precursors are evaporated, reacting in vapour phase before and condensing in a low temperature region of a closed quartz furnace tube [34]. By this method chemical growth allows the tuning of TMD properties, through the process of alloying, to yield properties intermediate to the values of the pure materials e.g. $Nb_xTa_{(1-x)}Se_2$ [35], $MoS_{2x}Se_{2(1-x)}$ [36], $Mo_xW_{(1-x)}Se_2$ [37], $Mo_xW_{(1-x)}S_{2y}Se_{2(1-y)}$ [38].

Following the 2D material field's inception the topic has captured the interest of a large portion of the scientific community, besides the pioneering physicists; both materials scientists and chemists have been drawn to the challenge of finding the methods required to deliver the promise of the materials to society, they found that by many of the methods described for the

production of bulk samples, adaptations in the procedures could be adapted to yield monolayer and heterostructure growth of 2D materials.

A summary of methods for growing TMDs in the 2D limit that have been explored are as follows:

- High temperature annealing of both dip and spin coated, thermally decomposed ammonium thiomolybdate layer in the presence of sulphur, on SiO_2 substrates [39], [40].
- Reaction of vapour phase MoO_3 with sulphur evaporated in an N_2 flow, SiO_2 substrates. [41]
- Reaction of vapour phase $MoCl_3$ with sulphur evaporated in an N_2 flow, SiO_2 substrates. [42]
- Sulphurisation of WO_3 pre-evaporated on to SiO_2 substrates [43].
- Sulphurisation of tungsten films fabricated using atomic layer deposition [44].
- Direct evaporation of MoS_2 powders on to SiO_2, quartz, and glass substrates. [45]
- Vapour phase reaction of MoO_3 with Sulphur in an argon flow reacting at a SiO_2/S target with W from a W/Te mixture resulting in growth of lateral and vertical heterojunctions, as controlled by the furnace temperature [46].
- Sulphurisation of thermally deposited 1 nm WO_3 on 1 nm MoO_3 to produce $Mo_xW_{(1-x)}S_2$ alloy films [47].

Though it is clear that the parameter space in which to find the most favourable thermodynamic conditions is large, and presents a considerable task, the work above is delivering results on which 2D material technology can be built.

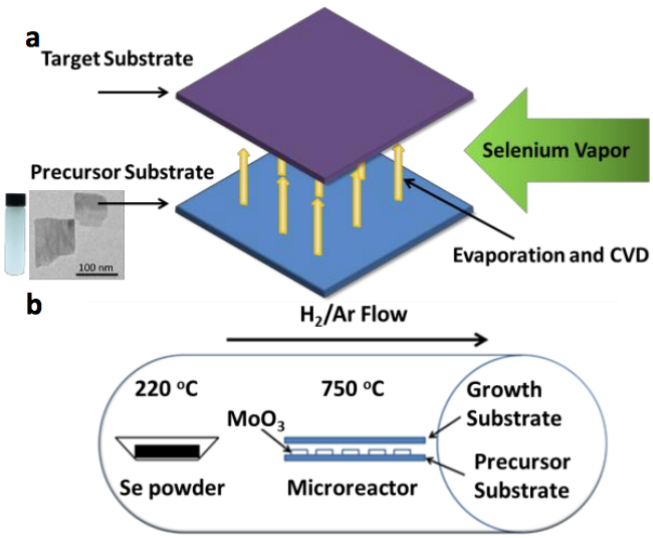

Figure 1.3: The furnace design of the Duisberg group, a design typical of those used throughout the research field. [48]

1.4 van der Waals Heterostructures

The nature of layered van der Waals materials allows not only the isolation of single atomic or molecular layers of the materials, but also the possibility to artificially stack materials, allowing the synthesis of novel structures with atomic abruptness at interfaces. The ideal, as illustrated in figure 1.4, represents a goal towards which researchers can aspire, though the reality poses numerous challenges:

- Firstly, the selection of materials is limited to those which may be isolated by means of the current technology; inert atmosphere gloveboxes offer the current state of the art with ultra high vacuum manipulation systems in development. Reliably, Graphene, hexagonal Boron Nitride, and the majority of chalcogenide materials can be isolated in such systems, and various electronic, optoelectronic, and experimental structures of these materials have been produced.
- Second, unlike the illustration in figure 1.4, the stacking of layers does not produce entire devices of perfect inter-facial contact, any crystals subjected to ambient conditions adsorb chemical species from the environment; water, hydrocarbons, and adhesive residues all present a threat to the homogeneity of 2D material heterostructures. Remarkably, however, the vdW interfaces demonstrate a 'self-cleaning' effect, where contaminants are aggregated into discreet, bubble like regions, leaving μm scale regions of atomically pristine interface [49]–[51].

Another attraction of vdW coupled materials is the relaxing of the epitaxial constraint for interfacing layers, allowing the use of materials with differences in lattice constants, again this assumption is somewhat naive: The coupling between neighbouring materials induces moiré patters of strain, and differing stacking orders [52].

An additional degree of freedom in the fabrication of 2D material hetrerostructures is the relative angles of the constituent crystals; devices with small deviations from perfect alignment can have dramatically different properties to those which are aligned. CVD techniques are able to yield perfect stacking of hetero-bilayers, and Graphene on hBN is able to undergo 'macroscopic self-reorientation' spontaneously aligning the two materials [53].

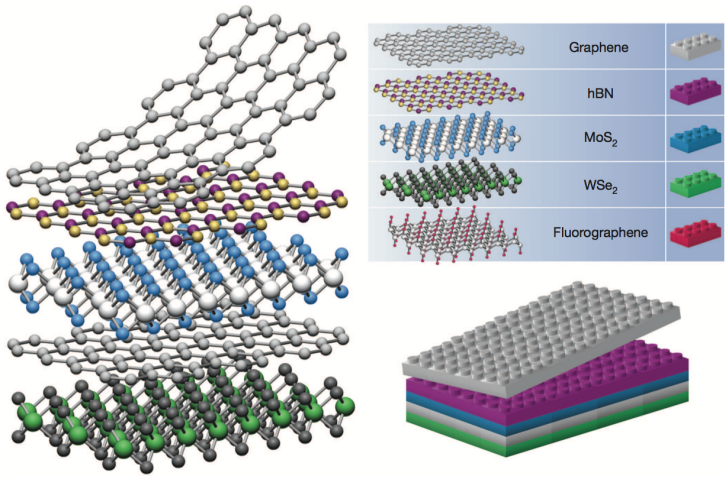

Figure 1.4: An illustration of the van der Waals epitaxy between different 2D materials combined into a heterostructure, an analogy is made with the LEGO building system. From ref. [54].

In 2D material heterostructures the coupling between layers is an important factor in determining the function and utility of the resulting device: Significant work has been undertaken in order to characterise the interactions between mechanically transferred and chemically grown 2D material interfaces, from optical dark field microscopy, cross sectional HAADF STEM analysis [55], to ultra low frequency Raman spectroscopy and PL. There needs to be continued work in this area to ensure consistent device characteristics and the provision of an effective quality control method.

1.5 Ultra Low Frequency Raman Microscopy

Raman spectroscopy is a versatile tool for investigating chemical and crystal structures. Loosely, a Raman spectrum, collected as the inelastically scattered light from a high intensity, monochromatic source represents the density of states of the vibrational modes of a structure. As such, it allows the probing of the purity, crystallinity [56], strains [57], [58], structural phase changes [59], or any other lattice phonon coupled excitation [60]. A particular advantage of the Raman technique is its applicability to a diverse range of materials, from molecular gasses through to solids of all kinds.

In layered materials such as 2D vdW materials there exists a set of low frequency lattice vibrations which correspond to interlayer vibrations, that have a strong dependence to properties such as sample thickness, and interfacial coupling [61].

Whilst Raman spectroscopy has existed as an experimental technique since 1928, the observation of the secondarily scattered light close to the Rayleigh line remained a challenge for a considerable time following [62].

1.5.1 Novel Rayleigh Rejection Technology

Besides the use of low throughput, high-cost triple spectrometer, recent technologies have emerged to enable facile observation of Raman lines down to 5 cm^{-1}. These technologies rely on producing very high-Q distributed Bragg reflectors to exclude Rayleigh scattered light, and transmit the Raman scattered signal.

The filters are produced in photo-thermo-reflective (PTR) glass, Na_2O-ZnO-Al_2O_3-SiO_2 glass doped with silver (Ag), cerium (Ce), and fluorine (F), the refractive index of the glass is modulated by the growth of NaF crystals after following steps [63]:

First Photo exciting Ce^{3+} ions to Ce^{4+} using near UV light, the extra electron neutralises the Ag^- ions.

Second The latent volume hologram is recorded in the glass by modulation of the density of Ag atoms by varying the dosage of EM radiation.

Third The Ag atoms are precipitated out by temperatures greater than 450°C.

Fourth At temperatures above 500°C NaF crystals nucleate about the Ag atoms, locally modifying the refractive index.

By this method it is possible to produce filters having more than 10^4 periods, yielding notch widths of 10's of picometers.

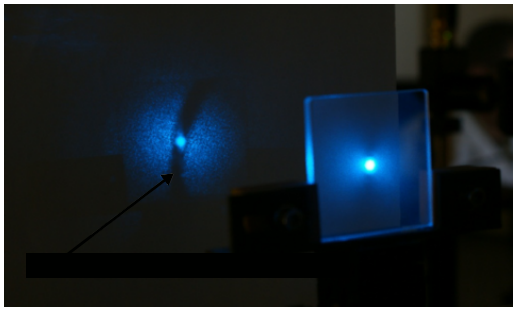

(a) The Bragg condition visible as a dark band though the laser speckle on the screen.

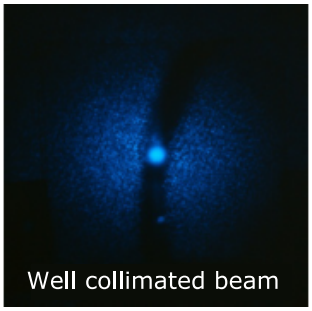

(b) Note the wide Bragg band

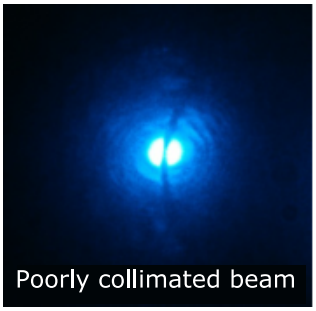

(c) Here the Bragg condition is less clear.

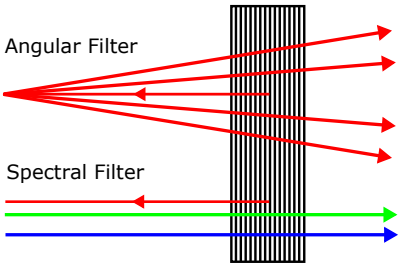

(d) The Bragg filter is bi-conditional.

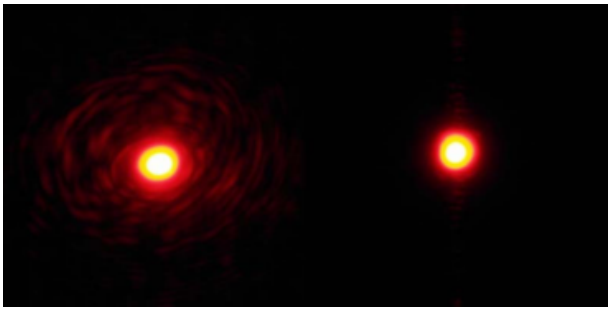

(e) Spatial and angular filtering of a laser beam.

Figure 1.5: Demonstrations of Bragg gratings properties. (Optigrate Corp.)

The Bragg condition may be satisfied by a range of wavelengths, at different angles, this gives rise to the curved rejection-band when the incident wavelength doesn't perfectly match the normal Bragg condition, this is a manifestation of the Ewald Sphere. In practice the filters are used in series, with each providing an optical density of 3 where the Bragg condition is met, each filter is mounted in a kinematic mount and its angle tuned to reject the Rayleigh scatter as much as possible.

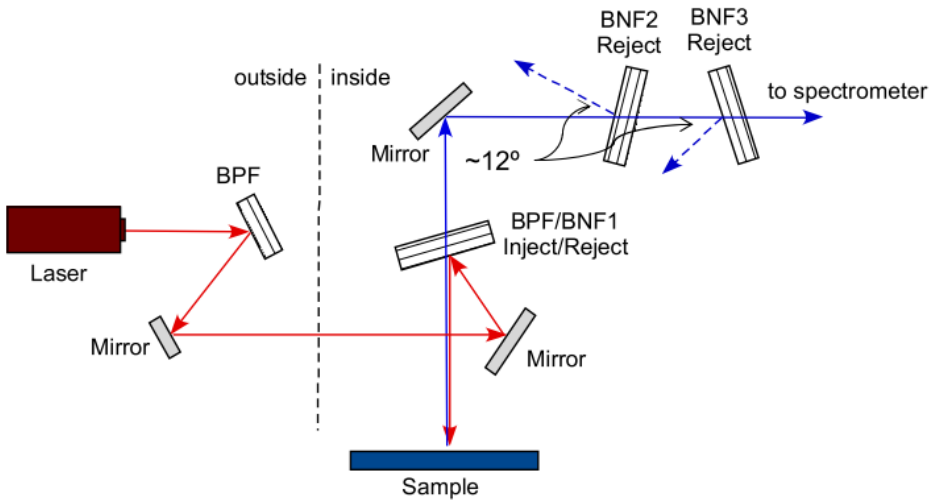

Figure 1.6: An ideal ULF Raman set-up, for use with a single stage spectrometer. (Optigrate Corp.)

The Bragg notch filters (BNFs), as described above, were implemented in the μPL set-up, with a Bragg pass filter (BPF) used to clean a 532 nm wavelength, 1 MHz, 0.1 pm linewidth diode-pumped-solid-state laser, aligned into the excitation path. In the collection arm, immediately preceding the spectrometer focussing lens, three BNFs were used to reject the Rayleigh scattered light with an effective optical density of 9. Without building a dedicated set up, as detailed in figure 1.6, or applying a screen to remove laser scatter from mirrors, and neutral density filters, the performance of the system is limited.

1.6 Thesis Structure

This work is split into two parts, the first part, I: Preliminaries, offers a chapter 1 which serves to introduce the reader to the topics required to appreciated the context in which the experimental work was conducted. In the following chapter the optics of transition metal chalcogenides is discussed including sections for excitonic properties, 2.1, and the Raman effect, 2.2. The final chapter 3 for the first part is a description of the experimental techniques, discussing optical spectroscopic techniques for detection of the Raman effect 3.1.1, and Photoluminescence 3.1.2.

The second part II: Results of Experimental Studies, where the main work achieved over the course of study is presented in the following chapters:

- 4, Raman Studies of $Mo_xW_{(1-x)}S_2$ Alloys
- 5 Raman Studies of Indium Selenide
- 6, Raman Studies of Twisted $MoSe_2/WS_2$ Heterobilayers.

Finally, conclusion is made, with a perspective on the results and the outlook for future work in the field of ultra-low-frequency Raman spectroscopy on 2D materials.

References

[1] K. S. Novoselov, A. K. Geim, S. V. Morozov, D. Jiang, Y. Zhang, S. V. Dubonos, I. V. Grigorieva, and A. A. Firsov, "Electric field effect in atomically thin carbon films.," *Science*, vol. 306, no. 5696, pp. 666–669, 2004, ISSN: 1095-9203. DOI: 10.1126/science.1102896. arXiv: 0410550 [cond-mat]. [Online]. Available: http://ieeexplore.ieee.org/xpls/abs%7B%5C_%7Dall.jsp?arnumber=6594127%20http://www.sciencemag.org/content/306/5696/666.short%20http://arxiv.org/abs/cond-mat/0410550.

[2] A. K. Geim, "Random walk to graphene," *International Journal of Modern Physics B*, vol. 25, no. 30, pp. 4055–4080, 2011. [Online]. Available: http://www.worldscientific.com/doi/pdf/10.1142/S0217979211059097.

[3] A. K. Geim and K. S. Novoselov, "The rise of graphene," *Nature Materials*, vol. 6, no. 3, pp. 183–191, Mar. 2007, ISSN: 1476-1122. DOI: 10.1038/nmat1849. arXiv: 0702595 [cond-mat]. [Online]. Available: http://www.nature.com/nmat/journal/v6/n3/abs/nmat1849.html%20http://www.nature.com/doifinder/10.1038/nmat1849.

[4] R. F. Frindt, "Optical Absorption of a Few Unit-Cell Layers of MoS2," *Physical Review*, vol. 140, no. 2A, pp. 1962–1965, 1965, ISSN: 0031899X. DOI: 10.1103/PhysRev.140.A536. [Online]. Available: http://prola.aps.org/abstract/PR/v140/i2A/pA536%7B%5C_%7D1.

[5] P. Joensen, R. F. Frindt, and S. R. Morrison, "Single layer MoS2," *Materials Research Bulletin*, vol. 21, no. 4, pp. 457–461, Apr. 1986, ISSN: 0025-5408. DOI: 10.1016/0025-5408(86)90011-5. [Online]. Available: http://linkinghub.elsevier.com/retrieve/pii/0025540886900115.

[6] R. F. Frindt, *Superconductivity in Ultrathin NbSe_{2} Layers*, 1972. DOI: 10.1103/PhysRevLett.28.299. [Online]. Available: http://prl.aps.org/abstract/PRL/v28/i5/p299%7B%5C_%7D1%20http://journals.aps.org/prl/abstract/10.1103/PhysRevLett.28.299.

[7] P. Rodríguez-Hernández, K. Nieto-Zepeda, A. Guillén-Cervantes, J. Santoyo-Salazar, J. Santos-Cruz, J. Arias-Cerón, M. Olvera, O. Zelaya-Ángel, G. Contreras-Puente, and F. de Moure-Flores, "Structural and optical properties of In_2S_3 thin films grown by chemical bath deposition on pet flexible substrates," *Chalcogenide Letters*, vol. 14, no. 8, pp. 331–335, 2017, ISSN: 15848663.

[8] B. J. Carey, J. Z. Ou, R. M. Clark, K. J. Berean, A. Zavabeti, A. S. R. Chesman, S. P. Russo, D. W. M. Lau, Z.-Q. Xu, Q. Bao, O. Kevehei, B. C. Gibson, M. D. Dickey, R. B. Kaner, T. Daeneke, and K. Kalantar-Zadeh, "Wafer-scale two-dimensional semiconductors from printed oxide skin of liquid metals," *Nature Communications*, vol. 8, p. 14 482, Feb. 2017, ISSN: 2041-1723. DOI: 10.1038/ncomms14482. [Online]. Available: http://www.nature.com/doifinder/10.1038/ncomms14482.

[9] A. Zavabeti, J. Z. Ou, B. J. Carey, N. Syed, R. Orrell-Trigg, E. L. H. Mayes, C. Xu, O. Kavehei, A. P. O'Mullane, R. B. Kaner, K. Kalantar-zadeh, and T. Daeneke, "A liquid metal reaction environment for the room-temperature synthesis of atomically thin metal oxides," *Science*, vol. 358, no. 6361, pp. 332–335, Oct. 2017, ISSN: 0036-8075. DOI: 10.1126/science.aao4249. [Online]. Available: http://www.sciencemag.org/lookup/doi/10.1126/science.aao4249.

[10] K. F. Mak, C. Lee, J. C. Hone, J. Shan, and T. F. Heinz, "Atomically thin MoS_2: A new direct-gap semiconductor," *Physical Review Letters*, vol. 105, no. 13, pp. 2–5, 2010, ISSN: 00319007. DOI: 10.1103/PhysRevLett.105.136805. arXiv: 1004.0546.

[11] Y. Liu, D. F. Shao, L. J. Li, W. J. Lu, X. D. Zhu, P. Tong, R. C. Xiao, L. S. Ling, C. Y. Xi, L. Pi, H. F. Tian, H. X. Yang, J. Q. Li, W. H. Song, X. B. Zhu, and Y. P. Sun, "Nature of charge density waves and superconductivity in 1T–$TaSe_{(2-X)}Te_x$," *Physical Review B*, vol. 94, no. 4, p. 045 131, Jul. 2016, ISSN: 2469-9950. DOI: 10.1103/PhysRevB.94.045131. arXiv: 1602.07983. [Online]. Available: https://link.aps.org/doi/10.1103/PhysRevB.94.045131.

[12] X. Xi, L. Zhao, Z. Wang, H. Berger, L. Forró, J. Shan, and K. F. Mak, "Strongly enhanced charge-density-wave order in monolayer $NbSe_2$," *Nature Nanotechnology*, vol. 10, no. 9, pp. 765–769, 2015, ISSN: 1748-3387. DOI: 10.1038/nnano.2015.143. [Online]. Available: http://www.nature.com/doifinder/10.1038/nnano.2015.143.

[13] P. Chen, Y.-H. Chan, X.-Y. Fang, Y. Zhang, M. Y. Chou, S.-K. Mo, Z. Hussain, A.-V. Fedorov, and T.-C. Chiang, "Charge density wave transition in single-layer titanium diselenide.," *Nature communications*, vol. 6, p. 8943, 2015, ISSN: 2041-1723. DOI: 10.1038/ncomms9943. [Online]. Available: http://www.ncbi.nlm.nih.gov/pubmed/26568512%0Ahttp://www.pubmedcentral.nih.gov/articlerender.fcgi?artid=PMC4660365.

[14] P. Goli, J. Khan, D. Wickramaratne, R. K. Lake, and A. A. Balandin, "Charge Density Waves in Exfoliated Films of van der Waals Materials: Evolution of Raman Spectrum in TiSe2," *Nano letters*, vol. 12, no. 11, pp. 5941–5, Nov. 2012, ISSN: 1530-6992. DOI: 10.1021/nl303365x. [Online]. Available: http://www.ncbi.nlm.nih.gov/pubmed/23092208.

[15] Z. Guguchia, F. Von Rohr, Z. Shermadini, A. T. Lee, S. Banerjee, A. R. Wieteska, C. A. Marianetti, B. A. Frandsen, H. Luetkens, Z. Gong, S. C. Cheung, C. Baines, A. Shengelaya, G. Taniashvili, A. N. Pasupathy, E. Morenzoni, S. J. Billinge, A. Amato, R. J. Cava, R. Khasanov, and Y. J. Uemura, "Signatures of the topological s+-superconducting order

parameter in the type-II Weyl semimetal Td-$MoTe_2$," *Nature Communications*, vol. 8, no. 1, pp. 1–8, 2017, ISSN: 20411723. DOI: 10.1038/s41467-017-01066-6. arXiv: 1704.05185. [Online]. Available: http://dx.doi.org/10.1038/s41467-017-01066-6.

[16] P. Li, Y. Wen, X. He, Q. Zhang, C. Xia, Z. M. Yu, S. A. Yang, Z. Zhu, H. N. Alshareef, and X. X. Zhang, "Evidence for topological type-II Weyl semimetal WTe2," *Nature Communications*, vol. 8, no. 1, pp. 8–15, 2017, ISSN: 20411723. DOI: 10.1038/s41467-017-02237-1. [Online]. Available: http://dx.doi.org/10.1038/s41467-017-02237-1.

[17] P. A. Young, "Lattice parameter measurements on molybdenum disulphide," *Journal of Physics D: Applied Physics*, vol. 1, no. 7, p. 416, Jul. 1968, ISSN: 00223727. DOI: 10.1088/0022-3727/1/7/416. [Online]. Available: http://stacks.iop.org/0022-3727/1/i=7/a=416?key=crossref.b36c68e5065dbbd7bc4f714aa625b3ab.

[18] A. Ramasubramaniam, "Large excitonic effects in monolayers of molybdenum and tungsten dichalcogenides," *Physical Review B - Condensed Matter and Materials Physics*, vol. 86, no. 11, pp. 1–6, 2012, ISSN: 10980121. DOI: 10.1103/PhysRevB.86.115409. arXiv: 1403.3771.

[19] H. P. Komsa and A. V. Krasheninnikov, "Effects of confinement and environment on the electronic structure and exciton binding energy of MoS2 from first principles," *Physical Review B - Condensed Matter and Materials Physics*, vol. 86, no. 24, pp. 1–6, 2012, ISSN: 10980121. DOI: 10.1103/PhysRevB.86.241201.

[20] A. Chernikov, T. C. Berkelbach, H. M. Hill, A. F. Rigosi, Y. Li, O. B. Aslan, D. R. Reichman, M. S. Hybertsen, and T. F. Heinz, "Exciton Binding Energy and Nonhydrogenic Rydberg Series in Monolayer WS_2," *Physical Review Letters*, vol. 113, no. 7, p. 076 802, 2014, ISSN: 0031-9007. DOI: 10.1103/PhysRevLett.113.076802. [Online]. Available: http://link.aps.org/doi/10.1103/PhysRevLett.113.076802.

[21] H. M. Hill, A. F. Rigosi, C. Roquelet, A. Chernikov, T. C. Berkelbach, D. R. Reichman, M. S. Hybertsen, L. E. Brus, and T. F. Heinz, "Observation of excitonic Rydberg states in monolayer MoS2 and WS2 by photoluminescence excitation spectroscopy," *Nano letters*, vol. 15, pp. 2992–2997, 2015, ISSN: 1530-6984. DOI: 10.1021/nl504868p. [Online]. Available: http://pubs.acs.org/doi/abs/10.1021/nl504868p.

[22] G. W. Mudd, S. A. Svatek, T. Ren, A. Patanè, O. Makarovsky, L. Eaves, P. H. Beton, Z. D. Kovalyuk, G. V. Lashkarev, Z. R. Kudrynskyi, and A. I. Dmitriev, "Tuning the bandgap of exfoliated inse nanosheets by quantum confinement," *Advanced Materials*, vol. 25, no. 40, pp. 5714–5718, 2013, ISSN: 1521-4095. DOI: 10.1002/adma.201302616. [Online]. Available: http://dx.doi.org/10.1002/adma.201302616.

[23] G. W. Mudd, M. R. Molas, X. Chen, V. Zólyomi, K. Nogajewski, Z. R. Kudrynskyi, Z. D. Kovalyuk, G. Yusa, O. Makarovsky, L. Eaves, M. Potemski, V. I. Fal'ko, and A. Patanè, "The direct-to-indirect band gap crossover in two-dimensional van der Waals Indium Selenide crystals," *Scientific Reports*, vol. 6, no. 1, p. 39 619, Dec. 2016, ISSN: 2045-2322.

DOI: 10.1038/srep39619. [Online]. Available: http://dx.doi.org/10.1038/srep39619%20http://10.0.4.14/srep39619%20http://www.nature.com/articles/srep39619.

[24] G. W. Mudd, A. Patanè, Z. R. Kudrynskyi, M. W. Fay, O. Makarovsky, L. Eaves, Z. D. Kovalyuk, V. Zólyomi, and V. Falko, "Quantum confined acceptors and donors in InSe nanosheets," *Applied Physics Letters*, vol. 105, no. 22, p. 221 909, Dec. 2014, ISSN: 0003-6951. DOI: 10.1063/1.4903738. [Online]. Available: http://aip.scitation.org/doi/10.1063/1.4903738.

[25] O. Del Pozo-Zamudio, S. Schwarz, J. Klein, R. C. Schofield, E. A. Chekhovich, O. Ceylan, E. Margapoti, A. I. Dmitriev, G. V. Lashkarev, D. N. Borisenko, N. N. Kolesnikov, J. J. Finley, and A. I. Tartakovskii, "Photoluminescence and Raman investigation of stability of InSe and GaSe thin films," pp. 1–6, Jun. 2015. arXiv: 1506.05619. [Online]. Available: http://arxiv.org/abs/1506.05619.

[26] W. Feng, W. Zheng, W. Cao, and P. Hu, "Back Gated Multilayer InSe Transistors with Enhanced Carrier Mobilities via the Suppression of Carrier Scattering from a Dielectric Interface," *Advanced Materials*, vol. 26, no. 38, pp. 6587–6593, Oct. 2014, ISSN: 09359648. DOI: 10.1002/adma.201402427. [Online]. Available: http://doi.wiley.com/10.1002/adma.201402427.

[27] S. Deckoff-Jones, J. Zhang, C. E. Petoukhoff, M. K. Man, S. Lei, R. Vajtai, P. M. Ajayan, D. Talbayev, J. Madéo, and K. M. Dani, "Observing the interplay between surface and bulk optical nonlinearities in thin van der Waals crystals," *Scientific Reports*, vol. 6, no. 1, p. 22 620, 2016, ISSN: 2045-2322. DOI: 10.1038/srep22620. [Online]. Available: http://www.nature.com/articles/srep22620.

[28] X. Zhou, J. Cheng, Y. Zhou, T. Cao, H. Hong, Z. Liao, S. Wu, H. Peng, K. Liu, and D. Yu, "Strong second-harmonic generation in atomic layered gase," *Journal of the American Chemical Society*, vol. 137, no. 25, pp. 7994–7997, 2015, PMID: 26060875. DOI: 10.1021/jacs.5b04305. eprint: https://doi.org/10.1021/jacs.5b04305. [Online]. Available: https://doi.org/10.1021/jacs.5b04305.

[29] S. Lei, L. Ge, S. Najmaei, A. George, R. Kappera, J. Lou, M. Chhowalla, H. Yamaguchi, G. Gupta, R. Vajtai, A. D. Mohite, and P. M. Ajayan, "Evolution of the Electronic Band Structure and Efficient Photo-Detection in Atomic Layers of InSe," *ACS Nano*, vol. 8, no. 2, pp. 1263–1272, Feb. 2014, ISSN: 1936-0851. DOI: 10.1021/nn405036u. [Online]. Available: http://dx.doi.org/10.1021/nn405036u%20http://pubs.acs.org/doi/abs/10.1021/nn405036u.

[30] S. R. Tamalampudi, Y.-Y. Lu, R. Kumar U., R. Sankar, C.-D. Liao, K. Moorthy B., C.-H. Cheng, F. C. Chou, and Y.-T. Chen, "High Performance and Bendable Few-Layered InSe Photodetectors with Broad Spectral Response," *Nano Letters*, vol. 14, no. 5, pp. 2800–2806, May 2014, ISSN: 1530-6984. DOI: 10.1021/nl500817g. [Online]. Available: http://pubs.acs.org/doi/abs/10.1021/nl500817g.

[31] J. Wilson and A. Yoffe, "The transition metal dichalcogenides discussion and interpretation of the observed optical, electrical and structural properties," *Advances in Physics*, no. May 2012, pp. 37–41, 1969. DOI: http://dx.doi.org/10.1080/00018736900101307. [Online]. Available: http://www.tandfonline.com/doi/abs/10.1080/00018736900101307.

[32] F. Reale, K. Sharda, and C. Mattevi, "From bulk crystals to atomically thin layers of group VI-transition metal dichalcogenides vapour phase synthesis," *Applied Materials Today*, vol. 3, pp. 11–22, Jun. 2016, ISSN: 23529407. DOI: 10.1016/j.apmt.2015.12.003. [Online]. Available: http://dx.doi.org/10.1016/j.apmt.2015.12.003%20http://linkinghub.elsevier.com/retrieve/pii/S2352940715300160.

[33] D. I. Bletskan, "Material Synthesis and Growth of the Single Crystals of the Type $A^{IV}B^{VI}$ and $A^{IV}B_2^{VI}$," *Chalcogenide Letters*, vol. 4, no. 1, pp. 1–16, 2007.

[34] A. Al-Hilli and B. Evans, "The preparation and properties of transition metal dichalcogenide single crystals," *Journal of Crystal Growth*, vol. 15, no. 2, pp. 93–101, 1972, ISSN: 00220248. DOI: 10.1016/0022-0248(72)90129-7. [Online]. Available: http://linkinghub.elsevier.com/retrieve/pii/0022024872901297%7B%5C%%7D5Cnhttp://www.sciencedirect.com/science/article/pii/0022024872901297%7B%5C%%7D5Cnhttp://linkinghub.elsevier.com/retrieve/pii/0022024872901297.

[35] B. Dalrymple, S. Mroczkowski, and D. Prober, "Vapor transport crystal growth of the transition metal dichalcogenide compounds $Nb_{(1-x)}Ta_xSe_2$," *Journal of Crystal Growth*, vol. 74, no. 3, pp. 575–580, 1986, ISSN: 00220248. DOI: 10.1016/0022-0248(86)90204-6. [Online]. Available: http://www.sciencedirect.com/science/article/pii/0022024886902046.

[36] M. K. Agarwal, P. D. Patel, L. T. Talele, and D. Laxminarayana, "Optical band gaps of Molybdenum Sulphoselenide," *Phys. Status Solidi A*, vol. 90, p. 107, 1985, ISSN: 00318965. DOI: 10.1002/pssa.2210900167.

[37] M. Agarwal and P. Wani, "Growth conditions and crystal structure parameters of layer compounds in the series $Mo_{(1-x)}W_xSe_2$," *Materials Research Bulletin*, vol. 14, no. 6, pp. 825–830, Jun. 1979, ISSN: 00255408. DOI: 10.1016/0025-5408(79)90144-2. [Online]. Available: http://linkinghub.elsevier.com/retrieve/pii/0025540879901442.

[38] S. Susarla, A. Kutana, J. A. Hachtel, V. Kochat, A. Apte, R. Vajtai, J. C. Idrobo, B. I. Yakobson, C. S. Tiwary, and P. M. Ajayan, "Quaternary 2D Transition Metal Dichalcogenides (TMDs) with Tunable Bandgap," *Advanced Materials*, no. May, 2017, ISSN: 15214095. DOI: 10.1002/adma.201702457.

[39] Y. Shi, W. Zhou, A.-Y. Lu, W. Fang, Y.-H. Lee, A. L. Hsu, S. M. Kim, K. K. Kim, H. Y. Yang, L.-J. Li, J.-C. Idrobo, and J. Kong, "van der Waals epitaxy of MoS_2 layers using graphene as growth templates.," *Nano letters*, vol. 12, no. 6, pp. 2784–91, Jun. 2012, ISSN: 1530-6992. DOI: 10.1021/nl204562j. [Online]. Available: http://www.ncbi.nlm.nih.gov/pubmed/22642717.

[40] K.-K. Liu, W. Zhang, Y.-H. Lee, Y.-C. Lin, M.-T. Chang, C.-Y. Su, C.-S. Chang, H. Li, Y. Shi, H. Zhang, C.-S. Lai, and L.-J. Li, "Growth of large-area and highly crystalline MoS2 thin layers on insulating substrates.," *Nano letters*, vol. 12, no. 3, pp. 1538–44, Mar. 2012, ISSN: 1530-6992. DOI: 10.1021/nl2043612. [Online]. Available: http://www.ncbi.nlm.nih.gov/pubmed/22369470.

[41] Y.-H. Lee, X.-Q. Zhang, W. Zhang, M.-T. Chang, C.-T. Lin, K.-D. Chang, Y.-C. Yu, J. T.-W. Wang, C.-S. Chang, L.-J. Li, and T.-W. Lin, "Synthesis of large-area MoS2 atomic layers with chemical vapor deposition.," *Advanced materials (Deerfield Beach, Fla.)*, vol. 24, no. 17, pp. 2320–5, May 2012, ISSN: 1521-4095. DOI: 10.1002/adma.201104798. [Online]. Available: http://www.ncbi.nlm.nih.gov/pubmed/22467187.

[42] C. Mai, A. Barrette, Y. Yu, Y. G. Semenov, K. W. Kim, L. Cao, and K. Gundogdu, "Many-body effects in valleytronics: Direct measurement of valley lifetimes in single-layer MoS2," *Nano letters*, vol. 14, no. 1, pp. 202–206, 2014, ISSN: 15306984. DOI: 10.1021/nl403742j.

[43] H. R. Gutiérrez, N. Perea-López, A. L. Elías, A. Berkdemir, B. Wang, R. Lv, F. López-Urías, V. H. Crespi, H. Terrones, and M. Terrones, "Extraordinary room-temperature photoluminescence in triangular WS2 monolayers.," *Nano letters*, vol. 13, no. 8, pp. 3447–54, Aug. 2013, ISSN: 1530-6992. DOI: 10.1021/nl3026357. [Online]. Available: http://www.ncbi.nlm.nih.gov/pubmed/23194096.

[44] J.-G. Song, J. Park, W. Lee, T. Choi, H. Jung, C. W. Lee, S.-h. Hwang, J. M. Myoung, J.-H. Jung, S.-H. Kim, C. Lansalot-Matras, and H. Kim, "Conformal Synthesis of Tungsten Disulfide Nanosheets Using Atomic Layer Deposition," *ACS nano*, pp. 11 333–11 340, 2013, ISSN: 1936-0851.

[45] S. Wu, C. Huang, G. Aivazian, J. S. Ross, D. H. Cobden, and X. Xu, "Vapor-solid growth of high optical quality MoS_2 monolayers with near-unity valley polarization.," *ACS nano*, vol. 7, no. 3, pp. 2768–72, Mar. 2013, ISSN: 1936-086X. DOI: 10.1021/nn4002038. [Online]. Available: http://www.ncbi.nlm.nih.gov/pubmed/23427810.

[46] Y. Gong, J. Lin, X. Wang, G. Shi, S. Lei, Z. Lin, X. Zou, G. Ye, R. Vajtai, B. I. Yakobson, H. Terrones, M. Terrones, B. K. Tay, J. Lou, S. T. Pantelides, Z. Liu, W. Zhou, and P. M. Ajayan, "Vertical and in-plane heterostructures from WS_2/MoS_2 monolayers," *Nature Materials*, vol. 13, no. 12, pp. 1135–1142, Sep. 2014, ISSN: 1476-1122. DOI: 10.1038/nmat4091. [Online]. Available: http://www.nature.com/doifinder/10.1038/nmat4091.

[47] A. Azizi, Y. Wang, Z. Lin, K. Wang, A. L. Elias, M. Terrones, V. H. Crespi, and N. Alem, "Spontaneous Formation of Atomically Thin Stripes in Transition Metal Dichalcogenide Monolayers," *Nano Letters*, vol. 16, no. 11, pp. 6982–6987, Nov. 2016, ISSN: 1530-6984. DOI: 10.1021/acs.nanolett.6b03075. [Online]. Available: http://pubs.acs.org/doi/10.1021/acs.nanolett.6b03075.

[48] M. O'Brien, N. McEvoy, D. Hanlon, K. Lee, R. Gatensby, J. N. Coleman, and G. S. Duesberg, "Low wavenumber Raman spectroscopy of highly crystalline $MoSe_2$ grown by chemical vapor deposition," *physica status solidi (b)*, vol. 252, no. 11, pp. 2385–2389, Nov. 2015, ISSN: 03701972. DOI: 10.1002/pssb.201552225. arXiv: 1505.02260. [Online]. Available: http://doi.wiley.com/10.1002/pssb.201570369%20http://doi.wiley.com/10.1002/pssb.201552225.

[49] S. J. Haigh, A. Gholinia, R. Jalil, S. Romani, L. Britnell, D. C. Elias, K. S. Novoselov, L. A. Ponomarenko, A. K. Geim, and R. Gorbachev, "Cross-sectional imaging of individual layers and buried interfaces of graphene-based heterostructures and superlattices," *Nature Materials*, vol. 11, no. 9, pp. 764–767, Jul. 2012, ISSN: 1476-1122. DOI: 10.1038/nmat3386. [Online]. Available: https://www.nature.com/articles/nmat3386%20http://www.nature.com/doifinder/10.1038/nmat3386.

[50] K. S. Vasu, E. Prestat, J. Abraham, J. Dix, R. J. Kashtiban, J. Beheshtian, J. Sloan, P. Carbone, M. Neek-Amal, S. J. Haigh, A. K. Geim, and R. R. Nair, "Van der Waals pressure and its effect on trapped interlayer molecules," *Nature Communications*, vol. 7, p. 12 168, Jul. 2016, ISSN: 2041-1723. DOI: 10.1038/ncomms12168. arXiv: 1605.07106. [Online]. Available: http://www.nature.com/doifinder/10.1038/ncomms12168.

[51] E. Khestanova, F. Guinea, L. Fumagalli, A. K. Geim, and I. V. Grigorieva, "Universal shape and pressure inside bubbles appearing in van der Waals heterostructures," *Nature Communications*, vol. 7, p. 12 587, Aug. 2016, ISSN: 2041-1723. DOI: 10.1038/ncomms12587. arXiv: 1604.00086. [Online]. Available: http://www.nature.com/doifinder/10.1038/ncomms12587.

[52] G. Argentero, A. Mittelberger, M. Reza Ahmadpour Monazam, Y. Cao, T. J. Pennycook, C. Mangler, C. Kramberger, J. Kotakoski, A. K. Geim, and J. C. Meyer, "Unraveling the 3D Atomic Structure of a Suspended Graphene/hBN van der Waals Heterostructure," *Nano Letters*, vol. 17, no. 3, pp. 1409–1416, Mar. 2017, ISSN: 1530-6984. DOI: 10.1021/acs.nanolett.6b04360. arXiv: 1702.02836. [Online]. Available: http://pubs.acs.org/doi/10.1021/acs.nanolett.6b04360.

[53] C. R. Woods, F. Withers, M. J. Zhu, Y. Cao, G. Yu, A. Kozikov, M. Ben Shalom, S. V. Morozov, M. M. van Wijk, A. Fasolino, M. I. Katsnelson, K. Watanabe, T. Taniguchi, A. K. Geim, A. Mishchenko, and K. S. Novoselov, "Macroscopic self-reorientation of interacting two-dimensional crystals," *Nature Communications*, vol. 7, p. 10 800, Mar. 2016, ISSN: 2041-1723. DOI: 10.1038/ncomms10800. arXiv: 1603.04765. [Online]. Available: http://www.nature.com/doifinder/10.1038/ncomms10800.

[54] A. K. Geim and I. V. Grigorieva, "Van der Waals heterostructures.," *Nature*, vol. 499, no. 7459, pp. 419–25, Jul. 2013, ISSN: 1476-4687. DOI: 10.1038/nature12385. [Online]. Available: http://www.ncbi.nlm.nih.gov/pubmed/23887427.

[55] A. P. Rooney, A. Kozikov, A. N. Rudenko, E. Prestat, M. J. Hamer, F. Withers, Y. Cao, K. S. Novoselov, M. I. Katsnelson, R. Gorbachev, and S. J. Haigh, "Observing Imperfection in Atomic Interfaces for van der Waals Heterostructures," *Nano Letters*, vol. 17, no. 9, pp. 5222–5228, Sep. 2017, ISSN: 1530-6984. DOI: 10.1021/acs.nanolett.7b01248. [Online]. Available: http://pubs.acs.org/doi/abs/10.1021/acs.nanolett.7b01248%20http://pubs.acs.org/doi/10.1021/acs.nanolett.7b01248.

[56] R. Gatensby, N. McEvoy, K. Lee, T. Hallam, N. C. Berner, E. Rezvani, S. Winters, M. O'Brien, and G. S. Duesberg, "Controlled synthesis of transition metal dichalcogenide thin films for electronic applications," *Applied Surface Science*, vol. 297, pp. 139–146, Apr. 2014, ISSN: 01694332. DOI: 10.1016/j.apsusc.2014.01.103. [Online]. Available: http://linkinghub.elsevier.com/retrieve/pii/S0169433214001433.

[57] E. Scalise, M. Houssa, G. Pourtois, V. Afanaseev, and A. Stesmans, "First-principles study of strained 2D MoS_2," *Physica E: Low-dimensional Systems and Nanostructures*, vol. 56, pp. 416–421, Feb. 2014, ISSN: 13869477. DOI: 10.1016/j.physe.2012.07.029. [Online]. Available: http://linkinghub.elsevier.com/retrieve/pii/S1386947712003062.

[58] B. Amin, T. P. Kaloni, and U. Schwingenschlögl, "Strain engineering of WS_2 , WSe_2, and WTe_2," *RSC Advances*, vol. 4, no. 65, p. 34 561, Aug. 2014, ISSN: 2046-2069. DOI: 10.1039/C4RA06378C. [Online]. Available: http://xlink.rsc.org/?DOI=C4RA06378C.

[59] A. M. Rasmussen, S. T. Teklemichael, E. Mafi, Y. Gu, and M. D. McCluskey, "Pressure-induced phase transformation of In 2 Se 3," *Applied Physics Letters*, vol. 102, no. 6, p. 062 105, Feb. 2013, ISSN: 0003-6951. DOI: 10.1063/1.4792313. [Online]. Available: http://aip.scitation.org/doi/10.1063/1.4792313.

[60] R. Sooryakumar and M. V. Klein, "The superconducting energy gap in 2H-NbSe2 and its coupling to charge density waves," *Physica B+C*, vol. 105, no. 1-3, pp. 422–427, 1981. DOI: 10.1016/0378-4363(81)90288-6.

[61] L. Liang, A. A. Puretzky, B. G. Sumpter, and V. Meunier, "Interlayer bond polarizability model for stacking-dependent low-frequency Raman scattering in layered materials," *Nanoscale*, vol. 9, no. 40, pp. 15 340–15 355, 2017, ISSN: 2040-3364. DOI: 10.1039/C7NR05839J. arXiv: 1708.02614. [Online]. Available: http://arxiv.org/abs/1708.02614%20http://xlink.rsc.org/?DOI=C7NR05839J.

[62] L. S. Schadler and C. Galiotis, "Fundamentals and applications of micro Raman spectroscopy to strain measurements in fibre reinforced composites," *International Materials Reviews*, vol. 40, no. 3, pp. 116–134, Jan. 1995, ISSN: 09506608. DOI: 10.1179/095066095790326094. [Online]. Available: http://openurl.ingenta.com/content/xref?genre=article%7B%5C&%7Dissn=0950-6608%7B%5C&%7Dvolume=40%7B%5C&%7Dissue=3%7B%5C&%7Dspage=116.

[63] A. L. Glebov, O. Mokhun, A. Rapaport, S. Vergnole, V. Smirnov, and L. B. Glebov, "Volume Bragg gratings as ultra-narrow and multiband optical filters," in *Proceedings of SPIE (2012)*, H. Thienpont, J. Mohr, H. Zappe, and H. Nakajima, Eds., vol. 8428, Jun. 2012, p. 84280C. DOI: 10.1117/12.923575. [Online]. Available: http://proceedings.spiedigitallibrary.org/proceeding.aspx?articleid=1315954%20http://proceedings.spiedigitallibrary.org/proceeding.aspx?doi=10.1117/12.923575.

Chapter 2

Semiconducting Transition Metal Chalcogenide Optical Properties

Semiconductor materials are those where the Fermi level of the electrons occurs at an energy that lies between the resulting energy bands of the bonding electrons of the chemical species of a crystalline material, with energies such that electrons may be thermally excited between valence and conduction bands. The technological significance of these materials is that their electronic properties may be altered by modest electromagnetic fields, such that they can be used as substrates for computing, or as sensors in diverse applications.

2.1 Electronic Band Structure and Excitons

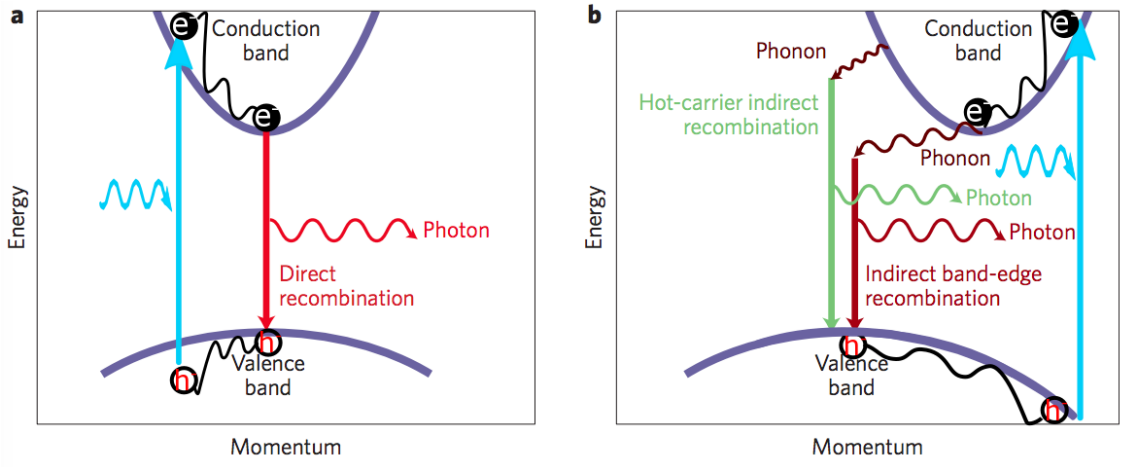

Figure 2.1: Illustrations of the E–K diagrams for exciton recombination processes from: a, direct; and b, indirect band gap semiconductors. Figure adapted from reference [1].

Excitons are quasiparticles formed as an electron in the conduction band bound to a hole in the valence band by the Coulomb interaction. They may be generated via electrical injection, formed spontaneously as in the case of the excitonic insulator, or produced through absorption

of photons via interband transitions. Figure 2.1 contains E-K diagrams to show the difference in recombination of exciton electron–hole pairs in; direct–gap and indirect–gap semiconductors. Photoexcitation, with energy greater than the fundamental bandgap may produce interband transitions of carriers, resulting in an additional hole in the valence band, and electron in the conduction band. Immediately following the transition, before the carriers relax to a ground state and form an exciton, they may recombine via a process called hot luminescence, shown in panel b, otherwise the carriers relax non-radiatively via scattering by phonons or other carriers, in the case in Auger scattering, to a ground state, or by scattering into defect states.

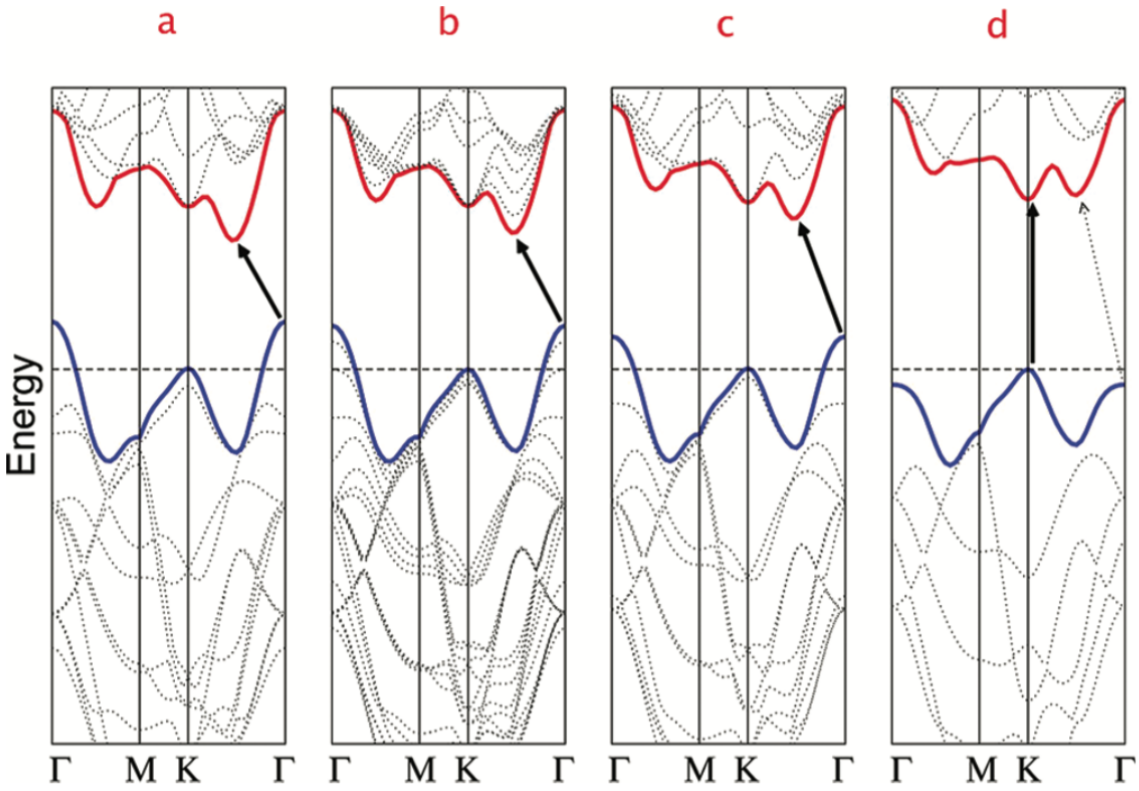

Figure 2.2: Calculated band structures for MoS_2 (a) bulk, (b) quad-layer, (c) bilayer, and (d) monolayer. The solid arrows indicate the lowest energy transitions. Bulk MoS_2 is characterised by an indirect bandgap where the transition takes place between the Γ point of the conduction band and a valley between Γ and K, there also exists a locally direct gap at the K point. With reduced layer thickness, the indirect bandgap becomes larger, while the direct excitonic transition changes little. The case for the monolayer in d, it that the K point transition is the bandgap minimum. These calculations have been confirmed by direct observation using ARPES [2]. Figure from reference [3].

The nature of this ground state can be, as in figure 2.1 a, direct, whereby the electron and hole have the same value of crystal momentum and can recombine with the emission of a photon. The alternative, shown in 2.1 b, is that the electron and hole take different values of crystal momentum and since the crystal wavevector of photons is relatively negligible, recombination requires interactions with other quasiparticles, typically phonons.

Specifically in TMDs these excitons some hybrid of Wannier-Mott and Frenkel excitons, with a Bohr radius of the order of the lattice constant [4] but not bound to specific atoms, with a wave function spanning multiple unit cells[5].

The band structure for MoS_2, is shown in figure 2.2 demonstrating the indirect-direct band gap transition in the monolayer. This observation is a result of the quantum confinement effects; density function theory (DFT) calculations show that the conduction band states at the K -point result from localised Mo d-orbitals and are quantitatively unaffected by interlayer coupling. The states near the Γ -point are given by combinations of the anti-bonding p_z -orbitals from the S atoms and the d-orbitals on the Mo atoms. Modification of the number of layers results in a change of the states at the Γ -point while change of the band energies at the K-point is negligible [2], [3].

In TMDs there exists significant spin orbit coupling, not shown in the calculated MoS_2 bandstructure in figure 2.2, a pictorial representation of this SOC is made in E–K diagrams of figure 2.3. The figure shows the band transitions at the K and K' points for monolayer tungsten dichalcogenides, panel a, and molybdenum dichalcogenides, panel b: It can be seen that the valence band states are split, this is due to the strong SOC of the heavy metal d-orbitals which constitute this band at $\pm K$, this splitting persists at all thickness and results in the exciton B-transition. In the case of the conduction band, the spin splitting is present due to weak mixing of non-SOC d-orbitals with chalcogen p-orbitals [6], [7].

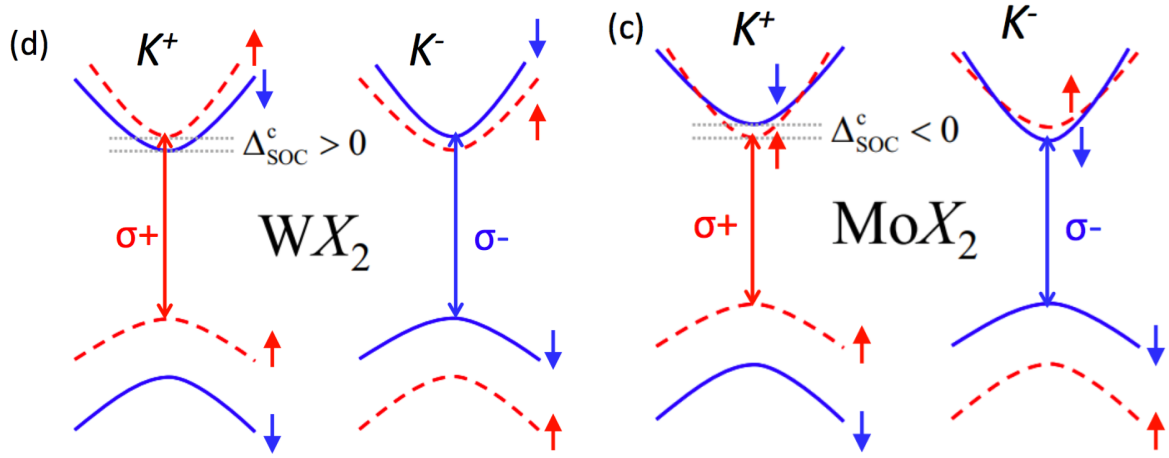

(a) Tungsten dichalcogenides. (b) Molybdenum dichalcogenides

Figure 2.3: The difference in the sign and magnitude of the spin orbit coupled conduction band splitting in TMDs. Figure from reference [8].

2.2 Raman Effect in TMDs

The Raman effect describes the inelastic scattering of light, as discovered in liquids by C. V. Raman and K. S. Krishnan [9] and in crystals by G. Landsberg and L. Mandelstam [10].

Spectroscopically apparent as a set of satellite peaks around the excitation source frequency, Raman scattered light reveals low energy excitations within a system.

2.2.1 Basic Theory

Unlike Rayleigh scattering, where no change in photon energy is observed, Raman scattering is characterised by a decreased (Stokes) or an increased (anti-Stokes) photon energy. The energy change arises due to the photon exciting a substance from a ground to a virtual or short lifetime state from which the substance relaxes to some mechanically excited state with the emission of a lower energy photon. The mechanism of excitation is via the photon's interaction with the electron density shared by atoms of substance as a chemical bond. The polarisation of this electron cloud can be understood quantum mechanically, starting with the Hamiltonian of the system;

$$H = H_\nu + H_{em} + H_{int}, \tag{2.1}$$

which is expressed as the sum of the contributions from the bond vibration energy, the photon's electromagnetic field energy and a term describing the interaction between the two. The vibrational term describing kinetic and potential energy is

$$H_\nu = \frac{1}{2m}(p^2 + \omega_0^2 q^2) \tag{2.2}$$

where ω_0 is the normal mode angular frequency, q is the mode amplitude, and p is the momentum. In the simple harmonic approximation, bosonic creation and annihilation operators of molecular vibration $b^\dagger$ & b may be applied in the expression of q;

$$q = \sqrt{\frac{\hbar}{4\pi\mu\omega_0}}[b^\dagger + b] \tag{2.3}$$

with μ representing the electric dipole moment of the excitation. The vibrational Hamiltonian is thus;

$$H_\nu = \hbar\omega_0[b^\dagger b + \frac{1}{2}] \tag{2.4}$$

Addressing the Hamiltonian of the field and applying creation and annihilation operators in a similar fashion to before yields a quantised field;

$$E_\lambda = \sqrt{\frac{2\pi\hbar\omega_L}{\varepsilon V}} \sum_{K_\lambda} e_{k_\lambda} i[a_{k_\lambda}^\dagger + a_{k_\lambda}] \tag{2.5}$$

where ω_L is the laser frequency, e_{k_λ} is a unit vector describing the field polarization, V is the interaction volume and ε is the permittivity. Inspection of the equations 2.4 & 2.5 allows a treatment of the field as a collection of many quantum harmonic oscillators allowing the

Hamiltonian for the field

$$H_{em} = \hbar\omega_L[a^\dagger a + \frac{1}{2}]. \tag{2.6}$$

The remaining term in the system Hamiltonian is due to the photon's EM field impinging on the bond and resulting in a polarization, the interaction Hamiltonian can be produced by applying first-order perturbation theory and using the electric dipole approximation. Considering the bond polarization as $P = \alpha \cdot E$ and expanding the polarisability α of a phonon mode about the mode amplitude q,

$$\alpha = \alpha_0 + \left(\frac{\partial\alpha}{\partial q}\right)_0 q + \left(\frac{\partial^2\alpha}{\partial q^2}\right)_0 \frac{q^2}{2} + \dots \tag{2.7}$$

The interaction Hamiltonian is,

$$\begin{aligned} H_{int} &= E \cdot \alpha \cdot E \\ &= E \cdot \alpha_0 \cdot E + \left(\frac{\partial\alpha}{\partial q}\right)_0 E \cdot q \cdot E + \dots \end{aligned} \tag{2.8}$$

The first term describes Rayleigh scattering, the second is first-order Raman scattering single phonon interactions and higher order terms describe higher-order, multi phonon events. To show this, simple expressions $q(t) = q_0 \cos(\Omega t)$ & $E(t) = E_0 \cos(\omega t)$ for mode amplitude and the electric field, respectively, may be substituted in $P = \alpha \cdot E$, retaining only the first-order Raman term which results in an induced dipole moment

$$\alpha_1 E_0 q_0 \cos(\omega t)\cos(\Omega t) = \frac{1}{2}\alpha_1 E_0 q_0[\cos\Big((\omega+\Omega)t\Big) + \cos\Big((\omega-\Omega)t\Big)] \tag{2.9}$$

The result describes the Stokes $(\omega-\Omega)$ and the anti Stokes $(\omega+\Omega)$ frequencies of the Raman scattered photon. Returning to the quantum mechanical description and substituting the field $E = E_L + E_S + E_{aS}$ into equation 2.9; where E_L is given by the quantised field of equation 2.5 and the subscripts L, S, & aS refer to the Laser, Stokes and anti-Stokes fields, respectively. The interaction Hamiltonian far from any resonance, becomes a symmetric function

$$\begin{aligned} H_{int} \approx \left(\frac{\partial\alpha}{\partial q}\right)_0 \Bigg\{ &\sum_{k_S k_L} \sqrt{\frac{2\omega_L\omega_S}{\omega_0}}(e_{k_L}\cdot e_{k_S})(a^\dagger_{k_S} b^\dagger a_{k_L} + a_{k_S} b a^\dagger_{k_L})\delta(k_L - k_S - K) + \dots \\ &\sum_{k_{aS} k_L} \sqrt{\frac{2\omega_L\omega_{aS}}{\omega_0}}(e_{k_L}\cdot e_{k_{aS}})(a^\dagger_{k_{aS}} b a_{k_L} + a_{k_{aS}} b^\dagger a^\dagger_{k_L})\delta(k_L - k_{aS} + K)\Bigg\} \end{aligned} \tag{2.10}$$

The delta function serves to exclude wave vectors violating the conservation of momentum from contributing and the two branches refer to the Stokes and anti-Stokes photons. It is insightful to compare the relative intensities of the Stokes and anti-Stokes transitions, applying

Fermi's Golden Rule, the Stokes intensity is

$$I(\omega - \Omega) \propto \left|\langle n_K + 1| \, H_{int} \, |n_K\rangle\right|^2 \propto n_K + 1 \tag{2.11}$$

where n_k is the population of the phonon mode with wave vector K, the anti-Stokes intensity is, similarly,

$$I(\omega + \Omega) \propto \left| \langle n_K - 1|H_{int}|n_K\rangle\right|^2 \propto n_K. \tag{2.12}$$

At a thermal equilibrium with temperature T where the mode population n_K is given by the Planck distribution function $1/[\exp\{\hbar\Omega/k_B T\} - 1]$ the ratio between the two is;

$$\frac{I(\omega + \Omega)}{I(\omega - \Omega)} = \frac{\langle n_K\rangle}{\langle n_K\rangle + 1} = \exp\left\{-\frac{\hbar\Omega}{k_B T}\right\}, \tag{2.13}$$

thus displaying a temperature dependence on the mode populations and the scattering intensities. The number of photons incident on a sample is considerably greater than the phonon populations of either the ground or excited vibrational states and hence the majority of photons are scattered by Rayleigh scattering, with a small proportion, $\approx 10^{-7}$ photons scattered by the Raman effect.

2.2.2 Symmetry Selection Rules

Symbol	Significance
E	Einheit, the identity operation
C_n	n-fold proper rotation about some axis
S_n	n-fold improper rotation about some axis, equivalent to a proper rotation followed by reflection in a mirror plane perpendicular to the rotational axis
i	Inversion through a center of symmetry
$\sigma_{h,v,ord}$	Mirror reflection though a plane horizontal, vertical, or dihedral to primary C_n axis

Table 2.1: Schönflies' notation for symmetry operations [11].

Symbol	Significance
A	Singly degenerate state, symmetric with respect to rotation about the principal C_n axis
B	Singly degenerate state, antisymmetric with respect to rotation about the principal C_n axis
E	Doubly degenerate (Entartet)
T	Triply degenerate
X_g	Gerade, symmetric; the sign of the wavefunction does not change on inversion of the unit cell
X_u	Ungerade, antisymmetric; the sign of the wavefunction changes on inversion of the unit cell
X_1	The sign of the wavefunction does not change upon reflection about a horizontal plane perpendicular to the principal axis
X_2	The sign of the wavefunction changes upon reflection about a horizontal plane perpendicular to the principal axis ll
$'$	Symmetric with respect to a horizontal symmetry plane σ_h
$''$	Antisymmetric with respect to a horizontal symmetry plane σ_h

Table 2.2: Mulliken's symbols for irreducible representations [12].

Ostensibly, Raman activity involves exclusively $q \approx 0$ events, since it is a near equilibrium process and crystal momentum should be conserved. From this, and considering Noether's first theorem; the Raman active modes in a crystal or molecule are determined by the symmetry of the system. The set of transformations — rotations, reflections & inversions (table 2.1) — preserving the crystal lattice forms a mathematical group expressible as a set of irreducible representations.

In order to determine the Raman-activity of a material, the symmetry considerations of the Hamiltonian necessitate the application of group theory to the molecular or crystal structure [11]. Beginning with simple spatial transformations, i.e. proper rotations, reflections and inversions, those which leave the structure in an indistinguishable configuration following their operation define the point group of the system, as described by Schönflies [13]. Assigning 'char-

acters' to each class of operation allows the construction of so-called irreducible representations of the point group which can in turn be denoted using the system defined by Mulliken [12] (table: 2.2). It is these irreducible representations that one assigns Raman active modes to.

From the tensor form of the polarisability $\overleftrightarrow{\alpha}$, noting that it's second rank symmetric and transforms quadratically, the presence of the polarisability in the Hamiltonian for the Raman interaction gives the condition that the Hamiltonian also be quadratically transformable; the corollary of which is that the characters of the symmetry operations constituting the irreducible representations of the point group dictate the symmetry of the lattice vibrations contributing to the Raman effect.

Inspecting the character table for a given point group, e.g. table 2.4, one may notice in the two rightmost columns both rotations ('R's), translations ('T's), and coordinate products ('α's), these are assigned to the irreducible representation under which these variables transform. It is thus the quadratic coordinate products which relate to the Raman activity of an irreducible representation.

Symbol	Symmetry Operations
$C_{n(and\ h,\ or\ v)}$	Cyclic; n-fold rotational axis with either a single horizontal (h) or n vertical (v) mirror planes
$S_{2n} \mid n \in 2\mathbb{Z}$	Spiegel; 2n-fold rotation-reflection axis, where $n \in 2\mathbb{Z} - 1 \mid S_n \equiv C_n h$
$D_{n(and\ h,\ or\ d)}$	Dihedral: One C_n axis with; n-C_2 axes with one horizontal and n vertical mirror planes (h); or n vertical mirror planes passing between C_2 axes (d)
$T_{(d\ or\ h)}$	Tetrahedral: Three C_2 axes, and four C_3 axes with three diagonal (d) or horizontal mirror planes (h)
$O_{(h)}$	Octahedral: Three C_4, four C_3, and six C_2 axes with horizontal mirror planes (h)
$I_{(h)}$	Icosahedral: Six C_5, ten C_3, and fifteen C_2 axes including horizontal mirror planes (h)

Table 2.3: A summary of the Schönflies' notation for point groups [11].

D_{6h}	E	$2C_6(z)$	$2C_3$	C_2	$3C_2'$	$3C_2''$	i	$2S_3$	$2S_6$	$\sigma_h(xy)$	$3\sigma_d$	$3\sigma_v$	Translations, rotations	quadratic functions
A_{1g}	+1	+1	+1	+1	+1	+1	+1	+1	+1	+1	+1	+1	–	x^2+y^2, z^2
A_{2g}	+1	+1	+1	+1	-1	-1	+1	+1	+1	+1	-1	-1	R_z	-
B_{1g}	+1	-1	+1	-1	+1	-1	+1	-1	+1	-1	+1	-1	-	-
B_{2g}	+1	-1	+1	-1	-1	+1	+1	-1	+1	-1	-1	+1	-	-
E_{1g}	+2	+1	-1	-2	0	0	+2	+1	-1	-2	0	0	(R_x, R_y)	(xz, yz)
E_{2g}	+2	-1	-1	+2	0	0	+2	-1	-1	+2	0	0	-	(x^2-y^2, xy)
A_{1u}	+1	+1	+1	+1	+1	+1	-1	-1	-1	-1	-1	-1	-	-
A_{2u}	+1	+1	+1	+1	-1	-1	-1	-1	-1	-1	+1	+1	z	-
B_{1u}	+1	-1	+1	-1	+1	-1	-1	+1	-1	+1	-1	+1	-	-
B_{2u}	+1	-1	+1	-1	-1	+1	-1	+1	-1	+1	+1	-1	-	-
E_{1u}	+2	+1	-1	-2	0	0	-2	-1	+1	+2	0	0	(x, y)	-
E_{2u}	+2	-1	-1	+2	0	0	-2	+1	+1	-2	0	0	-	

Table 2.4: Character table for the D_{6h} point group.

2.2.3 Resonant Raman Scattering

Ordinary Raman scattering holds the same dependence of scattering intensity with energy as Rayleigh scattering i.e. $I \propto \omega_L^4$, where the scattering occurs mainly through virtual intermediate vibrational or electronic transitions. In the vicinity of electronic interband transitions, however, there arises structure in the polarisability α the scattering Intensity is modified to

$$I \propto \omega_L^4 \left| \frac{\partial \alpha(\omega)}{\partial q} \right|_0^2 \left\langle q_0^2 \right\rangle \tag{2.14}$$

with an enhancement of the scattered intensity at electronic resonances and the allowance of contribution from antisymmetric Raman tensor components. Interactions with many-body effects such as excitons modify the allowed Raman modes due to the product of the space group symmetries of the participating excitations resulting in a greater number of symmetric elements contained in the Raman tensor.

Forbidden modes, those arising from some q-dependent part of the Raman tensor, by optical phonons and polaritons can also be observed due to enhancements due to Fröhlich interaction with longitudinal field of LO phonons.

2.3 Transition Metal Chalcogen Lattice Vibrations

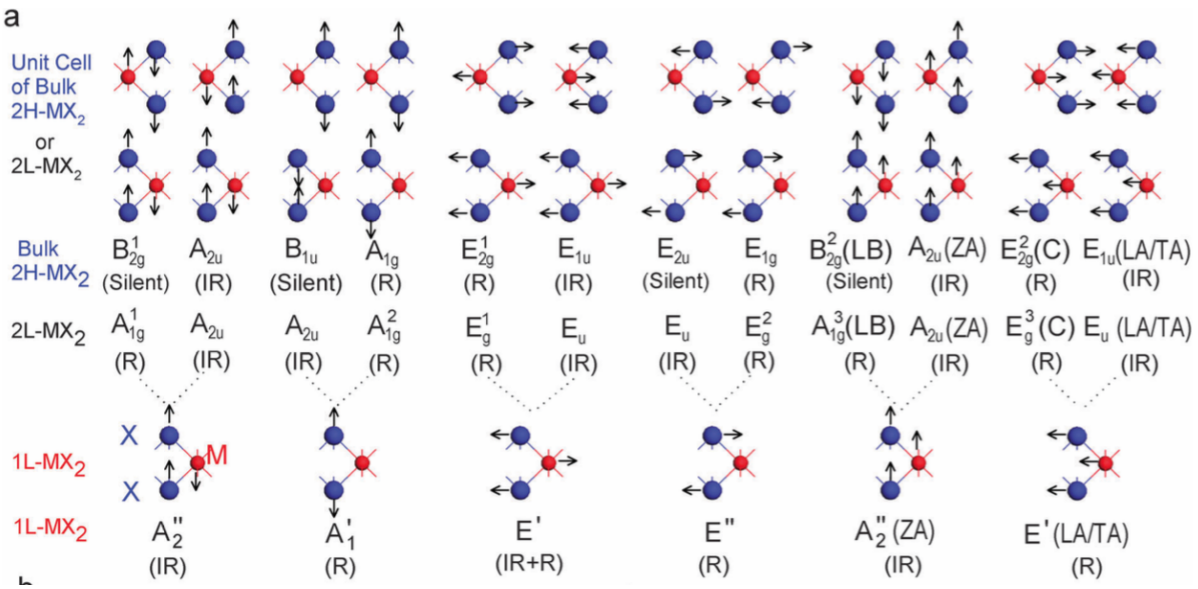

Figure 2.4: Illustrations of the vibrational modes of TMDs, of bulk, bilayer and monolayer thickness. Labelled according to their symmetry, and their optical activity, either Raman (R), infrared (IR), optically inactive (Silent). Layer breathing and shear modes are labelled as LB, and C, respectively; or acoustic, out of plane, longitudinal, or transverse; ZA, LA, TA, respectively. Figure from [14].

Bulk TMCs of the 2H polytype belong to the D_{6h} point group where the modes are characterised at Γ as follows:

- *Acoustic*: A_{2u}, and E_{1u}.
- *Raman Active*: A_{1g}, E_{1g}, E^1_{2g}, and E^2_{2g}.
- *Infrared Active*: A^2_{2u}, and E_{1u}.
- *Optically Inactive*: B^1_{2g}, B^2_{2g},B_{1u}, and E_{2u}.

Reducing the number of molecular layers of the TMC eventually modifies the symmetry of the system, due to reduced translational symmetry along the z-direction, perpendicular to the basal x–y plane. The reduction in symmetry becomes significant below 10 layers where odd numbers of layers belong to the D_{3h} point group owing to a horizontal reflection plane σ_h though the transition metal plane. In the case of the monolayer, the vibrational modes of the lattice can be expressed as:

- *Acoustic*: A''_2, and E′
- *Raman Active*: A', E′, E′, and E''
- *Infrared Active*: A''_2, and E′

Bilayer samples of TMDs, having an inversion symmetry about points in between the two layers, belongs to the D_{3d} point group with the following modes:

- *Acoustic*: A_{2u}, and E_u
- *Raman Active*: A^1_{1g}, A^2_{1g}, A^3_{1g}, E^1_g, E^1_g and E^3_g
- *Infrared Active*: A_{2u}, and E_u

These modes are summarised and illustrated in figure 2.4.

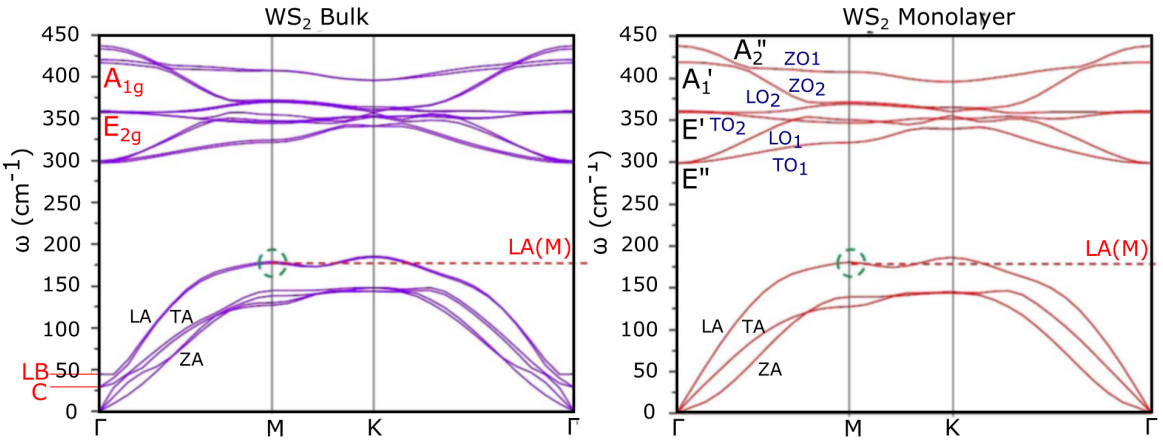

Figure 2.5: Calculated WS_2 phonon dispersion for bulk and monolayer thicknesses. Figure from reference [15].

It is instructive to view the phonon dispersion for TMDs in figures 2.5 and 2.6. For non resonant Raman Scattering in highly crystalline samples (i.e. with long range order), only Raman active modes at $q = 0$ at the Γ point, can be observed in first-order normal-incidence backscattering geometry, these are labelled for monolayer and bulk. For more disordered samples, with crystallites having finite domain sizes, the scattering condition is somewhat relaxed to $q \approx 0$ and spectroscopic Raman peaks are broadened by scattering contributions away from Γ. In the case of unidirectional strain, the phonon modes at $q = 0$ split into the TO and LO components, which can appear to broaden the spectroscopic peaks.

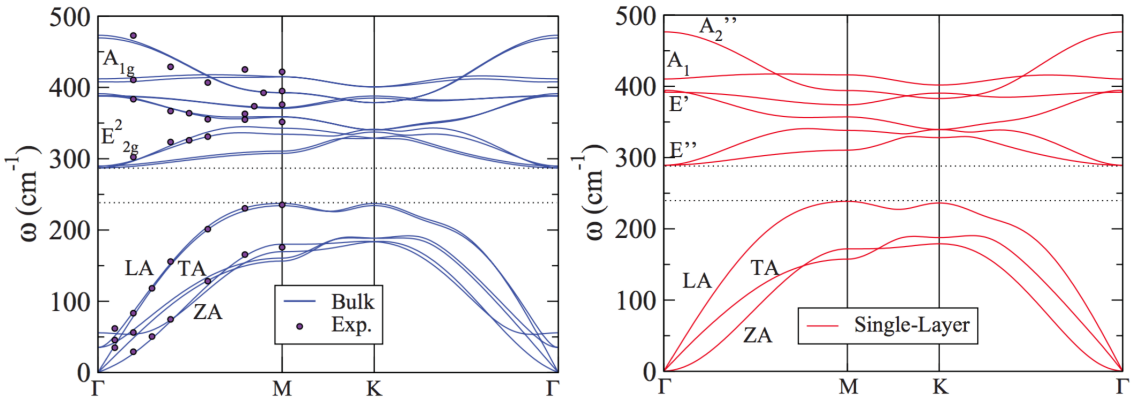

Figure 2.6: Calculated MoS_2 phonon dispersion for bulk and monolayer thicknesses, the points in the bulk calculation are points measured by Neutron scattering experiments[16]. Figure from [17].

In the WS_2 dispersion shown in figure 2.5 the LA(M) phonon is highlighted as this phonon is involved with a double resonant Raman process for the excitation wavelengths in the range (510–550) nm, scattering conduction band electrons between the K valley and a local valley along Γ–K.

References

[1] M. Fujita, "Silicon photonics: Nanocavity brightens silicon," *Nature Photonics*, vol. 7, no. 4, pp. 264–265, Mar. 2013, ISSN: 1749-4885. DOI: 10.1038/nphoton.2013.65. [Online]. Available: http://dx.doi.org/10.1038/nphoton.2013.65%20http://www.nature.com/doifinder/10.1038/nphoton.2013.65.

[2] Y. Zhang, T.-r. Chang, B. Zhou, Y.-t. Cui, H. Yan, Z. Liu, F. Schmitt, J. Lee, R. Moore, Y. Chen, H. Lin, H.-t. Jeng, S.-k. Mo, Z. Hussain, A. Bansil, and Z.-x. Shen, "Direct observation of the transition from indirect to direct bandgap in atomically thin epitaxial MoSe2.," *Nature nanotechnology*, vol. 9, no. 2, pp. 111–5, 2014, ISSN: 1748-3395. DOI: 10.1038/nnano.2013.277. [Online]. Available: http://www.ncbi.nlm.nih.gov/pubmed/24362235.

[3] A. Splendiani, L. Sun, Y. Zhang, T. Li, J. Kim, C. Y. Chim, G. Galli, and F. Wang, "Emerging photoluminescence in monolayer MoS2," *Nano letters*, vol. 10, no. 4, pp. 1271–1275, 2010, ISSN: 15306984. DOI: 10.1021/nl903868w.

[4] D. Y. Qiu, F. H. da Jornada, and S. G. Louie, "Optical Spectrum of MoS_2: Many–Body Effects and Diversity of Exciton States," *Phys. Rev. Lett.*, vol. 111, p. 216 805, 21 Nov. 2013. DOI: {10.1103/PhysRevLett.111.216805}. [Online]. Available: %7Bhttps://link.aps.org/doi/10.1103/PhysRevLett.111.216805%7D.

[5] Z. Ye, T. Cao, K. O'Brien, H. Zhu, X. Yin, Y. Wang, S. G. Louie, and X. Zhang, "Probing Excitonic Dark States in Single-layer Tungsten Disulfide," *Nature*, vol. 513, no. 7517, pp. 214–218, 2014, ISSN: 0028-0836. DOI: 10.1038/nature13734. arXiv: 1403.5568.

[6] A. Kormányos, V. Zólyomi, N. D. Drummond, and G. Burkard, "Spin-orbit coupling, quantum dots, and qubits in monolayer transition metal dichalcogenides," *Physical Review X*, vol. 4, no. 1, pp. 1–16, 2014, ISSN: 21603308. DOI: 10.1103/PhysRevX.4.011034. arXiv: 1310.7720.

[7] D. MacNeill, C. Heikes, K. F. Mak, Z. Anderson, A. Kormányos, V. Zólyomi, J. Park, and D. C. Ralph, "Breaking of Valley Degeneracy by Magnetic Field in Monolayer $MoSe_2$," *Physical Review Letters*, vol. 114, no. 3, p. 037 401, Jan. 2015, ISSN: 0031-9007. DOI: 10.1103/PhysRevLett.114.037401. arXiv: 1407.0686. [Online]. Available: http://arxiv.org/abs/1407.0686%20https://link.aps.org/doi/10.1103/PhysRevLett.114.037401.

[8] G. Wang, A. Chernikov, M. M. Glazov, T. F. Heinz, X. Marie, T. Amand, and B. Urbaszek, "Excitons in atomically thin transition metal dichalcogenides," no. Ml, Jul. 2017. arXiv: 1707.05863. [Online]. Available: http://arxiv.org/abs/1707.05863.

[9] C. V. Raman and K. S. Krishnan, "A New Type of Secondary Radiation," *Nature*, vol. 121, no. 3048, pp. 501–502, 1928. DOI: 10.1038/121501c0.

[10] G. Landsberg and L. Mandelstam, "Eine neue Erscheinung bei der Lichtzerstreuung in Krystallen," *Naturwissenschaften*, vol. 50, no. 11-12, pp. 769–780, 1928.

[11] F. A. Cotton, *"Chemical applications of group theory"*, 3rd. John Wiley & Sons, 1994, ISBN: 9780471010050.

[12] R. S. Mulliken, "Spectroscopy, molecular orbitals, and chemical bonding.," *Science*, vol. 157, no. 784, pp. 13–24, 1967, ISSN: 0036-8075. DOI: 10.1126/science.157.3784.13.

[13] A. Schoenflies, *"Krystallsysteme und Krystallstructur"*. Druck und Verlag von BG Teubner, 1891.

[14] X. Zhang, X.-F. Qiao, W. Shi, J.-B. Wu, D.-S. Jiang, and P.-H. Tan, "Phonon and Raman scattering of two-dimensional transition metal dichalcogenides from monolayer, multilayer to bulk material," *Chemical Society Reviews*, vol. 44, no. 9, pp. 2757–2785, 2015, ISSN: 0306-0012. DOI: 10.1039/C4CS00282B. arXiv: arXiv:1502.00701v1. [Online]. Available: http://xlink.rsc.org/?DOI=C4CS00282B.

[15] A. Berkdemir, H. R. Gutiérrez, A. R. Botello-Méndez, N. Perea-López, A. L. Elías, C.-I. Chia, B. Wang, V. H. Crespi, F. López-Urías, J.-C. Charlier, H. Terrones, and M. Terrones, "Identification of individual and few layers of WS_2 using Raman Spectroscopy," *Scientific Reports*, vol. 3, no. 1, p. 1755, Dec. 2013, ISSN: 2045-2322. DOI: 10.1038/srep01755. [Online]. Available: http://www.nature.com/doifinder/10.1038/srep01755%20http://www.nature.com/articles/srep01755.

[16] N. Wakabayashi, H. G. Smith, and R. M. Nicklow, "Lattice dynamics of hexagonal MoS_2 studied by neutron scattering," *Physical Review B*, vol. 12, no. 2, pp. 659–663, 1975, ISSN: 0556-2805. DOI: 10.1103/PhysRevB.12.659. [Online]. Available: http://link.aps.org/doi/10.1103/PhysRevB.12.659.

[17] A. Molina-Sánchez and L. Wirtz, "Phonons in single-layer and few-layer MoS_2 and WS_2," *Physical Review B*, vol. 84, no. 15, p. 155 413, Oct. 2011, ISSN: 1098-0121. DOI: 10.1103/PhysRevB.84.155413. arXiv: 1109.5499. [Online]. Available: https://link.aps.org/doi/10.1103/PhysRevB.84.155413.

Chapter 3

Experimental Methods

3.1 Optical Spectroscopy

Light–matter interactions are used by many life-forms in order to detect the reality in which they exist When in 1666, Sir Isaac Newton demonstrated the chromatic dispersion of transparent media, he realised an important means by which nature could be studied. His contemporaries speculated the observations were manifestations of ghosts and titled themselves *'ghost watchers'*, which results from the following: *'ghost'* in Latin (*spectrum*), and *'watcher'* in Greek (*scopos*) – to provide the term 'spectroscopy'. Over time this technique has developed in to a diverse range of techniques spanning all energy-, and time- scales. The following techniques are used in this work.

3.1.1 μ–Raman Spectroscopy

Ultra low frequency Raman spectra were collected with samples at room temperature and under vacuum in a home-built free-space set-up. The system used a 100 mW 532 nm single mode DPSS laser manufactured by Cobolt, model 04–01 with a spectral linewidth <1 MHz, and wavelength stability of 2 pm over $\pm$ 2 °C and 8 hrs. This excitation source was attenuated to the desired power using a neutral density filter and checked before and after each measurement.

Polarisation optics designed for operation at the excitation wavelength in the configuration; $\frac{\lambda}{4}$ — LP — Sample — LP — $\frac{\lambda}{2}$, which allows arbitrary polarisation independent in excitation and analysis relative to the crystal axis, and in case of the use of high density gratings, matching with the spectrometer's holographic grating axis. The polarisation configurations that were used for experiments were the linearly co-polarised, and cross-polarised with Porto notations; $(\bar{z}(xx)z)$, $(\bar{z}(xy)z)$, respectively. The sample was mounted in a cryostat on a motorised $x-y$ positional stage and held under vacuum at room temperature for all Raman measurements.

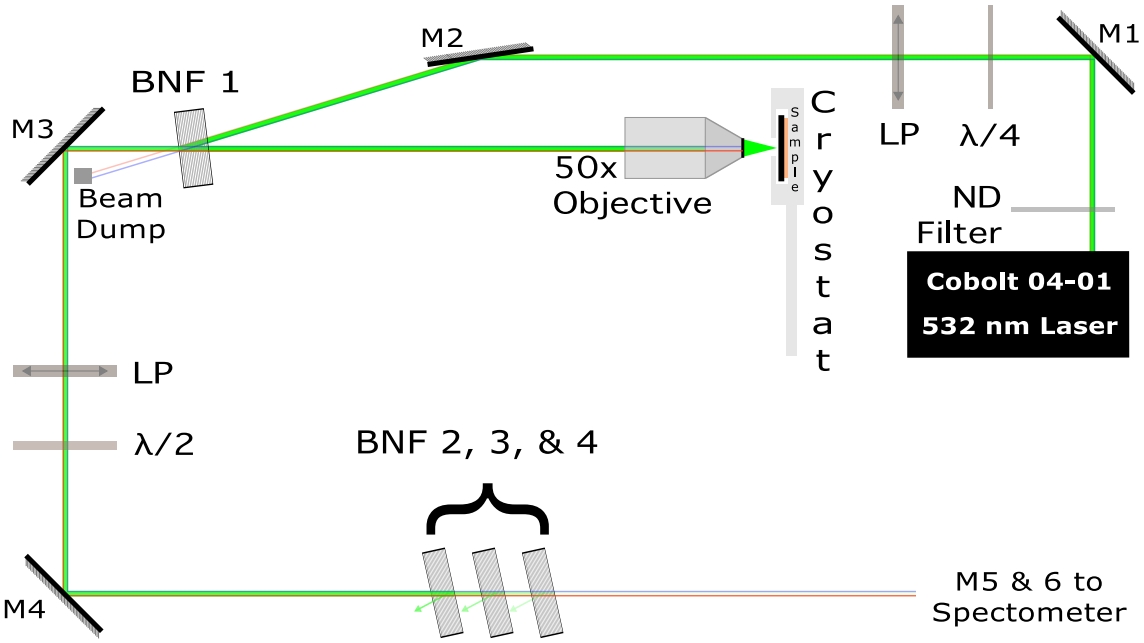

Figure 3.1: A schematic of the system used to perform μ-Raman spectroscopy: 'M' denotes a mirror; 'LP' a linear polariser; 'BNF's are Bragg notch filters; '$\lambda/4$', '$\lambda/2$' are quarter, and half waveplates, respectively. Red and blue lines indicate laser tails and noise rejected from the excitation path by transmission by 'BNF 1' and then absorbed by a beam dump; additionally they represent the sample's Raman signal, coupled to the spectrometer after BNF 4.

Rayleigh scattered light was rejected by the use of four Optigrate Bragg notch filters (BNFs); 'BNF 1' served the dual purpose of injecting the laser light into the backscattering axis, and along with the other three – 'BNF 2,3, & 4' – used to reject the laser in the collection path. The light was analysed using an $f-$matched Princeton Instruments SP750 0.75 m mirror spectrograph with a 1800 lines/cm grating dispersing light on to a back illuminated LN cooled Princeton instruments PyLon CCD. The optical path with significant intensity only comes to focus at the sample, under vacuum, preventing the observation of spurious Raman lines due to the Rotational modes of atmospheric species, especially N_2 or O_2. The low power of the signal at the spectrometer entrance slit focus produces negligible scattering. Laser power for Raman measurements was typically set at 0.5 mW to achieve negligible sample heating and sufficient signal:noise ratio. The spectral resolution of this system was ≈ 0.4 cm^{-1}, and the spatial resolution $\approx 1\mu$ m.

3.1.2 Photoluminescence Spectroscopy

Photoluminescence spectra were acquired from samples held under vacuum at room temperature from a home-built free space system. Multiple excitation sources were available, with 532 nm excitation used for this work. A single high NA 50x objective lens was used to focus the excitation and collect backscattered light. This light was analysed using a Princeton Instruments SP750 0.5m mirror spectrograph with a 300 lines/cm grating dispersing light on to a back illuminated LN cooled Princeton instruments PyLon CCD. Laser power for PL measurements

was at most 50 μW.

3.2 Atomic Force Microscopy

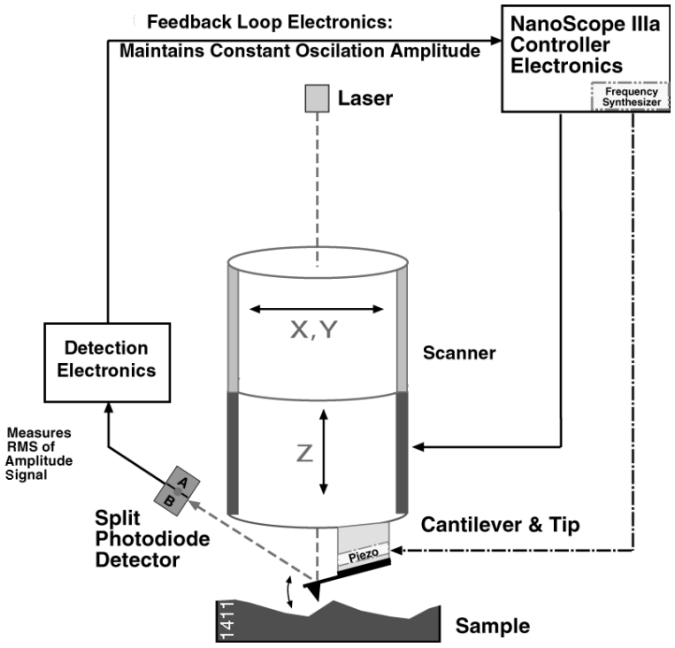

Figure 3.2: The basics of an AFM system. [Veeco]

Atomic Force Microscopy involves the use of an atomically fine tip to probe the topography of a sample, it is a powerful technique capable of yielding significant information about a sample, from magnetic properties, though to frictional and mechanical properties, all at the nanoscale.

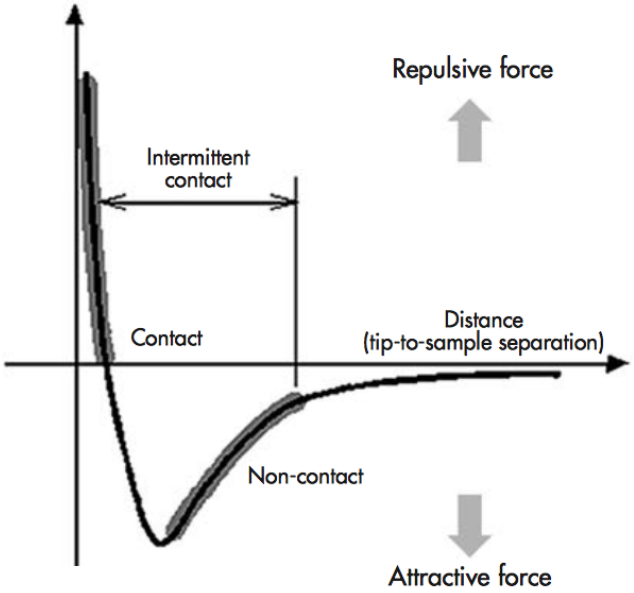

Figure 3.3: A typical force—separation graph for an AFM tip. [Veeco].

The probe tip is fabricated on the end of a small cantilever beam which deflects as it interacts with the sample; it is this deflection that is processed to image the sample. Several basic modes of operation exist in AFM, contact, non-contact, and tapping. Observation of figure 3.3, shows two highlighted regions where the tip—sample interactions are significant; in the contact regime (distance, $d < 1$ nm) the exchange interaction and Coulomb repulsion dominate and the net force is repulsive, in the non-contact regime (distance, $d > 1$ nm) van der Waals, dipole—dipole, and electrostatic interactions prevail and the net force is attractive.

The Tapping mode is essentially a hybrid of both contact and non-contact modes; the tip oscillated such that it intermittently comes into contact with the sample. The advantage of tapping is that it circumvents the risk of damaging the sample with the high force of contact mode, and the problem of snap down in non-contact mode where the ambient water meniscus pulls the tip down into contact. Tapping mode is used exclusively in the following work.

The atomic tip of the probe requires very precise control and the apparatus involved is detailed in figure 3.2. The entirety of the actuation of the tip is performed by piezoelectric crystals, for the precision they afford, from the raster scanning of the tip, to the oscillation of the cantilever. The deflection of the cantilever is probed as a light lever, using a laser reflected on to a photodiode array.

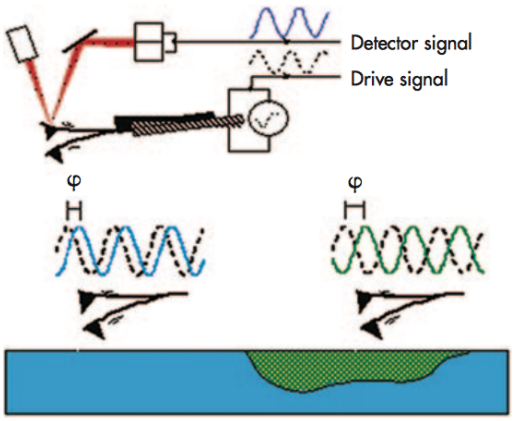

Figure 3.4: The principle of phase imaging, pictorially represented.

In tapping mode the cantilever is driven just below its resonant frequency $(50 - 500kHz)$, to achieve the highest resolution of the system, and is typically operated in an amplitude modulated fashion, where the dedicated feedback electronics modulate the height in order to maintain a constant cantilever amplitude. It is this modulation in height, the phase of the cantilever oscillation relative to the drive (figure 3.4), and the amplitude of the oscillations that are recorded and used to build images of the sample.

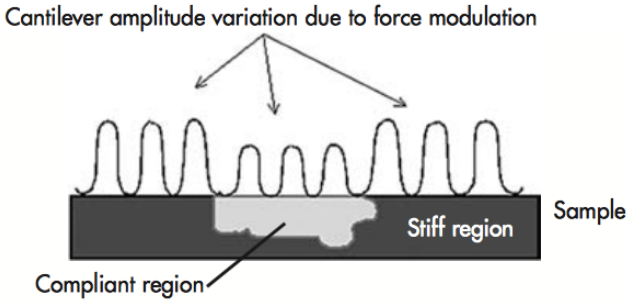

Figure 3.5: Artefacts may arise in the height profile where compliant regions are present, this indicates the importance of the amplitude data.

Part II

Results of Experimental Studies

Chapter 4

Raman Studies of $Mo_xW_{(1-x)}S_2$ Alloys

4.1 Introduction

Semiconductor alloys have long been a useful method of engineering the band gaps and Fermi levels of dielectric materials for use in building optoelectronic devices. In the field of 2D materials, where there exist a large number of materials with diverse bandgaps and optical properties 4.1, the ability to produce alloys in such systems heralds a means to produce a greater spectrum of bandgaps for implementation in the growing technological applications of 2D materials. Understanding the excitonic properties and the Raman dependencies as a function of alloy content is therefore necessary.

Ultra low frequency Raman spectroscopy, and its sensitivity to the interlayer vibrations present in van der Waals materials, provides a technique to determine accurately the alloy content in the $Mo_xW_{(1-x)}S_2$ alloy system, with greater specificity and ambiguity than high-frequency modes.

Presented in this chapter is a comprehensive optical study of the $Mo_xW_{(1-x)}S_2$ alloy system at room temperature and under vacuum; from photoluminescence and reflectance contrast to the high-, and low-frequency Raman response.

The bulk material was grown by HQ Graphene (Groningen, Netherlands) and characterised by EDX data and high-frequency Raman. The nominal concentrations were derived from the targeted growth stoichiometry, and do not agree with the EDX data perfectly. Samples were prepared using tape exfoliation from bulk on to PDMS films, after which suitable flakes could be measured for room temperature photoluminesence, or transferred on to 90 nm SiO_2 on Si substrates for reflectance contrast, and Raman studies.

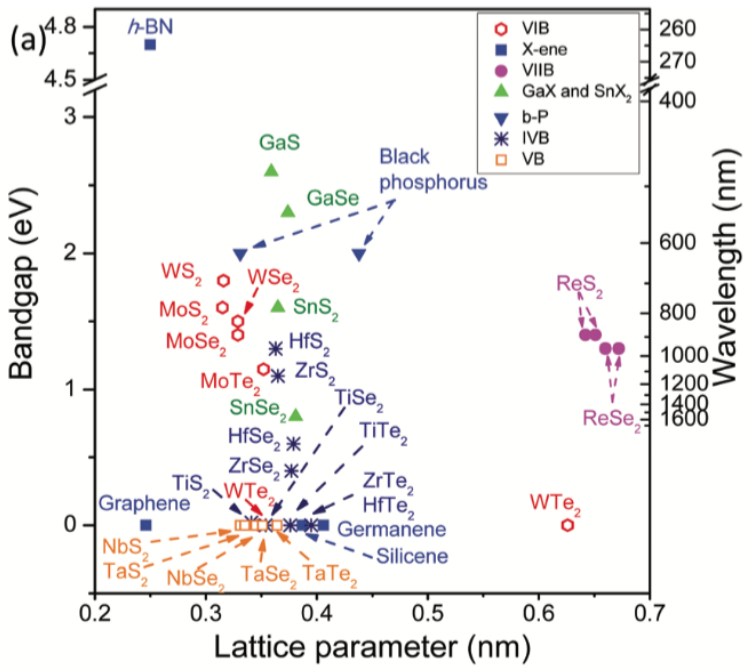

Figure 4.1: Diversity in the excitonic bandgaps as a function of in-plane lattice parameter for various 2D materials, from ref. [1].

4.2 Results and Discussion

4.2.1 Excitonic Optical Response

Reflectance contrast (RC) spectra shown in figures 4.2(b), and 4.4 show features due to optical absorption by band edge excitonic resonances of TMDs, the two distinct resonances; A- (2.01–1.91 eV), and B- (2.41-2.04 eV); result from valence band spliting due to spin orbit coupling [2]. In figure 4.4, the broader spectral range captures a lower energy absorption band corresponding to the indirect exciton which red-shifts with increasing layer number.

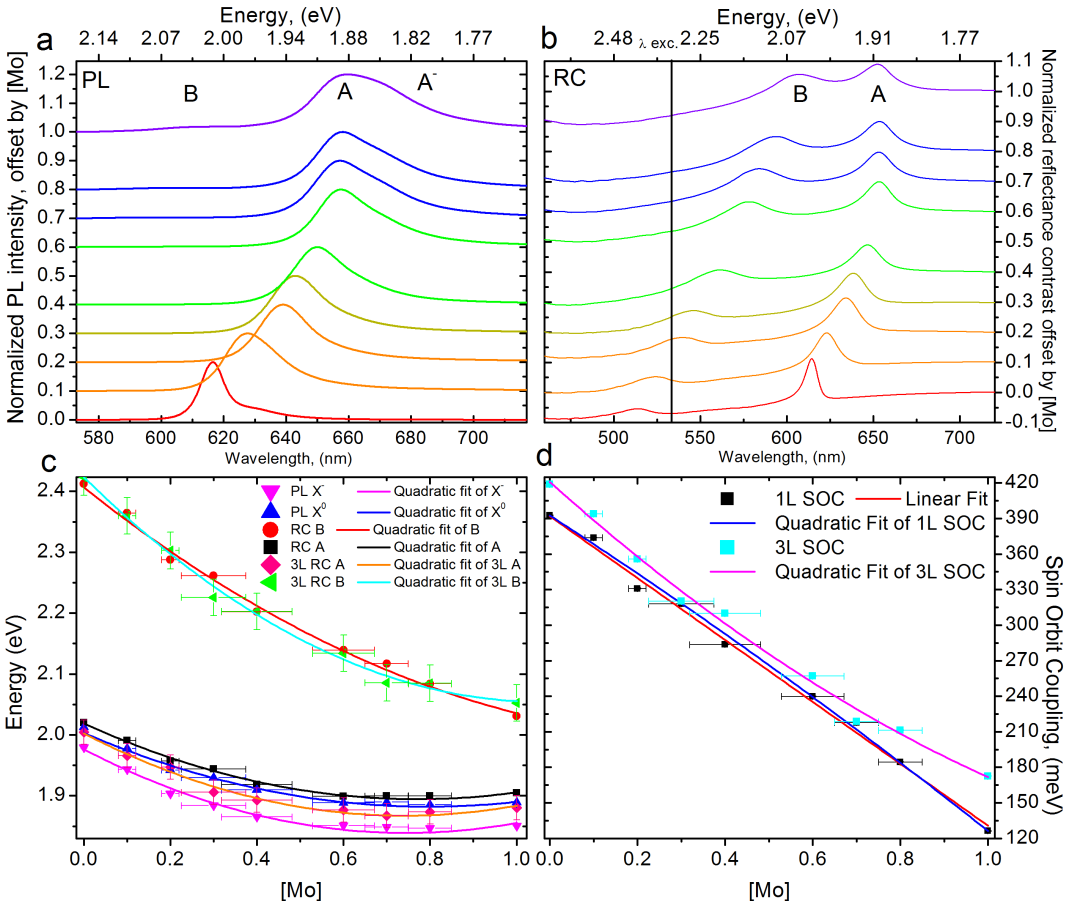

Figure 4.2: (a) Photoluminescence; (b) Reflectance contrast measurements; (c) composition dependence of excitonic resonances; and (d) the extracted spin orbit splitting between A and B resonances for exfoliated mono-layer and tri-layer $Mo_xW_{(1-x)}S_2$. The vertical line in (b) depicts the excitation wavelength (532 nm, 2.33 eV) used in this work. The results of the quadratic fits of the bowing effect from (c) can be seen in 4.1, including the results for tri-layer. All adjusted R–Square values are above 0.98, and reduced χ^2 values below 3×10^{-7}. The spin orbit coupling extracted from RC measurements in (c) is shown in (d), and plotted with both a linear and quadratic fits, with adjusted R–Square values of 0.995, & 0.996 respectively.

From room temperature photoluminescence (PL) spectra in figure 4.2(a), A and B excitons are radiative, in the monolayer the lower energy A exciton provides the bulk of the quantum yield though direct luminescence and the B exciton radiates via a hot luminescence process involving acoustic phonons. The A peak appears asymmetric in room temperature PL measurements due to the presence of a negative trion state, A^-, due to n-dopants [3], this asymmetry is consistent and suggests that doping is not significantly modified by Δ[Mo] under the fabrication conditions of these alloys. In bi-, and tri- layer flakes, the excitonic ground state is an indirect transition near the Γ point of the Brillouin zone as can be seen in figure 4.3. In the case of multi-layer flakes, emission from both A and B excitons is due to hot luminescence as carriers around the K points recombine before fully relaxing [4].

In many semiconductor alloy systems the optical band gap can be observed to be parabolically modulated by alloy concentration due to the different electronegativities of the alloy species, and the modification to the periodicity of the lattice [5], this effect can be described by the equation [6];

$$E_{PL(Mo_xW_{1-x}S_2)} = (1-x)E_{PL(x=0)} + xE_{PL(x=1)} - bx(1-x) \tag{4.1}$$

.

The so-called bowing parameter b descibes four times the deviation of $E_{PL(Mo_xW_{(1-x)}S_2)}$ from linearity at equi-molar concentration $[Mo] = 0.5$, and in most semiconductor alloy systems the bowing parameter varies from a few meV to 3 eV [7]. Table 4.1 shows the values extracted from fitting equation 4.1 to the mono-layer, and tri-layer data shown in figures 4.6 & 4.5, respectively.

Fit	$E_{PL(x=0)}$ (eV)	$E_{PL(x=1)}$ (eV)	Bowing Parameter, b (meV)
PL A^-	1.97±0.01	1.86±0.01	238±26
PL A^0	2.01±0.01	1.89±0.01	209±20
RC A	2.02±0.01	1.91±0.01	214±16
RC B	2.41±0.01	2.04±0.01	199±39
PL 3L A	1.93±0.01	1.85±0.01	104±28
RC 3L A	2.00±0.01	1.88±0.01	245±23
PL 3L B	2.35±0.08	1.98±0.02	132±169
RC 3L B	2.42±0.01	2.06±0.01	328±40
PL 3L I	1.75±0.02	1.56±0.03	149±97
Ref.[8] B exp.	2.36	1.98	190±60
Ref.[8] A exp.	1.99	1.85	250±40
Ref.[8] A calc.	–	–	280 ± 40
Ref.[9] A exp.	2.02±0.01	1.89 ±0.01	250±30
Ref.[10] A exp.	2.02±0.01	1.89±0.01	≈ 260

Table 4.1: Fit results of bandgap bowing equation 4.1 applied to PL data in figure 4.2, compared with values from literature.

Values for the bowing parameters for $Mo_xW_{(1-x)}S_2$ from other works [8]–[10] concord within the error margins. Comment should be made on the fact that this work reports data for the A^0 and A^- separately, having resolved the emission from the two complexes through fitting of the PL data: The derived bowing parameter for the A^0 emission is smaller, but the bowing of the A^- complex provides a closer match with previous results, especially for ref. [8] where the emission energies of MoS_2 and WS_2 match best with the A^- PL, suggesting significant doping in their samples.

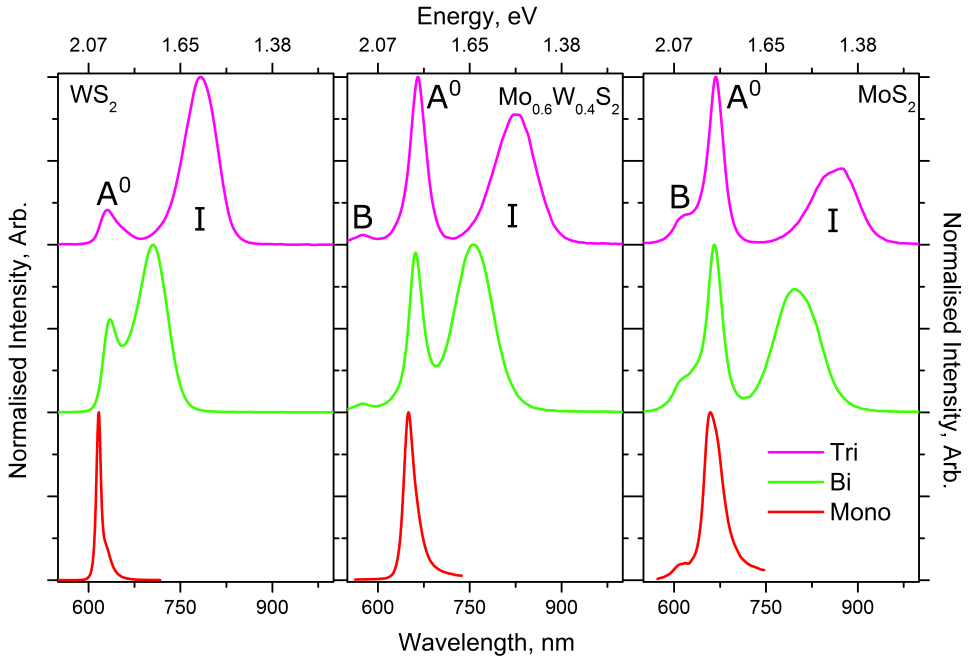

Figure 4.3: Normalised photoluminescence spectra for mono-, bi-, and tri- layer; leftmost, WS_2; middle, $Mo_{0.6}W_{0.4}S_2$; and rightmost, MoS_2. Excitation wavelength; 532 nm, 2.33 eV.

The extracted SOC coupling for the mono-layer in figure 4.2(d) suggests a small degree of bowing; (−27.3±11.3) meV, which is not expected from theoretical evaluation omitting SO effects, and previous experimental studies on the $Mo_xW_{(1-x)}S_2$ system having not observed this effect. However, in the $Mo_xW_{(1-x)}Se_2$ system where the SO effects are much more pronounced, a significant SOC bowing is observed [11], thus, in $Mo_xW_{(1-x)}S_2$ this effect should also be non-zero. For the tri-layer case in figure 4.2(d) the extracted bowing parameter is considerably larger and of opposite sign, (83±29) meV.

Figures 4.3, 4.4 & 4.5 demonstrate the progression of the excitonic resonances with differing layer thickness. Figure 4.3 shows photoluminescence response with the presence of the indirect exciton peak, labelled as 'I', which manifests as a much broader feature in the reflectance contrast measurements of figure 4.4. The fitted peak centres of trilayer are plotted as a function of [Mo] in figure 4.5, and the parameters of the parabolic fit are compared with monolayer values in table 4.1.

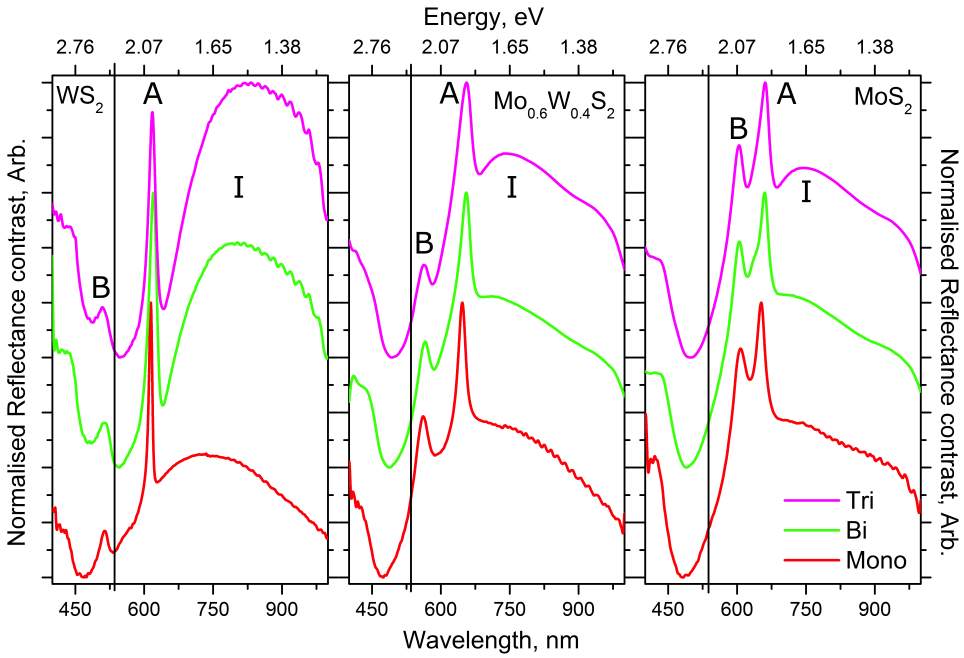

Figure 4.4: Normalised reflectance contrast spectra for mono-, bi-, and tri- layer; leftmost, WS_2; middle, $Mo_{0.6}W_{0.4}S_2$; and rightmost, MoS_2. The excitation wavelength for Raman and PL studies is marked with a vertical, solid black line at 532 nm, 2.33 eV.

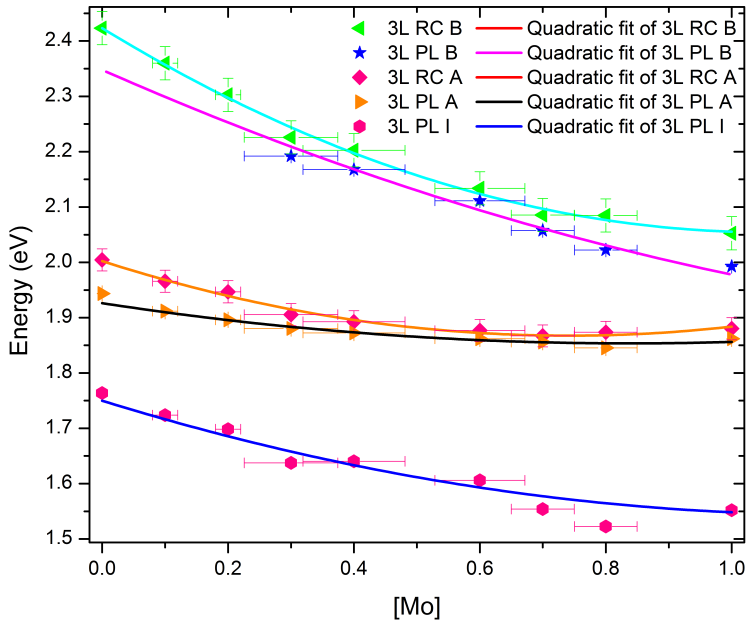

Figure 4.5: Extracted peak positions from RC and PL measurements on exfoliated 3L $Mo_xW_{(1-x)}S_2$ showing the quadratic fits of the data, the results of which can be seen in table 4.1.

4.2.2 Raman Response

This study uses 532 nm laser excitation for both Raman and PL, providing a pumped resonance of the B exciton for [Mo]<0.4; under resonance, selection rules for Raman processes are greatly relaxed due to the product of the space group symmetries of the participating excitations – in this case excitons and phonons – resulting in a greater number of symmetric elements contained in the Raman tensor. Additionally the $Q = 0$ condition of Raman scattering is relaxed for second order modes by the uncertainty present in the exciton momentum [12].

Since the symmetry groups for the bulk and few-layers of TMDs in question are different, the notations used for peak assignment should strictly also differ, though they originate from similar vibrational modes [13]–[15]. To ease communication, however, the peak notations for bulk material will be followed.

High Frequency Raman

In figure 4.6(a) co-polarised, high-frequency spectra for tri-layer samples are shown, normalised to the highest intensity Raman mode: 2LA(M) for WS_2, and A_{1g} for [Mo]>0. Prominent intra-layer optical phonon E_{2g} and A_{1g} peaks are observed in the ranges (350–385) cm^{-1} and (400–420) cm^{-1}, respectively. Trilayer Raman data is used to demonstrate the trends present in mono- and bi-layer flakes, and was chosen for the improved signal:noise and the clarity and reliability of the data and resulting fits and analysis. In WS_2 and low [Mo] samples there appears an additional double-resonant peak due to the 2LA(M) Phonon mode at ≈ 350 cm^{-1}. Panel (b) of figure 4.6 shows the cross-polarised spectra in the same wavenumber range, in such configuration only the out of plane E modes are present, and a clear two-mode dependence can be observed, the peak positions of which are in the figure 4.6(e).

The trends of the first order optical high-frequency Raman modes are in agreement with previous reports [10], [16]. But it is noted that in addition to the previously observed two mode behaviour of the E_{1g} peaks, the A_{1g} peak can also be decomposed into two peaks, overlapping to produce the appearance of single mode behaviour (fig.4.6(c,e)). This suggests that disorder of the alloy domains may not be as great as had been assumed previously from consideration of the Raman linewidth broadening, as would be the case due to finite domains relaxing the $Q = 0$ condition of Raman scattering.

The form of the trends of the mode frequencies of both MoS_2-, & WS_2- like modes in figure 4.6 c, and e, for both A_{1g}, & E_{2g}, fit to sigmoid and cubic functions with Adj. R-Square values ranging from (0.989–0.999). The higher frequency branches – WS_2 A_{1g}, & MoS_2 E_{2g} take the sigmoid form, whilst the lower frequency branches – WS_2 E_{2g}, & MoS_2 A_{1g} – take cubic forms. Modified random-element-isodisplacement (MREI) modeling does not predict these subtleties [16]; it excludes bi-modal behaviour of A_{1g} and provides fits less accurate than presented here. Looking for explanation in the phonon dispersions of MoS_2 and WS_2 (ref.[17] (figures 2.6 &

2.5)) one might speculate that an avoided crossing of the phonon branches between Γ & M points of the Brillouin zone could modify the Raman active modes observed at $Q = 0$.

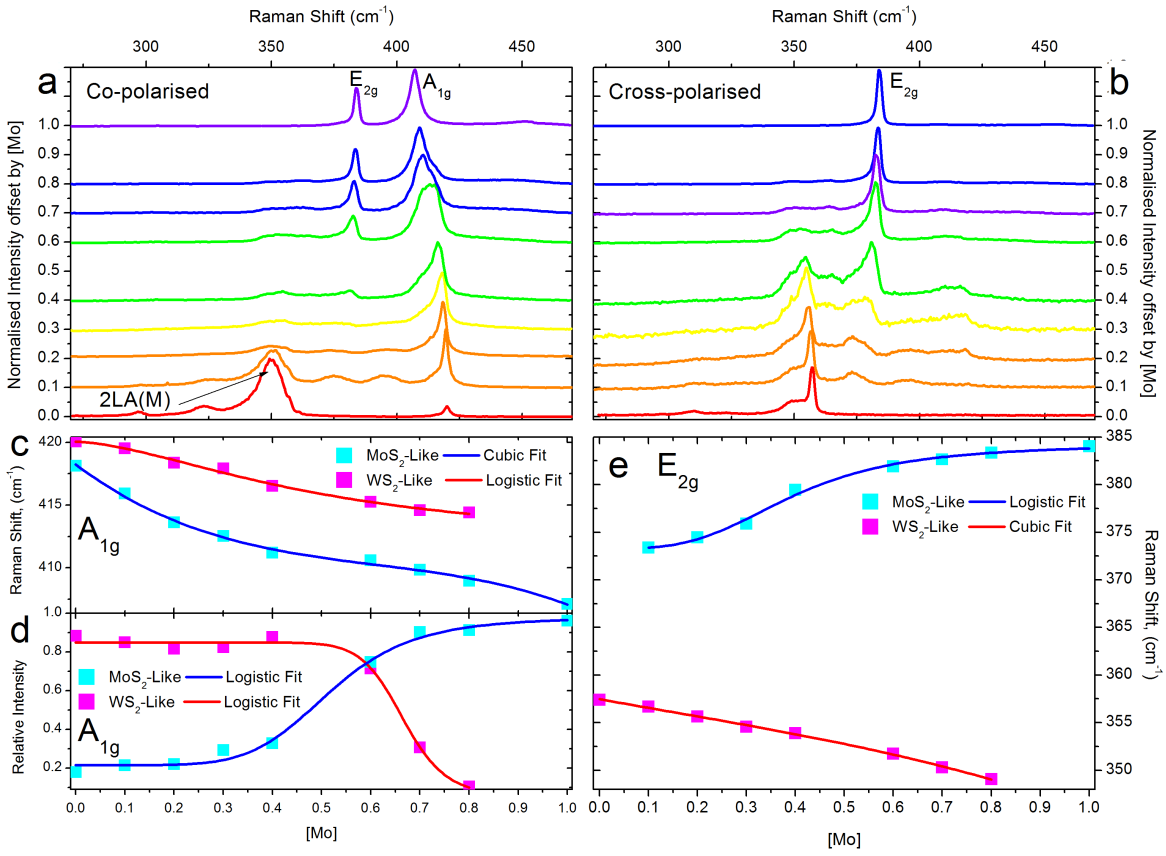

Figure 4.6: Raman response in the high frequency for tri-layer $Mo_xW_{(1-x)}S_2$ in both co-polarised, $A+E$ symmetry, (a); and cross polarised, E symmetry, (b); scattering configurations. Panels (c) & (e) show the extracted peak positions for (c); A_{1g}, and (e) E_{2g} first order Raman modes, demonstrating the two mode behaviour. (d) Shows the relative intensities of the two A_{1g} components, showing a sigmoidal dependence.

The relative intensities of the bi-modal fitting of the A_{1g} peak concord with sigmoidal functions (figure 4.6 d), often seen in autocatalytic processes, this non-linearity represents the entropy of the system, in that the phonon populations of a given mode (WS_2–like or MoS_2–like) are unstable where the mixing of Mo and W elements is greatest, and phonon correlation length lowest. The impact of the disorder at intermediate [Mo] and the additional phonon confinement may be the cause of the modification of the Raman peak positions from linear trends predicted by MREI. This deviation from theory may be explained in considering the experimental in plane lattice parameters, which in MoS_2 are $a = 3.148$ Å [18] and in the case of WS_2, $a = 3.153$ Å [19], a mismatch of only 0.2%. The maximum strain can be estimated in the same way $\varepsilon = \frac{a-a_0}{a_0}$ [20], from first principles calculations by density-functional perturbation theory (DFPT) on MoS_2 Raman shifts are altered by ± 4 cm^{-1} at $\varepsilon = \pm 1\%$ [21], by reasonably assuming Hooke's law

and linearity at small strains, the modification at 0.2% should be of the order of 0.8 cm^{-1} which would be close to satisfying the deviations from linearity observed in the E_{2g} & A_{1g} Raman peak shifts as a function of [Mo].

Ultra Low Frequency Raman

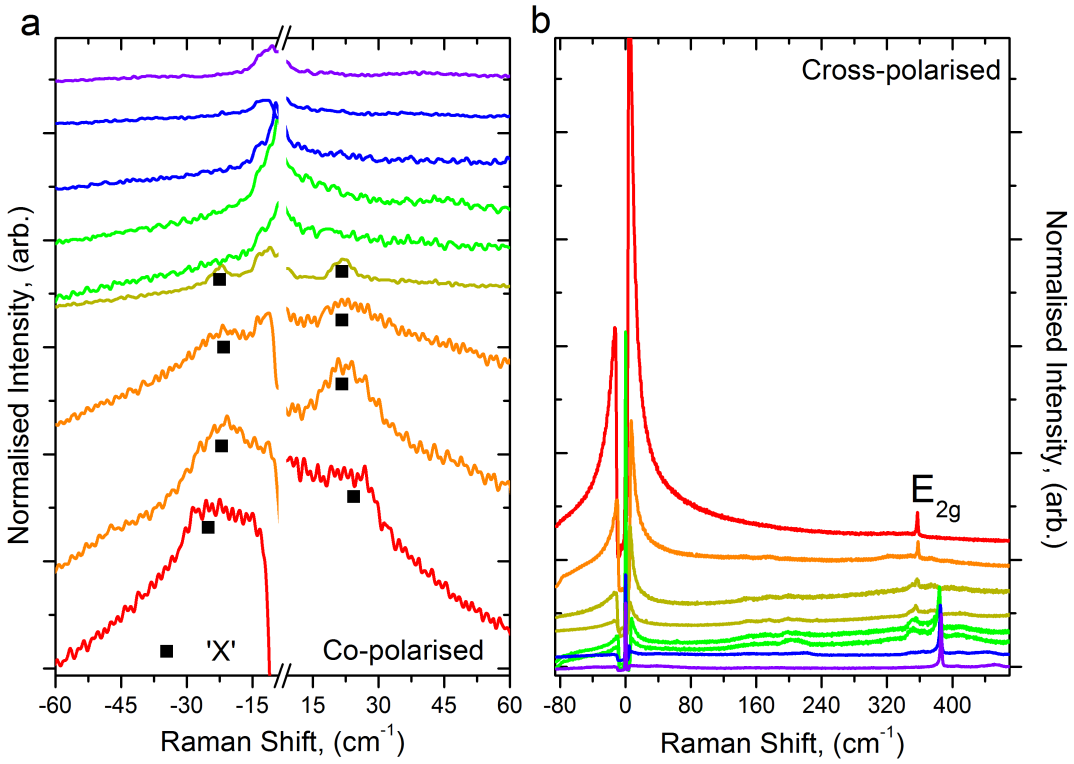

Figure 4.7: Monolayer $Mo_xW_{(1-x)}S_2$ Raman response; (a) Low-frequency co-polarised, and (b) Full range cross-polarised. Interlayer modes are absent in the monolayer, allowing clear observation of 'peak X' in (a). Hot luminescence tails from the B-exciton can be seen in (b), the order of the plotted spectra has been reversed for clarity, with the red trace as the [Mo] = 0 through to the Purple trace with [Mo] = 1.

Ultra-low-frequency (ULF) Raman spectra for mono-layer samples are shown in figure 4.7, normalised in the acquisition time. In panel (a) co-polarised data are shown; in the mono-layer, there are no optical phonon modes present in the ULF however, excitation resonant with the B-exciton produces a peak – termed as 'Peak X' in the literature – at 28 cm^{-1} in WS_2, which red-shifts with increasing [Mo] and disappears for [Mo]>0.3. The purpose of the cross-polarised data in figure 4.6(b) is to demonstrate the hot-luminescence tails due to the B-exciton resonance, these are asymmetric about 0 cm^{-1} and due to the Stokes and anti-Stokes scattering from the continuous populations of acoustic phonons from the exciton complex.

Bi-layer ULF spectra are presented in figure 4.8, the co-polarised spectra in panel (a) show both shear ($\approx$ 20 cm^{-1}), and breathing – (30:45) cm^{-1} – interlayer modes, both modes blue-

shift with increasing [Mo]. For low [Mo] the resonant peak masks the presence of the inter-layer modes. In the cross-polarised configuration, the shear mode is the only inter-layer mode present, in [Mo]=(0,0.1) spectra a resonant peak 2X can be observed at ≈ 45 cm^{-1}. The inter-layer peak positions are summarised in figure 4.10(b).

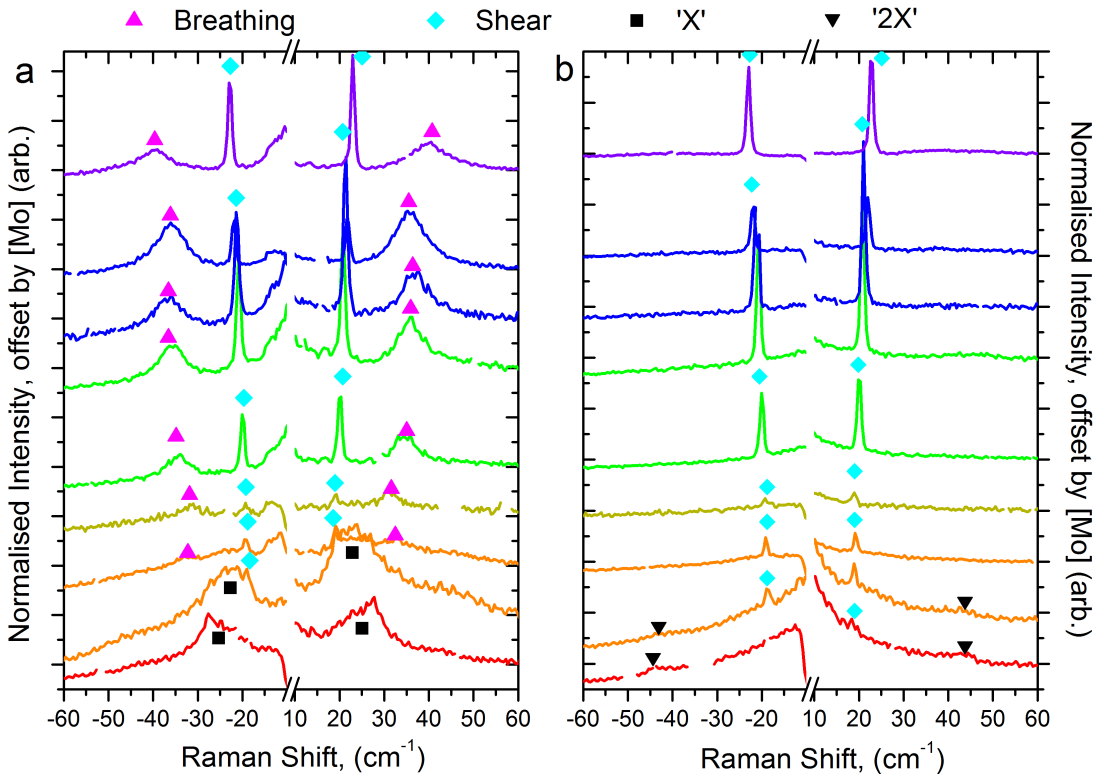

Figure 4.8: Bilayer $Mo_xW_{(1-x)}S_2$ low frequency Raman response; (a) co-polarised, and (b) cross-polarised. Both shear (cyan rhombus) and breathing (magenta triangle) interlayer modes are present in the spectra [Mo]$<$ 0.4, but are masked by the 'peak X' feature (black squares). Hot luminescence tails from the B-exciton can be seen to be quenched relative to the monolayer, with shear modes and a feature 2X (black triangles) at 45 cm^{-1}(b).

Tri-layer ULF Raman response can be seen in figure 4.9, at this layer-number the shear, and breathing modes have approximately the same frequency, with breathing modes contributing broad tails to the shear mode peaks. No splitting of the degenerate shear/breathing mode peak is seen as a function of [Mo] suggesting that there is no significant change in the interlayer coupling with the substitution of metal atoms in the lattice. Contributions from neighbouring flakes of different thickness (bi-, and quad- layer) are marked with asterisks. Non-inter-layer resonant features are observed for [Mo]$<$0.3. In [Mo]=0.3, where the excitation is slightly above resonance the appearance of a Raman mode at 13 cm^{-1} is seen in in the tri-layer cross polarised spectrum (fig.4.9 b, marked with an orange star). This peak at 13 cm^{-1} is not considered by theories considering only optical phonons [13], [22], but is predicted by more simple models taking in to account intra-layer forces and considering acoustic phonons [14]: Observation has been made of a similar mode in trilayer MoS_2 under resonant excitation [23]. This study's

polarisation resolved measurements suggests this mode is a shear mode of the C_2^- branch in the diatomic chain model (DCM). In the Tri-layer this peak belongs to the E_u symmetry which should be forbidden in backscattering geometry, this constraint is lifted by the prescence of Wannier excitons in TMDs [24] by Fröhlich electron—phonon interaction [25]. Another example of these higher order acoustic layer vibrations is seen in figure 4.9 (a), magenta star, where an additional breathing mode is observed at ≈ 40 cm $^{-1}$ this corresponds to the first LB_2^- mode, and is often observed in mixed 2H/3R trilayers [26], [27]. Modification of the frequencies of the low frequency Raman modes can be seen in figure 4.10(b), where the trend is adequately explained by the change in mean density, μ; $\omega \propto \sqrt{1/\mu}$, due to proportional substitution of tungsten atoms with those of molybdenum. The fitted lines take in to account the mode frequencies in WS_2 and then scales the mass as a function of [Mo].

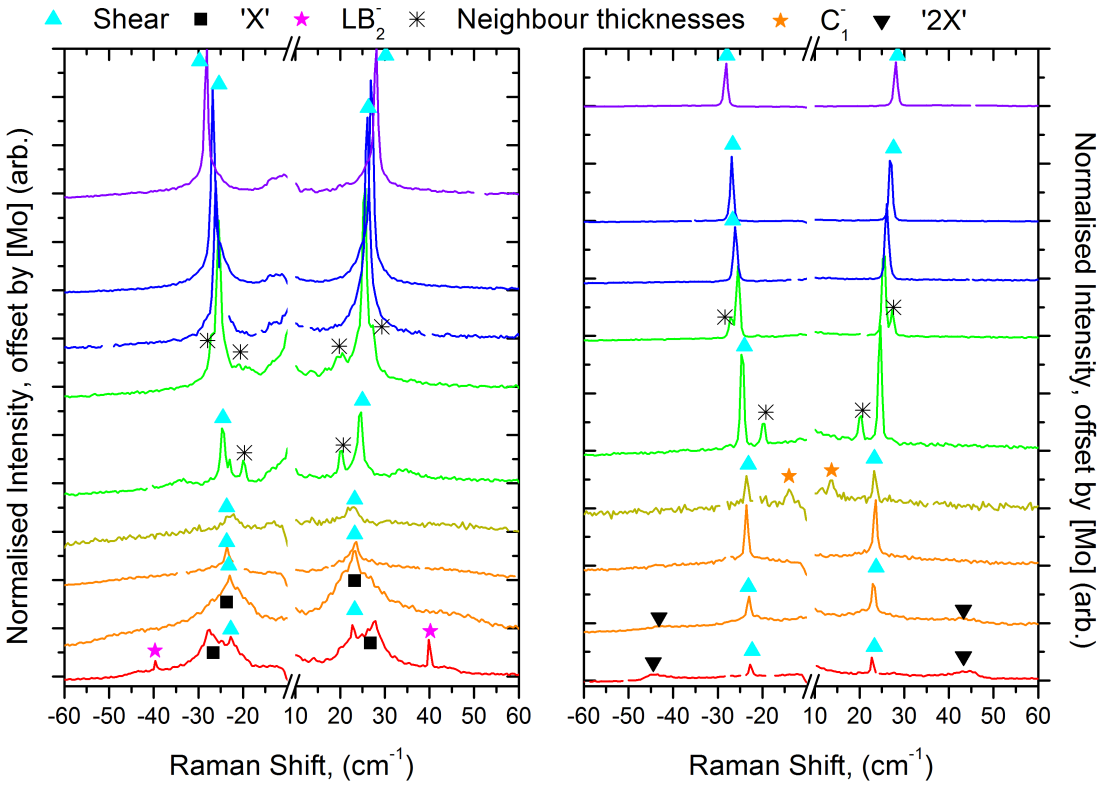

Figure 4.9: Trilayer $Mo_xW_{(1-x)}S_2$ Low frequency Raman response; (a) co-polarised, and (b) cross-polarised. (a) Both shear and breathing interlayer modes (cyan rhombus, degenerate) are present in the spectra [Mo]< 0.4, but are masked by 'peak X' (black square). The magenta stars indicate a resonantly enhanced breathing mode. (b) Hot luminescence tails from the B-exciton can be seen to be quenched relative to the monolayer case, there are additional shear modes (orange stars) and a feature 2X (black triangle) at 45 cm^{-1}(b). Contributions from neighbouring flakes of different thickness (bi-, and quad- layer) are marked with asterisks.

Discussion of Peak X

Whilst the resonance condition appears to be met equally well for all [Mo]< 0.4 the hot luminescence in the monolayer and all resonant Raman features only decrease in intensity with increasing [Mo] (figure 4.7). The change in the hot luminescence could be due to the non radiative relaxation processes to the excitonic ground state become more significant with increasing [Mo].

From the WS_2 Raman shift of ≈ 28 cm^{-1} 'peak X' tunes away from the shift reported for MoS_2 (38 cm^{-1}) [22], with increasing [Mo] rather than towards this value. 'Peak X' cannot be attributed to collective electric carrier oscillations, the so-called plasmon mode, or other collective modes such as the charge density wave (CDW), all of which are excluded by the thickness independence of the feature whilst Coulomb screening and interlayer coupling are substantially modified with thickness.

For a time, the prevailing explanation for the low frequency resonant Raman 'peak X' as being due to a spin-flip within the SOC split conduction band [22] should be incorrect: not only do circularly polarised Raman measuments disagree [23] but the conduction band splitting between WX_2s and MoX_2s is of different magnitude, and opposite sign , 27 meV & -3 meV, respectively [28]–[30]. Similarly, resonant Raman scattering in WSe_2 shows a peak at ≈ 19 cm^{-1} [31], not at all commensurate with its much larger conduction band spin orbit induced splitting. Whilst 'peak X' does tune in energy with increasing [Mo], it decreases in intensity incommensurately with 2LA(M), suggesting a direct link to the acoustic phonon mode LA(M) [32] might not be the case and that some other candidate mode should be considered. Recently it has been suggested that acoustic phonons (TA and LA) are responsible, but the main justification being that the ratio of group velocities of these modes is similar to the Raman shift ratios, and it remains unclear how the specific momentum value of these modes is selected, given the factor ≈ 300 difference between the incident light's wavevector $k \approx 10^5$ cm^{-1} and that of the phonons $k \approx 3 \times 10^7$ cm^{-1} at their given energy [33]. It might be worth considering what processes involving excitons could contribute the momentum to couple to specific acoustic phonon energies, a Rashba-type splitting is predicted at Γ [30] and has been observed with applied electric field [34], in polar TMDs [35], and used to explain indirect exciton recombination processes [36].

Observation of coherent lattice vibrations has been made in mono- and few-layer WSe_2 in the time domain, obtained by performing time-resolved transmission measurements, resonant with the A–exciton [37]. However, there was no report of any sign of 'peak X' in the spectrum, which would be the case were the peak due to some Lamb mode [38]–[40], in addition, a Lamb mode should be dependent on thickness.

Most probably the explanation lies in the exciton—polariton picture, where scattering between branches allows coupling to the specific momentum values of the LA and TA phonons, this principle has been effective in explaining annomolous resonant Raman effects in TMDs in

the past [41].

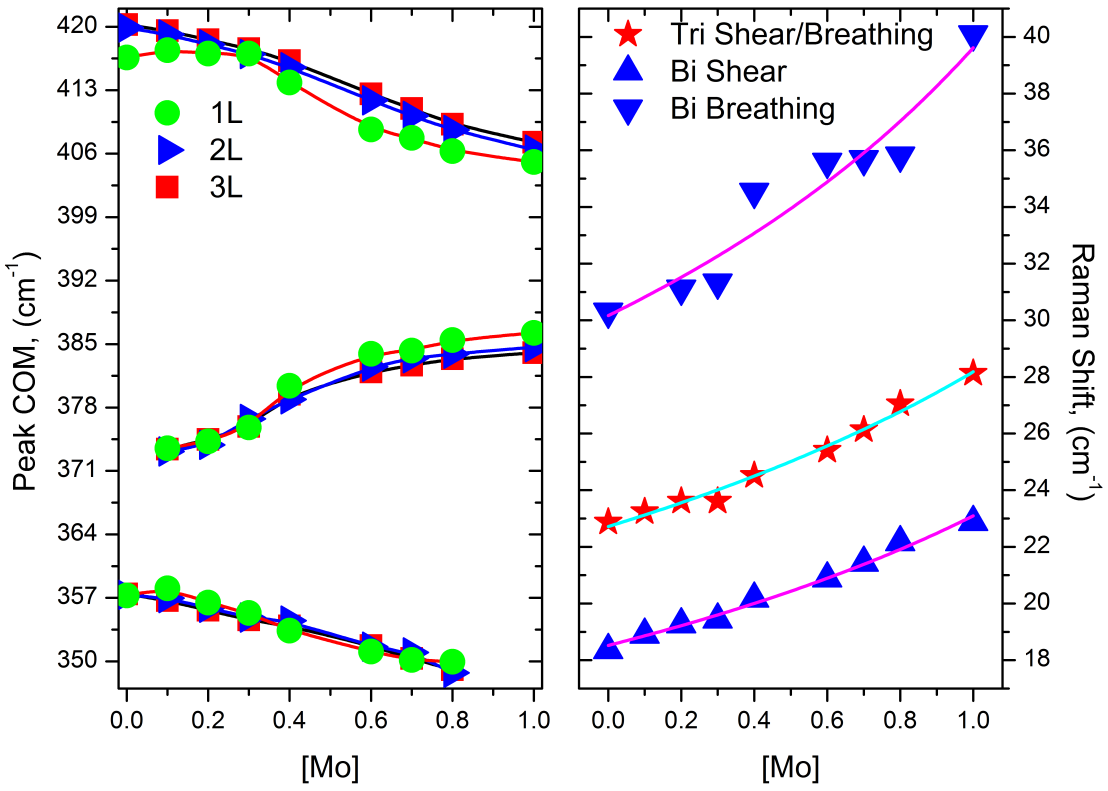

Figure 4.10: Extracted Raman mode frequencies plotted against [Mo]. (a) High frequency intra-layer modes show non-linear trends. (b) Inter-layer modes tune with the change in mean density.

4.3 Summary

In summary, these results provide a confirmation of the behaviour of the excitonic properties of $Mo_xW_{(1-x)}S_2$, and some evidence of the bowing of the spin orbit coupling in monolayer transition metal sulphide alloys.

The Raman measurements performed in this system allow characterisation with unprecedented resolution, highlighting deviations in the high frequency A_{1g} optical phonon mode from theoretical predictions, and previous experimental studies. In the low frequency, the data has confirmed that the trend in the shear and breathing layer modes between WS_2 and MoS_2 is well described by the modification in the density due to the difference in atomic mass of molybdenum and tungsten.

The resonant excitation for [Mo]<0.4, highlights new evidence for the understanding of the 'Peak X' feature; that it does not tune towards its value in MoS_2 was a property hitherto unreported.

References

[1] L. Xie, "Two-dimensional transition metal dichalcogenide alloys: preparation, characterization and applications," *Nanoscale*, vol. 7, no. 44, pp. 18 392–18 401, 2015, ISSN: 2040-3364. DOI: 10.1039/C5NR05712D. [Online]. Available: http://xlink.rsc.org/?DOI=C5NR05712D.

[2] A. Ramasubramaniam, "Large excitonic effects in monolayers of molybdenum and tungsten dichalcogenides," *Physical Review B - Condensed Matter and Materials Physics*, vol. 86, no. 11, pp. 1–6, 2012, ISSN: 10980121. DOI: 10.1103/PhysRevB.86.115409. arXiv: 1403.3771.

[3] K. F. Mak, K. He, C. Lee, G. H. Lee, J. Hone, T. F. Heinz, and J. Shan, "Tightly bound trions in monolayer MoS_2," *Nature Materials*, vol. 12, no. 3, pp. 207–211, Dec. 2012, ISSN: 1476-1122. DOI: 10.1038/nmat3505. arXiv: 1210.8226. [Online]. Available: http://www.nature.com/doifinder/10.1038/nmat3505.

[4] K. F. Mak, C. Lee, J. C. Hone, J. Shan, and T. F. Heinz, "Atomically thin MoS_2: A new direct-gap semiconductor," *Physical Review Letters*, vol. 105, no. 13, pp. 2–5, 2010, ISSN: 00319007. DOI: 10.1103/PhysRevLett.105.136805. arXiv: 1004.0546.

[5] W. J. Yin, X. G. Gong, and S. H. Wei, "Origin of the unusually large band-gap bowing and the breakdown of the band-edge distribution rule in the Snx Ge1-x alloys," *Physical Review B - Condensed Matter and Materials Physics*, vol. 78, no. 16, pp. 1–4, 2008, ISSN: 10980121. DOI: 10.1103/PhysRevB.78.161203.

[6] J. V. Vechten and T. K. Bergstresser, "Electronic structures of semiconductor alloys," *Physical Review B*, vol. 1, no. 8, pp. 3351–3358, 1970, ISSN: 01631829. DOI: 10.1103/PhysRevB.1.3351. [Online]. Available: http://dx.doi.org/10.1103/PhysRevB.1.3351.

[7] B. Fluegel, S. Francoeur, A. Mascarenhas, S. Tixier, E. C. Young, and T. Tiedje, "Giant Spin-Orbit Bowing in $GaAs_xBi_{(x-1)}$," *Physical Review Letters*, vol. 97, no. 6, p. 067 205, Aug. 2006, ISSN: 0031-9007. DOI: 10.1103/PhysRevLett.97.067205. [Online]. Available: https://link.aps.org/doi/10.1103/PhysRevLett.97.067205.

[8] Y. Chen, J. Xi, D. O. Dumcenco, Z. Liu, K. Suenaga, D. Wang, Z. Shuai, Y.-S. Huang, and L. Xie, "Tunable Band Gap Photoluminescence from Atomically Thin Transition-Metal Dichalcogenide Alloys," *ACS Nano*, vol. 7, no. 5, pp. 4610–4616, May 2013, ISSN:

1936-0851. DOI: 10.1021/nn401420h. [Online]. Available: http://pubs.acs.org/doi/abs/10.1021/nn401420h.

[9] J.-G. Song, G. H. Ryu, S. J. Lee, S. Sim, C. W. Lee, T. Choi, H. Jung, Y. Kim, Z. Lee, J.-M. Myoung, C. Dussarrat, C. Lansalot-Matras, J. Park, H. Choi, and H. Kim, "Controllable synthesis of molybdenum tungsten disulfide alloy for vertically composition-controlled multilayer," *Nature Communications*, vol. 6, p. 7817, Jul. 2015, ISSN: 2041-1723. DOI: 10.1038/ncomms8817. [Online]. Available: http://www.nature.com/ncomms/2015/150723/ncomms8817/full/ncomms8817.html%20http://www.nature.com/doifinder/10.1038/ncomms8817.

[10] Z. Wang, P. Liu, Y. Ito, S. Ning, Y. Tan, T. Fujita, A. Hirata, and M. Chen, "Chemical Vapor Deposition of Monolayer $Mo_{(1-x)}W_xS_2$ Crystals with Tunable Band Gaps," *Scientific Reports*, vol. 6, no. 1, p. 21 536, Aug. 2016, ISSN: 2045-2322. DOI: 10.1038/srep21536. [Online]. Available: http://www.nature.com/articles/srep21536%5Cn%3CGo%20to%20ISI%3E://WOS:000370499200001%20http://www.nature.com/articles/srep21536.

[11] G. Wang, C. Robert, A. Suslu, B. Chen, S. Yang, S. Alamdari, I. C. Gerber, T. Amand, X. Marie, S. Tongay, and B. Urbaszek, "Spin-orbit engineering in transition metal dichalcogenide alloy monolayers," *Nature Communications*, vol. 6, p. 10 110, Dec. 2015, ISSN: 2041-1723. DOI: 10.1038/ncomms10110. arXiv: 1506.08114. [Online]. Available: http://arxiv.org/abs/1506.08114%20http://www.nature.com/doifinder/10.1038/ncomms10110.

[12] K. Gołasa, M. Grzeszczyk, P. Leszczyński, C. Faugeras, A. A. L. Nicolet, A. Wysmołek, M. Potemski, and A. Babiński, "Multiphonon resonant Raman scattering in MoS_2," *Applied Physics Letters*, vol. 104, no. 9, p. 092 106, Mar. 2014, ISSN: 0003-6951. DOI: 10.1063/1.4867502. [Online]. Available: http://aip.scitation.org/doi/10.1063/1.4867502.

[13] Y. Zhao, X. Luo, H. Li, J. Zhang, P. T. Araujo, C. K. Gan, J. Wu, H. Zhang, S. Y. Quek, M. S. Dresselhaus, and Q. Xiong, "Interlayer breathing and shear modes in few-trilayer MoS_2 and WSe_2.," *Nano letters*, vol. 13, no. 3, pp. 1007–15, Mar. 2013, ISSN: 1530-6992. DOI: 10.1021/nl304169w. [Online]. Available: http://www.ncbi.nlm.nih.gov/pubmed/23432683.

[14] X. Zhang, W. P. Han, J. B. Wu, S. Milana, Y. Lu, Q. Q. Li, A. C. Ferrari, and P. H. Tan, "Raman spectroscopy of shear and layer breathing modes in multilayer MoS_2," *Physical Review B*, vol. 87, no. 11, p. 115 413, Mar. 2013, ISSN: 1098-0121. DOI: 10.1103/PhysRevB.87.115413. [Online]. Available: http://link.aps.org/doi/10.1103/PhysRevB.87.115413%20https://link.aps.org/doi/10.1103/PhysRevB.87.115413.

[15] Q. Feng, N. Mao, J. Wu, H. Xu, C. Wang, J. Zhang, and L. Xie, "Growth of $MoS_{2(1-x)}Se_{2x}$ (x=0.41-1.00) Monolayer Alloys with Controlled Morphology by Physical Vapor Deposition," *ACS Nano*, vol. 9, no. 7, pp. 7450–7455, 2015, ISSN: 1936-0851. DOI: 10.1021/acsnano.5b02506.

[16] Y. Chen, D. O. Dumcenco, Y. Zhu, X. Zhang, N. Mao, Q. Feng, M. Zhang, J. Zhang, P.-H. Tan, Y.-S. Huang, and L. Xie, "Composition-dependent Raman modes of $Mo_{(1-x)}W_xS_2$ monolayer alloys," *Nanoscale*, vol. 6, no. 5, p. 2833, 2014, ISSN: 2040-3364. DOI: 10.1039/c3nr05630a. [Online]. Available: http://www.ncbi.nlm.nih.gov/pubmed/24469100%5Cnhttp://xlink.rsc.org/?DOI=c3nr05630a.

[17] A. Molina-Sánchez and L. Wirtz, "Phonons in single-layer and few-layer MoS_2 and WS_2," *Physical Review B*, vol. 84, no. 15, p. 155 413, Oct. 2011, ISSN: 1098-0121. DOI: 10.1103/PhysRevB.84.155413. arXiv: 1109.5499. [Online]. Available: https://link.aps.org/doi/10.1103/PhysRevB.84.155413.

[18] P. A. Young, "Lattice parameter measurements on molybdenum disulphide," *Journal of Physics D: Applied Physics*, vol. 1, no. 7, p. 416, Jul. 1968, ISSN: 00223727. DOI: 10.1088/0022-3727/1/7/416. [Online]. Available: http://stacks.iop.org/0022-3727/1/i=7/a=416?key=crossref.b36c68e5065dbbd7bc4f714aa625b3ab.

[19] W. Schutte, J. De Boer, and F. Jellinek, "Crystal structures of tungsten disulfide and diselenide," *Journal of Solid State Chemistry*, vol. 70, no. 2, pp. 207–209, Oct. 1987, ISSN: 00224596. DOI: 10.1016/0022-4596(87)90057-0. [Online]. Available: http://linkinghub.elsevier.com/retrieve/pii/0022459687900570.

[20] B. Amin, T. P. Kaloni, and U. Schwingenschlögl, "Strain engineering of WS_2 , WSe_2, and WTe_2," *RSC Advances*, vol. 4, no. 65, p. 34 561, Aug. 2014, ISSN: 2046-2069. DOI: 10.1039/C4RA06378C. [Online]. Available: http://xlink.rsc.org/?DOI=C4RA06378C.

[21] E. Scalise, M. Houssa, G. Pourtois, V. Afanaseev, and A. Stesmans, "First-principles study of strained 2D MoS_2," *Physica E: Low-dimensional Systems and Nanostructures*, vol. 56, pp. 416–421, Feb. 2014, ISSN: 13869477. DOI: 10.1016/j.physe.2012.07.029. [Online]. Available: http://linkinghub.elsevier.com/retrieve/pii/S1386947712003062.

[22] H. Zeng, B. Zhu, K. Liu, J. Fan, X. Cui, and Q. M. Zhang, "Low-frequency Raman modes and electronic excitations in atomically thin MoS_2 films," *Physical Review B - Condensed Matter and Materials Physics*, vol. 86, no. 24, 2012, ISSN: 10980121. DOI: 10.1103/PhysRevB.86.241301. arXiv: arXiv:1209.1775v1.

[23] J.-U. Lee, J. Park, Y.-W. Son, and H. Cheong, "Anomalous excitonic resonance Raman effects in few-layered MoS_2," *Nanoscale*, vol. 7, no. 7, pp. 3229–3236, 2015, ISSN: 2040-3364. DOI: 10.1039/C4NR05785F. [Online]. Available: http://xlink.rsc.org/?DOI=C4NR05785F.

[24] Z. Ye, T. Cao, K. O'Brien, H. Zhu, X. Yin, Y. Wang, S. G. Louie, and X. Zhang, "Probing Excitonic Dark States in Single-layer Tungsten Disulfide," *Nature*, vol. 513, no. 7517, pp. 214–218, 2014, ISSN: 0028-0836. DOI: 10.1038/nature13734. arXiv: 1403.5568.

[25] R. M. Martin and T. Damen, "Breakdown of Selection Rules in Resonance Raman Scattering," *Phys. Rev. Lett.*, vol. 26, no. 2, pp. 86–88, 1971, ISSN: 0031-9007. DOI: 10.1103/PhysRevLett.26.86.

[26] J.-U. Lee, K. Kim, S. Han, G. H. Ryu, Z. Lee, and H. Cheong, "Raman Signatures of Polytypism in Molybdenum Disulfide," *ACS Nano*, vol. 10, no. 2, pp. 1948–1953, Feb. 2016, ISSN: 1936-0851. DOI: 10.1021/acsnano.5b05831. [Online]. Available: http://dx.doi.org/10.1021/acsnano.5b05831%20http://pubs.acs.org/doi/10.1021/acsnano.5b05831.

[27] J. Yang, J.-U. Lee, and H. Cheong, "Excitation energy dependence of Raman spectra of few-layer WS_2," *FlatChem*, vol. 3, pp. 64–70, Jun. 2017, ISSN: 24522627. DOI: 10.1016/j.flatc.2017.06.001. [Online]. Available: http://dx.doi.org/10.1016/j.flatc.2017.06.001%20http://linkinghub.elsevier.com/retrieve/pii/S2452262717300624.

[28] K. Kosmider and J. Fernández-Rossier, "Electronic properties of the MoS_2-WS_2 heterojunction," *Physical Review B - Condensed Matter and Materials Physics*, vol. 87, no. 7, pp. 2–5, 2013, ISSN: 10980121. DOI: 10.1103/PhysRevB.87.075451. arXiv: 1212.0111.

[29] K. Kosmider, J. W. González, and J. Fernández-Rossier, "Large spin splitting in the conduction band of transition metal dichalcogenide monolayers," *Physical Review B - Condensed Matter and Materials Physics*, vol. 88, no. 24, pp. 1–7, 2013, ISSN: 10980121. DOI: 10.1103/PhysRevB.88.245436. arXiv: 1311.0049.

[30] A. Kormányos, V. Zólyomi, N. D. Drummond, and G. Burkard, "Spin-orbit coupling, quantum dots, and qubits in monolayer transition metal dichalcogenides," *Physical Review X*, vol. 4, no. 1, pp. 1–16, 2014, ISSN: 21603308. DOI: 10.1103/PhysRevX.4.011034. arXiv: 1310.7720.

[31] S. Kim, K. Kim, J.-U. Lee, and H. Cheong, "Excitonic resonance effects and Davydov splitting in circularly polarized Raman spectra of few-layer WSe_2," *2D Materials*, vol. 4, no. 4, p. 045 002, Aug. 2017, ISSN: 2053-1583. DOI: 10.1088/2053-1583/aa8312. arXiv: 1612.05879. [Online]. Available: https://arxiv.org/ftp/arxiv/papers/1708/1708.00126.pdf%20http://stacks.iop.org/2053-1583/4/i=4/a=045002?key=crossref.081d6ef1060602b8c7c7aa9c344b2858.

[32] M. O'Brien, N. McEvoy, D. Hanlon, K. Lee, R. Gatensby, J. N. Coleman, and G. S. Duesberg, "Low wavenumber Raman spectroscopy of highly crystalline $MoSe_2$ grown by chemical vapor deposition," *physica status solidi (b)*, vol. 252, no. 11, pp. 2385–2389, Nov. 2015, ISSN: 03701972. DOI: 10.1002/pssb.201552225. arXiv: 1505.02260. [Online]. Available: http://doi.wiley.com/10.1002/pssb.201570369%20http://doi.wiley.com/10.1002/pssb.201552225.

[33] Q.-H. Tan, Y.-J. Sun, X.-L. Liu, Y. Zhao, Q. Xiong, P.-H. Tan, and J. Zhang, "Observation of forbidden phonons and dark excitons by resonance Raman scattering in few-layer WS_2," *2D Materials*, vol. 4, p. 1704.01315, 2017. DOI: https://doi.org/10.1088/2053-1583/aa79bb. arXiv: arXiv:1704.01315v1. [Online]. Available: https://arxiv.org/pdf/1704.01315.pdf.

[34] C. Cheng, J.-T. Sun, X.-R. Chen, H.-X. Fu, S. Meng, Y. Iwasa, E. Saitoh, D. Barroso, S. Kim, V. Y. Shur, A. R. Akhmatkhanov, A. Gruverman, L. Bartels, P. A. Dowben, R. Arita, N. Nagaosa, K. Kobayashi, Y. Murakami, R. Kumai, Y. Kaneko, Y. Onose, and Y. Tokura, "Nonlinear Rashba spin splitting in transition metal dichalcogenide monolayers," *Nanoscale*, vol. 8, no. 41, pp. 17 854–17 860, 2016, ISSN: 2040-3364. DOI: 10.1039/C6NR04235J. [Online]. Available: http://xlink.rsc.org/?DOI=C6NR04235J.

[35] M. A. U. Absor, I. Santoso, Harsojo, K. Abraha, H. Kotaka, F. Ishii, and M. Saito, "Polarity tuning of spin-orbit-induced spin splitting in two-dimensional transition metal dichalcogenides," *Journal of Applied Physics*, vol. 122, no. 15, p. 153 905, Oct. 2017, ISSN: 0021-8979. DOI: 10.1063/1.5008475. arXiv: 1702.06685. [Online]. Available: http://arxiv.org/abs/1702.06685%20http://dx.doi.org/10.1063/1.5008475%20http://aip.scitation.org/doi/10.1063/1.5008475.

[36] H. Dery and Y. Song, "Polarization analysis of excitons in monolayer and bilayer transition-metal dichalcogenides," *Physical Review B*, vol. 92, no. 12, p. 125 431, Sep. 2015, ISSN: 1098-0121. DOI: 10.1103/PhysRevB.92.125431. arXiv: 1506.06686. [Online]. Available: http://arxiv.org/abs/1506.06686%20https://link.aps.org/doi/10.1103/PhysRevB.92.125431.

[37] T. Y. Jeong, B. M. Jin, S. H. Rhim, L. Debbichi, J. Park, Y. D. Jang, H. R. Lee, D.-H. Chae, D. Lee, Y.-H. Kim, S. Jung, and K. J. Yee, "Coherent Lattice Vibrations in Mono- and Few-Layer WSe_2," *ACS Nano*, vol. 10, no. 5, pp. 5560–5566, May 2016, ISSN: 1936-0851. DOI: 10.1021/acsnano.6b02253. [Online]. Available: http://pubs.acs.org/doi/abs/10.1021/acsnano.6b02253%20http://pubs.acs.org/doi/10.1021/acsnano.6b02253.

[38] A. J. McKenna, "Photo-induced Structural Dynamics of Molybdenum Disulfide," PhD thesis, University of Minnesota, 2017.

[39] J.-W. Jiang, B.-S. Wang, J.-S. Wang, and H. S. Park, "A review on the flexural mode of graphene: lattice dynamics, thermal conduction, thermal expansion, elasticity and nanomechanical resonance," *Journal of Physics: Condensed Matter*, vol. 27, no. 8, p. 083 001, Mar. 2015, ISSN: 0953-8984. DOI: 10.1088/0953-8984/27/8/083001. arXiv: 1408.1450. [Online]. Available: http://arxiv.org/abs/1408.1450%0Ahttp://dx.doi.org/10.1088/0953-8984/27/8/083001%20http://stacks.iop.org/0953-8984/27/i=8/a=083001?key=crossref.6f1600b267f607eb2eb1a457e7730613.

[40] H. Lamb, "On Waves in an Elastic Plate," *Proceedings of the Royal Society A: Mathematical, Physical and Engineering Sciences*, vol. 93, no. 648, pp. 114–128, Mar. 1917, ISSN: 1364-5021. DOI: 10.1098/rspa.1917.0008. [Online]. Available: http://rspa.royalsocietypublishing.org/cgi/doi/10.1098/rspa.1917.0008.

[41] R. Yoshizaki, K. Uchinokura, T. Nakashizu, and E. Matsuura, "Dispersive Raman Mode of Layered Compound 2H-MoS_2 under the Resonant Condition," *Journal of the Physical*

Society of Japan, vol. 53, no. 2, pp. 811–818, 1984, ISSN: 13474073. DOI: 10.1143/JPSJ.53.811.

Chapter 5

Raman Studies of Indium Selenide

5.1 Introduction

The nature of chemical bonding in indium–selenium compounds is such that a wide range of stoichometries and crystal structures may be metastable in ambient conditions [1], and thus manifest a greater diversity than their transition metal dichalcogen counterparts. The indium–selenium phase diagram demonstrates the range of compounds that may be produced from the binary elements.

This diversity in the structures of InSe is probed accurately by the technique of Raman spectroscopy and, as such, this chapter aims to describe InSe compounds isolated by novel means.

The samples investigated in this work have been produced by the following methods:

- Mechanical exfoliation by the use of viscoelastic PDMS (Poly-(dimethylsiloxane)) dry stamping method, produced in The department of Physics and Astronomy, at The University of Sheffield by Messrs Allesandro Catanzaro and Daniel Gillard. These samples represent the most simple isolation of InSe on clean, well understood substrates of 290 nm SiO_2 on Si. Post fabrication, samples were immediately stored under vacuum to preserve the flake integrity, and transferred directly to the cryostat before measurements were taken.
- Hexagonal Boron Nitride pickup and encapsulation in an argon atmosphere glovebox with the goal of producing ultra clean, environmentally stable devices [2]. Surface passivation is an important technique in controlling the interaction of any material with its environment: in 2D materials the dielectric environment and surface roughness of an interface has important consequences for the stability and properties of the fabricated sample [3]. Hexagonal boron nitride with its high dielectric constant and atomically smooth layers provides the leading means of engineering high quality vdW heterostructures. It is with the goal of high environmental stability that these InSe flakes were produced at the School

of Physics and Astronomy and The University of Manchester by Mr. Matthew Hamer.
- In_2Se_3 grown on exfoliated GaSe flakes, by Dr. Nilanthy Balakrishnan at the School of Physics and Astronomy, The University of Nottingham, in a physical vapour transport process described in reference [4]. The process targeted the formation of GaSe/InSe heterojuctions for the exploration of a scalable method of producing room temperature elecroluminecent devices with a wide band optical response [5].

Samples such as these have never previously been studied using the technique of ultra low frequency Raman spectroscopy.

5.1.1 InSe Structures

InSe may crystallise into one of two structures, akin to the polymorphs of TMD's octahedral or trigonal prismatic arrangements, with Se-In-In-Se lattice arrangements of *AbbC*, and *AbbA*, respectively. The trigonal prismatic *AbbA* structure is the more stable [6], and from this are built up the polytypes, β, ε, δ, and γ, often referred to as phases in the literature.

The stacking orders of these polytypes are understood as:

- Rhombohedral with 3 layers in unit cell, centrosymmetric γ-polytype; ABC stacking.
- Hexagonal with 2 layers in the unit cell; β-, centrosymmetric (AA′A), and ε-, non-centrosymmetric (ABA).
- Hexagonal with 4 layers in the unit cell; δ-, non-centrosymmetric (ABACA) [7].
- 9R, & 12R polytypes are also reported [8].

It has been demonstrated that these phases can exist stacked vertically on top of one another [9]. Presently there exists no precise method for characterising the stacking orders in InSe via optical spectroscopy, thus the technique of ultra low frequency Raman spectroscopy offers much in this regard.

5.1.2 In_2Se_3 Structures

Recent interest has been generated in this indium-selenide compound due to its suitability as a candidate for phase-change random access memory (PRAM) applications, due to the various metastable states it manifests [10], [11].

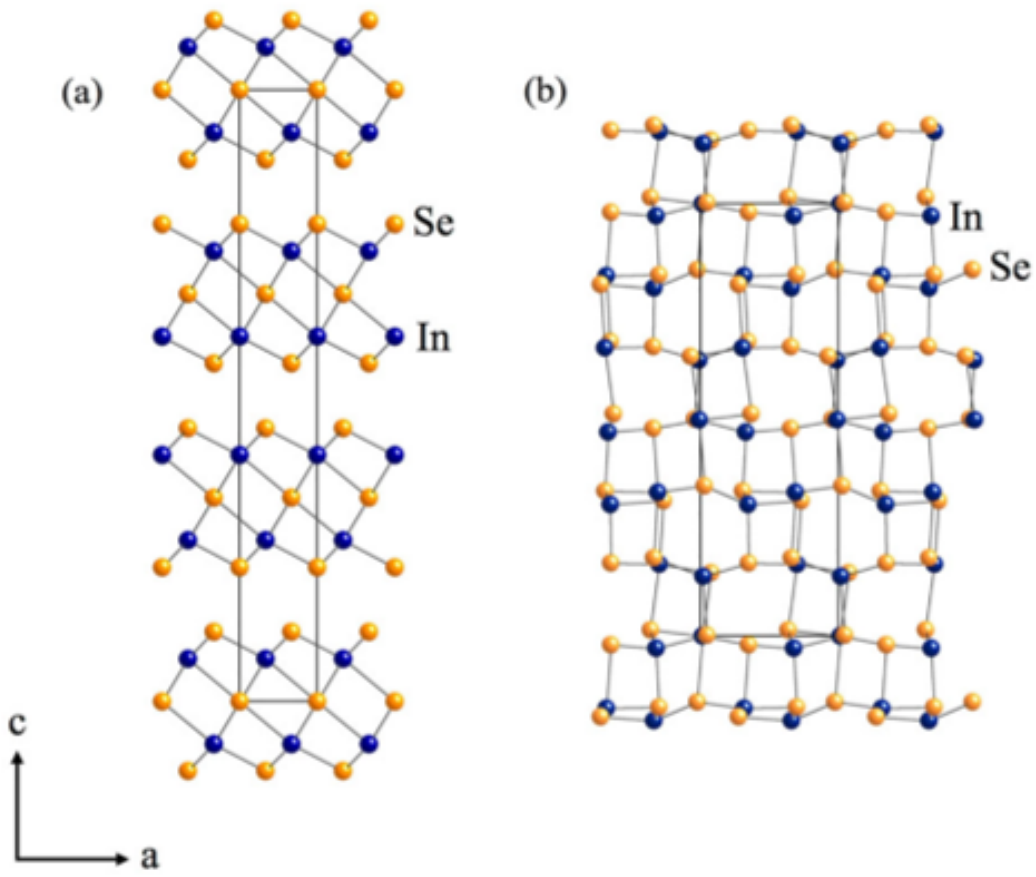

Figure 5.1: Di-indium triselenide ball-and-stick models for: (a) layered α, β-phases, in this instance, 3R polytype-β-phase; and (b), non-layered defect wurtzite (γ -phase). Figure from reference [12].

In_2Se_3 may be preferable over other prospective materials such as $Ge_2Sb_2Te_5$ as a potential PRAM material due to its high resistivity and the large change in resistivity between a crystalline and possibly amorphous phase, as reported in a nanowire structure [11]. In addition, the crystalline-crystalline phase transitions of In_2Se_3 holds prospects for multi-level memory.

For indium–selenium compounds there exists considerable complexity in obtaining desired stoichiometry and phase from growth precursors. In the specific case of In_2Se_3 the following phase relationships are currently accepted, with some variation on the exact temperatures [13], [14]:

$$\alpha \underset{\leftarrow}{\xrightarrow{T\approx 200^{\circ}C}} \beta \underset{\leftarrow}{\xrightarrow{(350\leqslant T\leqslant 520)^{\circ}C}} \gamma \underset{\leftarrow}{\xrightarrow{(550\leqslant T\leqslant 730)^{\circ}C}} \delta \tag{5.1}$$

The two principal cryistal structures for In_2Se_3 are depicted in figure 5.1; they are defined by the nature of the vacancy sites, with the layered structures having planar vacancy defects, whilst the γ-phase exhibits a screw pattern on every third indium site [15], [16].

The nature of the exact positioning of indium and selenium atoms in the various In_2Se_3 phases has long been an issue of contention, [13], [15]–[21]. Figure 5.2 illustrates various suggested In_2Se_3 layer structures, clarification has recently been provided where first-principles DFT calculations were compared with experimentally measured lattice constants and the ground states were identified to be the α-phase, while the fcc′ state to be the β-phase [22]. The calculated phonon spectra agreed with the modes in the case of fcc′ β-phase, but discrepancy is noted for the A_1 Raman mode of the FE-ZB′ and FE-WZ′ α-phase and those experimentally determined, although the A_1 mode blue-shift between β- & α- phases was present.

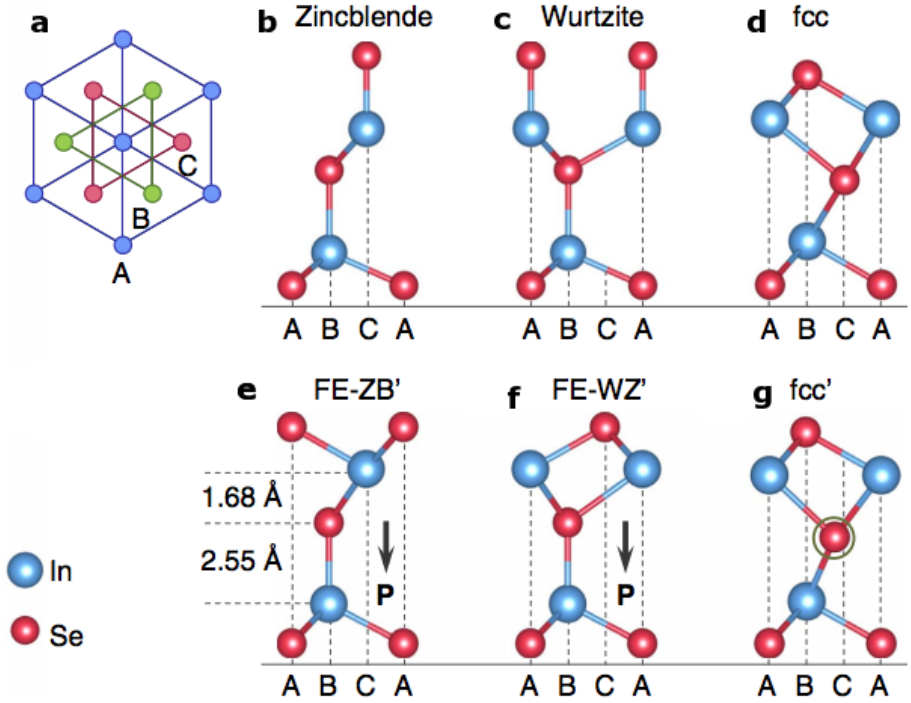

Figure 5.2: Ball-and-stick models of representative structures of In_2Se_3 molecular-layers with Indium atoms in blue and selenium atoms in red. (a) Plan view of the system; each atomic layer in a molecular-layer contains a single elemental species, with the atoms arranged in one of the triangular lattices A, B, or C as shown. (b–g) Cross sectional views of several representative structures of one monolayer In_2Se_3, among which the (b–d) structures are derived from the zincblende, wurtzite, and fcc crystals, respectively. In e, the central Se layer and the two neighbouring In layers are displaced. The black arrows in e & f indicate the directions of the spontaneous electric polarization, P, in the ferroelectric-ZB′ and ferroelectric-WZ′ structures. Figure from reference [22]

Phase changes of In_2Se_2 have been demonstrated by various means:

- By pressure:
  - $\alpha \rightarrow \beta$ at critical pressures P_c of 0.7 GPa, an order of magnitude lower than phase-transition of typical semiconductors [23], [24].
  - $\gamma \rightarrow \beta$ $(2.8 \leqslant P_c \leqslant 3.2)$ GPa in bulk powder samples and slightly higher pressures of $(3.2 \leqslant P_c \leqslant 3.7)$ GPa in nanowire samples [12].

- Thermal annealing resulting in partial transition ε-InSe $\rightarrow$ γ-In_2Se_3 [25].
- Laser photo-annealing. $\gamma \rightarrow \alpha$-$In_2Se_3$ [26].
- Electrically, between unconfirmed phases, with set/reset powers and energies orders of magnitude below competing material systems; GeTe or $Ge_2Sb_2Te_5$ nanowires [11], [27].

5.2 Results

Presented here are the results of Raman studies carried out with 532 nm laser excitation, with samples at room temperature under vacuum, in the system described in section 3.1.1.

5.2.1 PDMS Exfoliated InSe

Full-range spectra for PDMS exfoliated InSe, normalised in the acquisition time are presented in figure 5.3, in both co- and cross-polarised configurations. A^1_{1g} modes around 114 cm^{-1} are seen to redshift with decreasing layer number, additionally their FWHM increase from (2.5±0.1) cm^{-1} in bulk to (3.1±0.1) cm^{-1} in the trilayer, and (3.9±0.1) cm^{-1} in bilayer.

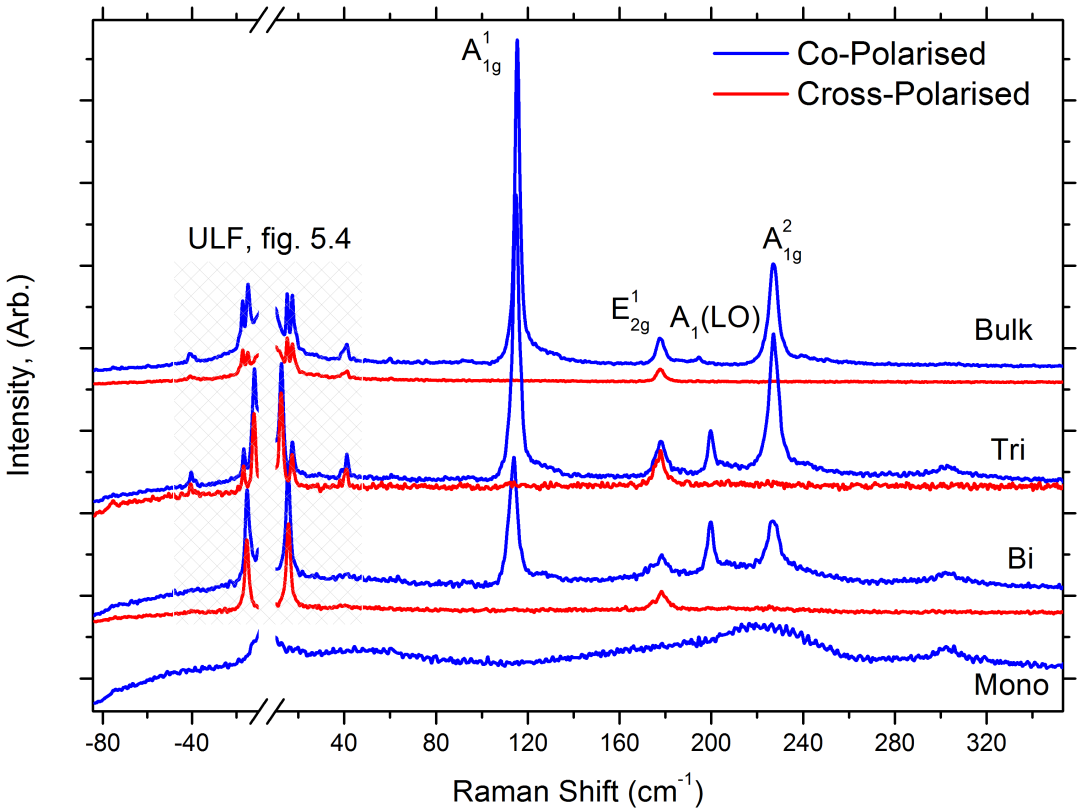

Figure 5.3: Polarisation resolved full-range Raman spectra of various thicknesses of PDMS exfoliated InSe. Normalised in their acquisition times. The peak frequencies are listed in table 5.2

InSe							
ε-phase, †		γ-phase, ‡		β-phase, ♠		PDMS Exfoliated	Epitaxially Grown
Assigned	ν	Assigned	ν	Assigned	ν	ν	ν
-	-	-	-	E	-	15.1	-
E'	17 (calc.)	-	-	E^2_{2g}	17	17.2	-
E''	42	E	48	E^1_{1g}	40	41.3	41
A'_1	117	A	118	A^1_{1g}	115	115.4	114.3
				A	-	-	148.0
E''	177	E	180	E^1_{2g}	176	177.5	175.4
E'(TO)	199	-	-	A_1 (LO)	190	194.4	197
E' (LO)	212	-	214	-	-	-	-
A'_1	226	A	228	A^2_{1g}	225	227	224.7

Frequencies in cm^{-1}. † reference [28]; λ_{exc}: 514.5 nm. ‡ reference [29], [30],λ_{exc}: 632.8 nm, 1064.4 nm. ♠ references [31]–[33].

Table 5.1: A comparison of previously observed Raman modes for the bulk InSe polytypes ε, γ, & β and those reported in this work in figures 5.3 & 5.7.

The A_1(LO) mode at 199.5 cm^{-1} in the bilayer persists at the same frequency in trilayer - albeit with reduced relative intensity - before the mode shifts to 194.6 cm^{-1} in bulk, with an intensity observable only slightly above the noise floor. A peak not attributable to a specific crystalline vibrational mode can be observed at 302.7 cm^{-1} in the monolayer, is also present in bi- and trilayer flakes, before disappearing in the bulk. The monolayer spectrum manifests only broad features, not attributable to any specific crystalline mode. These broad features in the monolayer might be expected to be oxide signatures, but there is no agreement with the Raman studies of InSe cyrstals oxidised in air [34], and the samples were held under a vacuum of 10^{-6} mbar. The other HF modes show negligible frequency shifts with changes in layer number.

Raman spectra for the ultra low frequency modes of PDMS exfoliated flakes are presented in figure 5.4. The monolayer spectrum is absent of any features. All Raman modes in this region, (< 45 cm^{-1}) appear both in co- and cross-polarisations and are thus E symmetric. The E^1_{1g} mode is absent in monolayer and bilayer flakes, but appears at 40.9 cm^{-1} and 41.1 cm^{-1} in trilayer and bulk, respectively. This mode also appears broader than the equivalent mode in GaSe (figure 5.12), and InSe-like growth on GaSe (figure **??**), this may be due to the presence of a low frequency shoulder. This feature can be observed in detail in figure 5.5, where the lower frequency shoulder has been fitted with a Lorentz peak.

The modes below 20 cm^{-1}, have E symmetry and are attributable to rigid-layer shear modes; the bilayer exhibits only a single peak at 15.5 cm^{-1} whilst additional modes are observed in thicker samples at 12.3 cm^{-1} in trilayer, & 15.1 cm^{-1} in bulk, with the higher frequency modes

at 17.0 cm^{-1} & 17.2 cm^{-1} in trilayer and bulk, respectively.

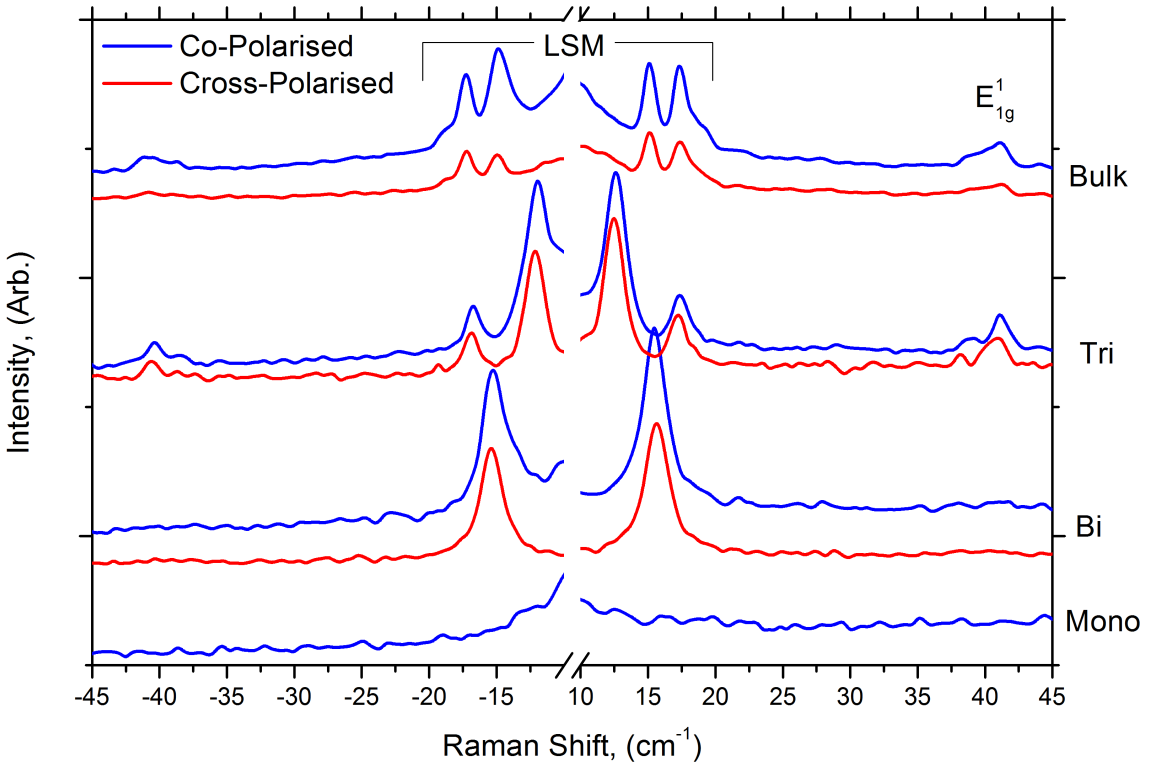

Figure 5.4: Polarisation resolved ultra-low-frequency Raman spectra of various thicknesses of PDMS exfoliated InSe.

PDMS Exfoliated; thickness, # molecular layers					hBN Encapsulated; thickness, nm			
As-signed	Mono	Bi	Tri	Bulk	3.5	4	15	30
E'	-	15.5	12.3, 17.0	15.1, 17.2	15.8	10.1	-	11.6, 16.4
E''	-	-	40.9	41.1	-	40.5	40.7	41.1
A'_1	-	113.9	114.7	115.4	115.0	115.0	115.0	115.0
E	-	178.0	177.7	177.7	177.7	177.2	177.0	177.1
A_1(LO)	-	199.5	199.5	194.6	199.8	199.9	-	191.9
A	-	227.0	226.9	226.9	227.6	227.5	227.0	227.1
A	302.7	303.0	302.7	-	303.5	303.8	303.6	304.7

Frequencies in cm^{-1}

Table 5.2: A comparison of Raman modes observed in PDMS exfoliated and hBN encapsulated InSe.

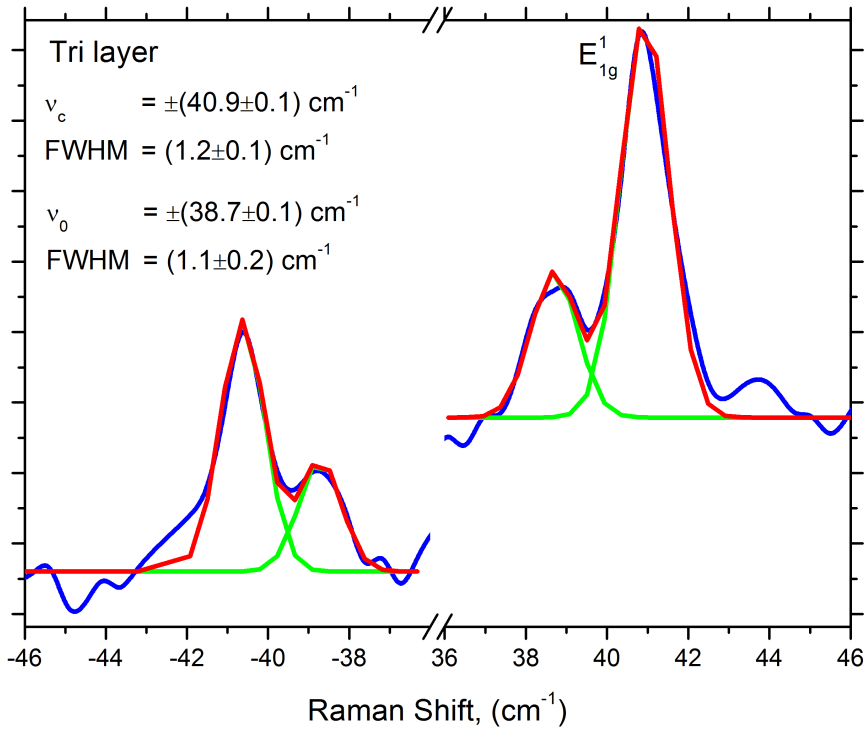

Figure 5.5: Stokes and anti-Stokes peaks of co-polarised trilayer InSe E^1_{1g} mode with two Lorentz peaks fitted to the Davydov components.

A more comprehensive plot of the shear modes of PDMS exfoliated InSe is shown in figure 5.6, where for layer numbers of N, $(N-1)$ layer shear modes are observed. Note that the bulk ULF modes don't correspond between figures 5.4 & 5.6, and can be understood in the discussion. For a selection of 25 flakes of various thickness, the shear modes have been extracted and plotted in figure 5.6 b as a function of layer number, with the branches of a linear chain model (LCM) plotted for comparison, and each experimentally observed branch plotted with a distinct colour for clarity. The linear chain model has been used with success previously to describe interlayer vibrations in 2d materials [35]–[41]. The treatment models the molecular layers as "pseudoatoms", considering only nearest-neighbour interactions, and ignoring substrate coupling. The interlayer mode frequencies of flakes in cm^{-1} of layer number N are given by the following equation:

$$\omega_{SM,LBM} = \sqrt{\frac{K_{SM,LBM}}{2\mu\pi^2c^2}\left\{1-\cos\left[\frac{(\alpha-1)\pi}{N}\right]\right\}} \tag{5.2}$$

where $K_{SM,LBM}$ is the interlayer force constant for a shear, or breathing mode, μ is the square density, c is the speed of light in cm·s^{-1}, and α = 1,2, ..., N is the branch index. $\alpha = 1$ gives the zero frequency acoustic modes; $\alpha = 2$, the lowest frequency branch, with neighbouring molecular layers vibrating with the lowest possible phase difference $\pi/(N-1)$; and $\alpha = N$, the

highest frequency branch with neighbouring layers relatively π out-of-phase.

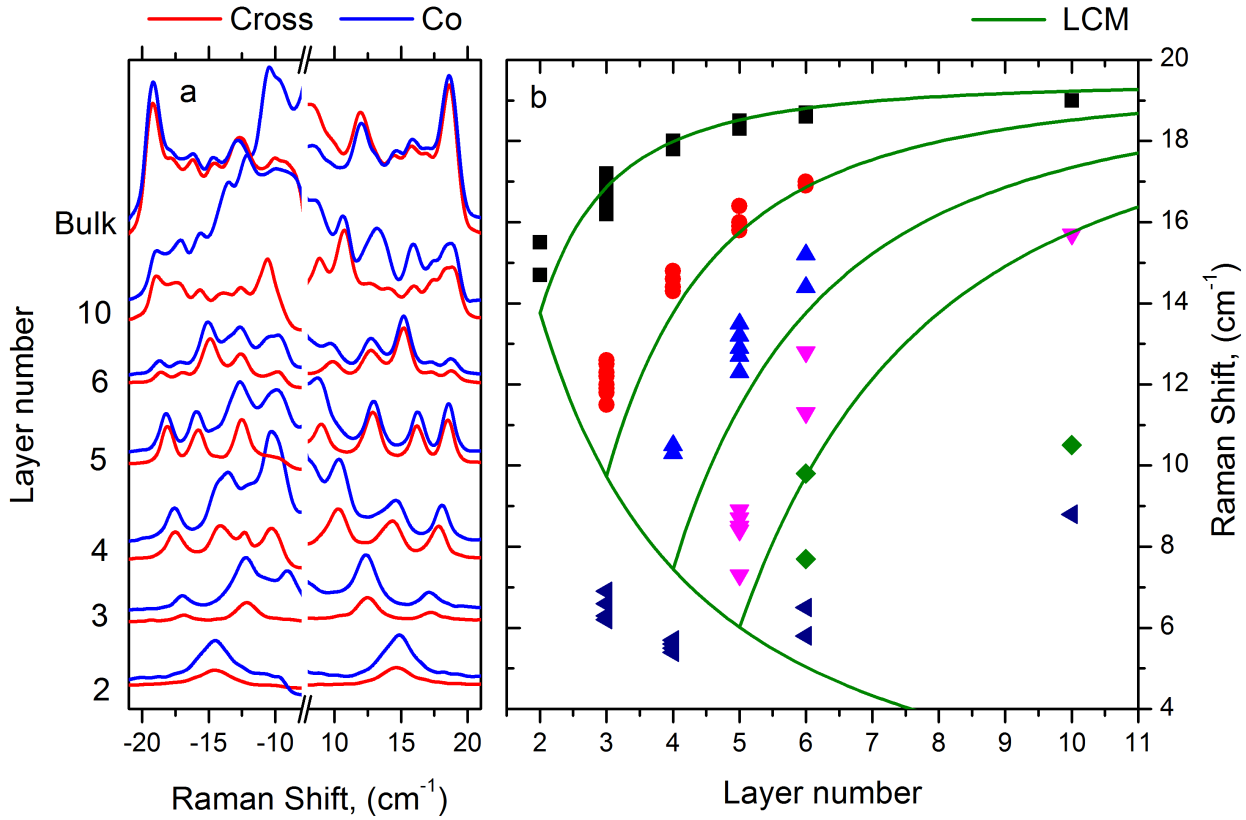

Figure 5.6: (a) Stokes and anti-Stokes shear mode peaks of PDMS InSe multilayers. (b) Extracted peak positions from 25 PDMS multilayers, and superposed linear chain model branch trends.

5.2.2 Hexagonal Boron Nitride Encapsulated InSe

The full-range co-polarised Raman spectrum normalised to the A_{2g} peak at 227 cm^{-1}, for hBN encapsulated samples is shown in figure 5.7. The optical lattice normal modes can be found around 41 cm^{-1} (E^1_{1g}); 115 cm^{-1} (A_{1g}); 177 cm^{-1} (E_{2g}); 227 cm^{-1} (A), frequencies are summarised in table 5.2. The A_{1g}, E_{1g}, and A modes are all observed to remain at a single wavenumber with respect to the thicknesses displaying no systematic trend.

For the A_1(LO) mode a similar behaviour is observed to the PDMS exfoliated samples, where in the 3.5 nm and 4 nm thicknesses the mode appears at 199 cm^{-1}, whilst in the 30 nm flake, this peak appears at 191 cm^{-1}. The broad feature around 303 cm^{-1} shows a reduction in prominence with increasing thickness, but no definite shift, in agreement with the PDMS exfoliated samples.

Below 100 cm^{-1} appear a great number of closely spaced narrow peaks, these are attributable to the rotational modes of air, and appear in both the Stokes and anti-Stokes frequencies at def-

inite frequencies, figure 5.8 shows the co-polaried spectrum of 3.5 nm thick, hBN–encapsulated InSe (blue trace), which has the greatest air:InSe Raman signal, with the Raman spectrum for air (yellow trace), there is direct correspondence between the Rotational modes of N_2 and O_2 and those observed in the encapsulated InSe sample.

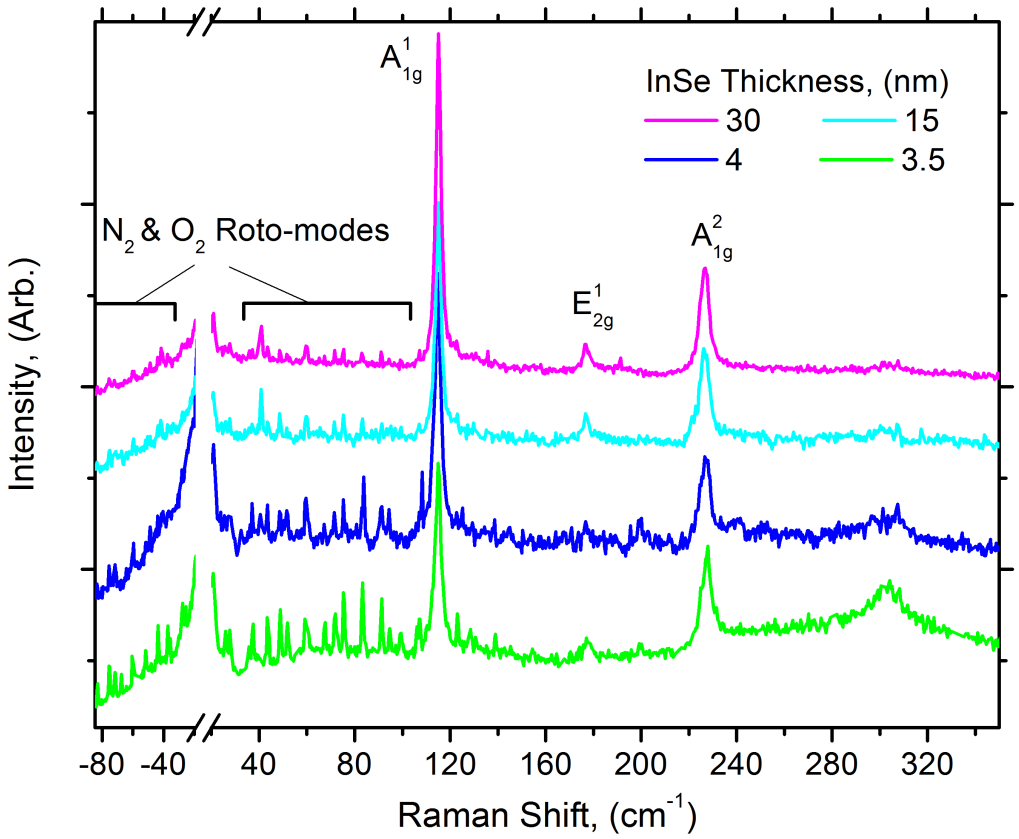

Figure 5.7: Co-polarised full range Raman spectra of four thicknesses of hBN encapsulated InSe.

Cross-polarised ultra low frequency Raman spectra normalised to the remnant of the A_{1g} peak are presented in figure 5.10, low signal:noise and additional Rayleigh scattering require use of the cross-polarised spectra for observation of this region of Raman scattering. The Raman modes of Air are most prominent in the spectrum of the 3.5 nm sample, and these peaks are identifiable in the thicker flakes. Notably the 3.5 nm thickness is absent of the E^1_{1g} mode, whilst the thicker flakes show small frequency shifts with increasing thickness; 40.5 cm^{-1}, 40.7 cm^{-1}, and 41.1 cm^{-1} for the 4 nm , 15 nm, and 30 nm thick flakes. Shear modes are present in 3.5 nm and 4 nm flakes at frequencies of 15.8 cm^{-1} and 10.1 cm^{-1}, respectively. The 15 nm flake is absent of such low frequency modes, and shows greater Rayleigh scattering tails. The 30 nm sample has shear mode peaks at 16.4 cm^{-1}, and 11.6 cm^{-1}.

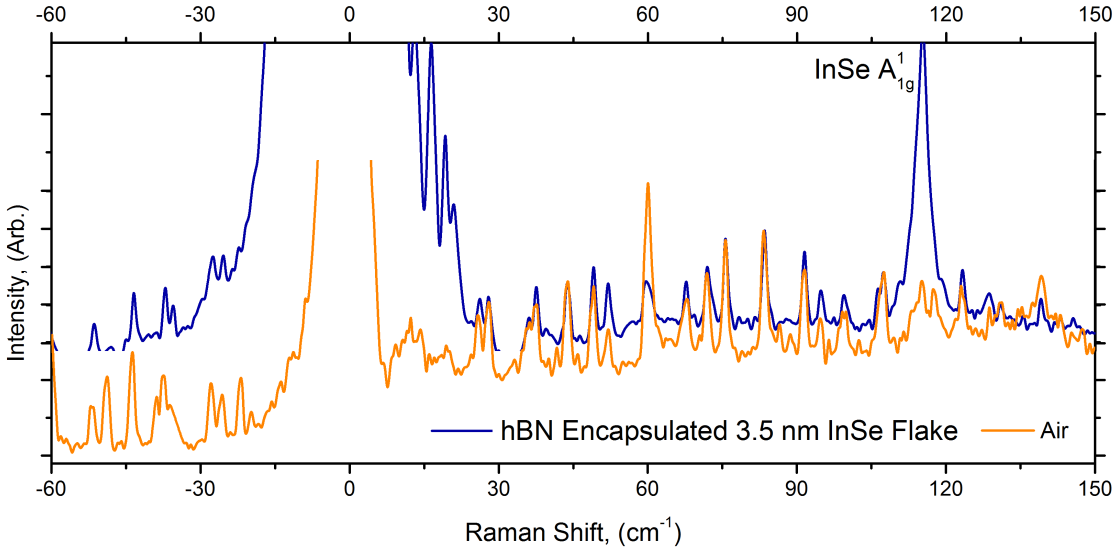

Figure 5.8: Co-polarised Raman spectrum of hBN encapsulated 3.5 nm InSe flake, compared with the Raman response for air.

AFM height images for the hBN-encapsulated InSe flakes may be observed in figure 5.9: numerous bubble-like features are present, with the density of the features being higher on thicker InSe flakes, whilst the 3.5 nm flake displays fewer but larger structures.

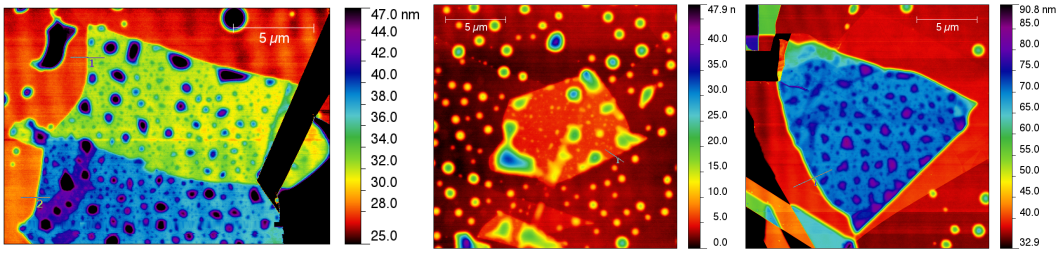

(a) Substrate hBN, 12 nm; InSe 4, & 15 nm; cap hBN 20 nm.

(b) Substrate hBN, 15 nm; InSe 3.5 nm; cap hBN 25 nm.

(c) Substrate hBN, 12 nm; InSe 30 nm; cap hBN 21 nm.

Figure 5.9: AFM height images of Hexagonal boron nitride encapsulated indium selenide flakes. Numerous bubble-like features are present.

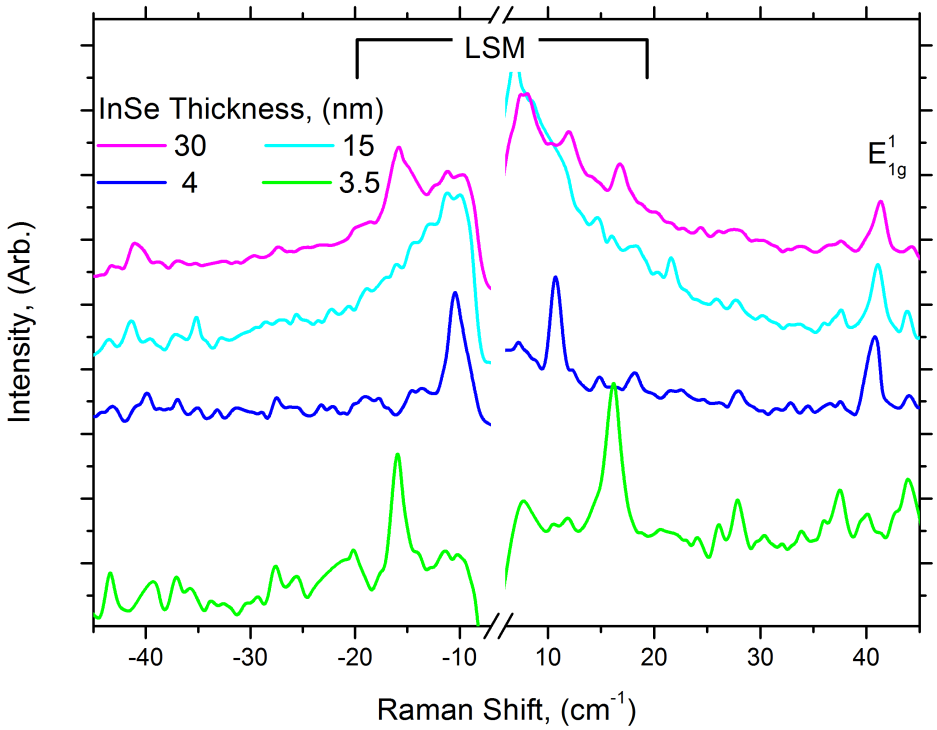

Figure 5.10: Cross-polarised ultra-low-frequency Raman spectra of four thicknesses of hBN encapsulated InSe.

5.2.3 Epitaxially grown In_2Se_3 on GaSe

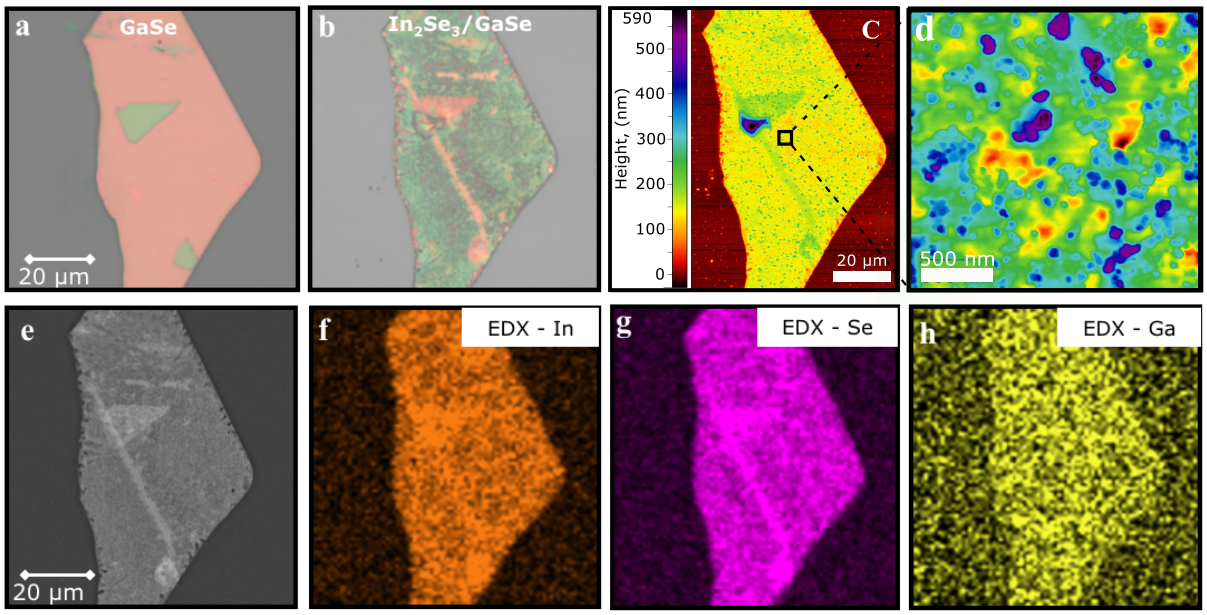

Figure 5.11: Images of the target GaSe flake, (optical micrograph, a) and the resulting GaSe/In_2Se_3 heterostructure (b–h). (b) shows the optical micrograph of the GaSe flake post In_2Se_3 growth, (c) is an AFM height image of the GaSe/In_2Se_3 heterostructure, with panel c, being another smaller area, higher resolution AFM height image. A plain SEM electron image is shown in (e), whilst figures f, g, & h are EDX maps of indium, selenium, and gallium, respectively. Images courtesy of Nilanthy Balakrishnan.

The absence of the 252.1 cm^{-1} (E'') Raman mode in figure 5.12 (see table 5.3) and the lack of correspondence of the E^1_{2g} 213.0 cm^{-1} peak with the β-phase peak (E'(TO)) suggests that the GaSe polytype used here is the β-polytype belonging to the D_{6h} space group, rather than the non-centrosymmetric ε-GaSe, of space group D_{3h}. There remains a missing peak at 249 cm^{-1}, but this peak tends to be very weak in previously reported spectra.

GaSe				
ε-phase, †		β-phase, ♠		Present work
Assignment	ν	Assignment	ν	$\nu^{\star}$
E'	19.5	E^2_{2g}	19.1	18.9
E''	60.1	E^1_{1g}	60.1	60.0
A'_1	134.3	A^1_{1g}	134.6	134.4
E''	211.9	E^2_{1g}	249.0	-
E'(TO)	215.0±2	E^1_{2g}	213.1	213.0
E''	252.1	-	-	-
A'_1	308.0	A^2_{1g}	307.8	307.6

Frequencies in cm^{-1}. † reference [42]; λ_{exc}: 514.5 nm. ♠ reference [43]; λ_{exc}: 514.5 nm. $\star$ Present work; λ_{exc}: 532 nm.

Table 5.3: A comparison of previously observed Raman modes for GaSe and those reported in this work.

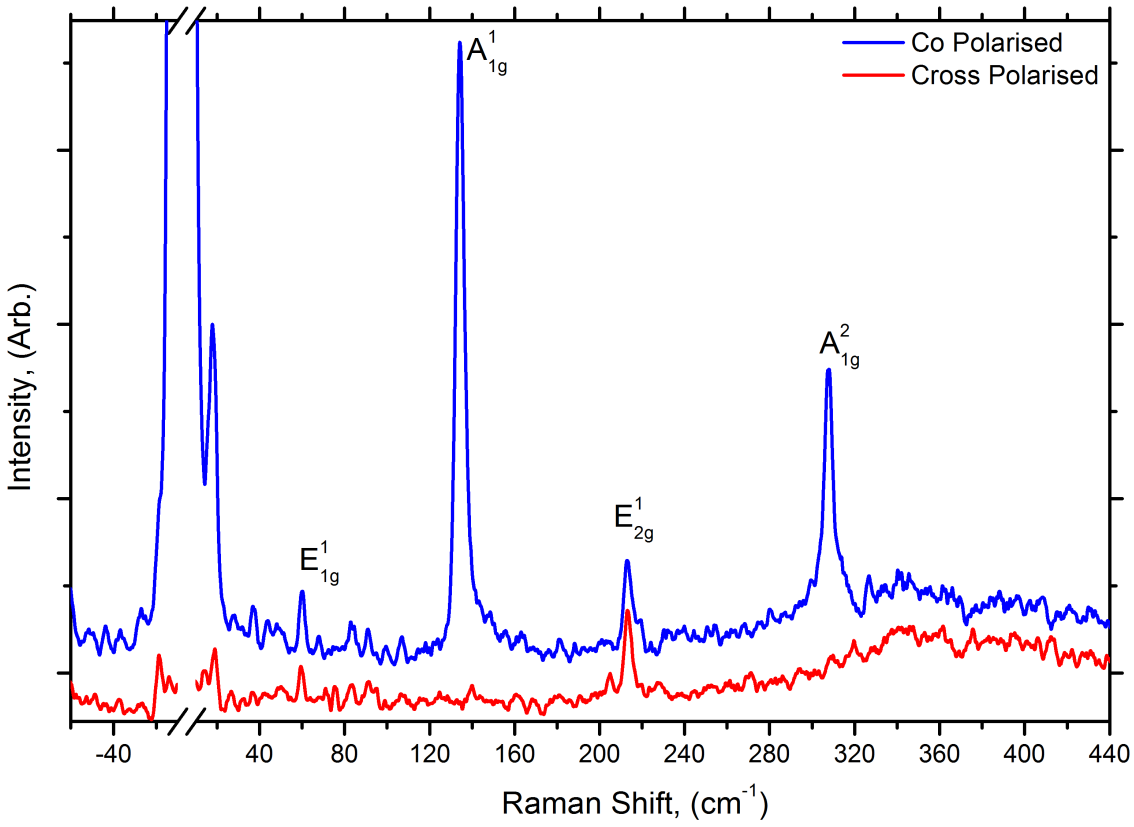

Figure 5.12: Co-, and cross-polarised Raman spectra of an exfoliated GaSe flake of comparable thickness to the epitaxial substrate flake in 5.11.

Figures 5.13–?? show the various Raman spectra collected from different regions of the epitaxially grown In_xSe_y.

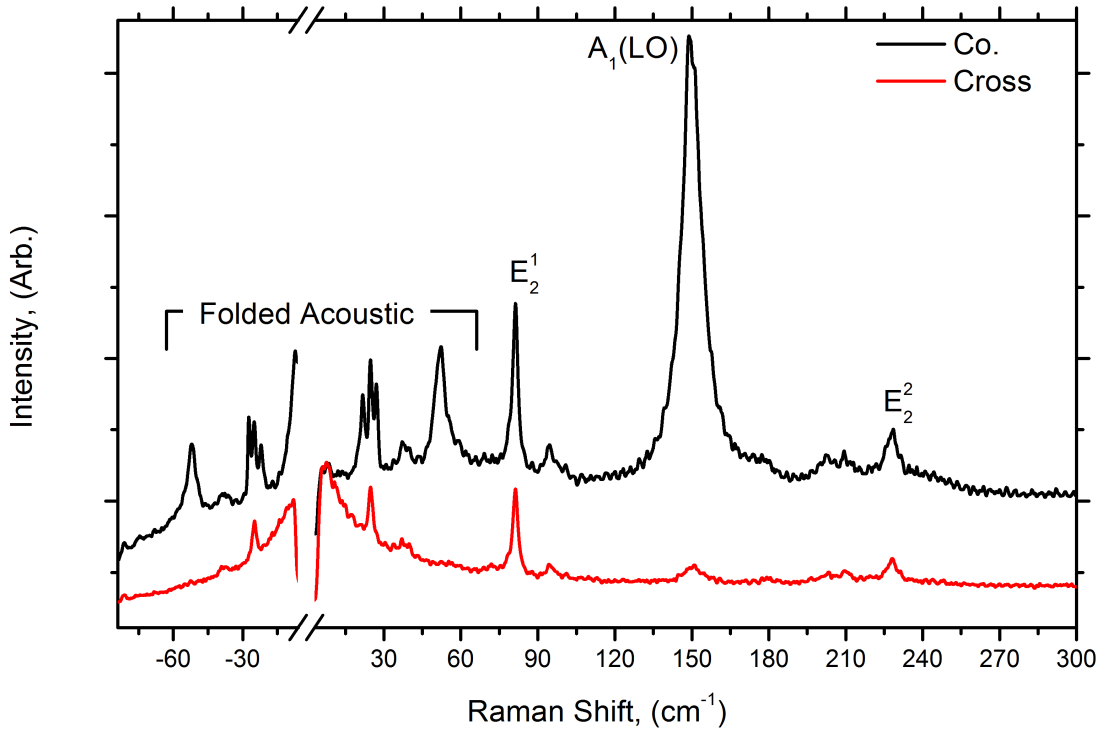

Figure 5.13: Co-, and cross-polarised Raman spectra of a region of γ-In_2Se_3 which grows preferentially at the GaSe flake discontinuities, as seen by the resulting red contrast areas in the 5.11 b In_2Se_3/GaSe optical micrograph.

The figure 5.13 shows a spectrum, recorded in co- $(z(xx)\bar{z})$, and cross-$(z(xy)\bar{z})$ polarisations, the Raman peak positions correspond closely to those previously observed for γ-In_2Se_3 [20], [44], as presented in table 5.4. These spectra were collected from regions of GaSe flake discontinuities, as seen by the resulting red contrast areas in the 5.11b In_2Se_3/GaSe optical micrograph. The γ-In_2Se_3 modes have not been definitively assigned symmetry due to few Raman studies having been carried out to date, and none with any polarisation sensitivity. The wurtzite crystal structure belongs to the space group C_{6v}^4 with its elementary unit cell consisting of four atoms resulting in 12 phonon modes of which 9 are optically active. According to group theory, the optical phonon modes should belong to the irreducible representation $\Gamma_0 = A_1 + 2B_1 + E_1 + 2E_2$.

The figure ?? shows spectra obtained from multiple 600″ CCD exposures from the grown on the continuous planes of the exfoliated GaSe crystal with 0.5 mW laser power at room temperature, and under vacuum. With increasing exposure time the A mode at 110 cm^{-1}

redshifts to 105 cm^{-1}, whilst the two modes at 183 & 204 cm^{-1} grow slightly in intensity. No agreement is made with the reported Raman spectra for rhombohedral and trigonal phases of S_6 molecules [45].

In_2Se_3

α			β			γ		
Assigned	$\nu^{\ddagger}$	$\nu^{\star}$	Assigned	$\nu^{\clubsuit}$	$\nu^{\star}$	Assigned	$\nu^{\diamondsuit}$	$\nu^{\star}$
E	27	-	E	-	27	FA$^{\blacktriangledown}$	22, 26, 40, 54, & 74	21.8, 24.5 ($\perp$), 26.9, 38, & 52
E	91	90.2	E_{1g}	91	-	E_2^1	85	81.4($\perp$)
A_1(TO,LO)	104	105.0	A_{1g}^1(TO,LO)	110	110		97	94.5
A_1(TO)	144	-				A_1 (LO)	151	150
A_1(LO)	180	-	A_1(TO)	175	-			
E	182	183.4	-				183	179.8
A_1(TO)	187	-	-					
A_1(LO)	193	-	-					202.5
A_1	203	204.4	A_{1g}^2(LO)	205	-		205	209.5
		-	-			E_2^2	224	228.5 ($\perp$)
A_1	237	-	-				233	-

Frequencies in cm^{-1}. ‡ References [46] & [47]; λ_{exc}: 488 nm & 532 nm, respectively. ♣ References. [48] & [4]; λ_{exc}: 633 nm. ◊ Reference [49] ; λ_{exc}: 514.5 nm. ⋆ This Work; λ_{exc}: 532 nm. ▼ Folded Acoustic, $\perp$ denotes modes remaining in cross-polarised $(z(xy)\bar{z})$ configuration.

Table 5.4: A comparison of previously observed Raman modes assigned to the α, β, and γ-polytypes of In_2Se_3, and those reported in this work.

Further to the In_2Se_3 phases discovered grown on GaSe, areas could be found with InSe-like spectra, as seen in figure ??. The Raman modes are listed in table 5.1, right most column. Besides those matching roughly with previously reported values, most closely with β-phase, there is an additional peak at 148.0 cm^{-1}. This peak appears only in $z(xx)\bar{z}$ polarisation configuration and has been assigned A-symmetry as a result. Relative to PDMS exfoliated InSe in figures 5.3 & 5.4, there is greatly increased Rayleigh scattering of the laser. The $z(xy)\bar{z}$ polarisation configuration removes a great deal of the Rayleigh scatter, and there are no E symmetric Raman peaks above the noise down to ± 10 cm^{-1}.

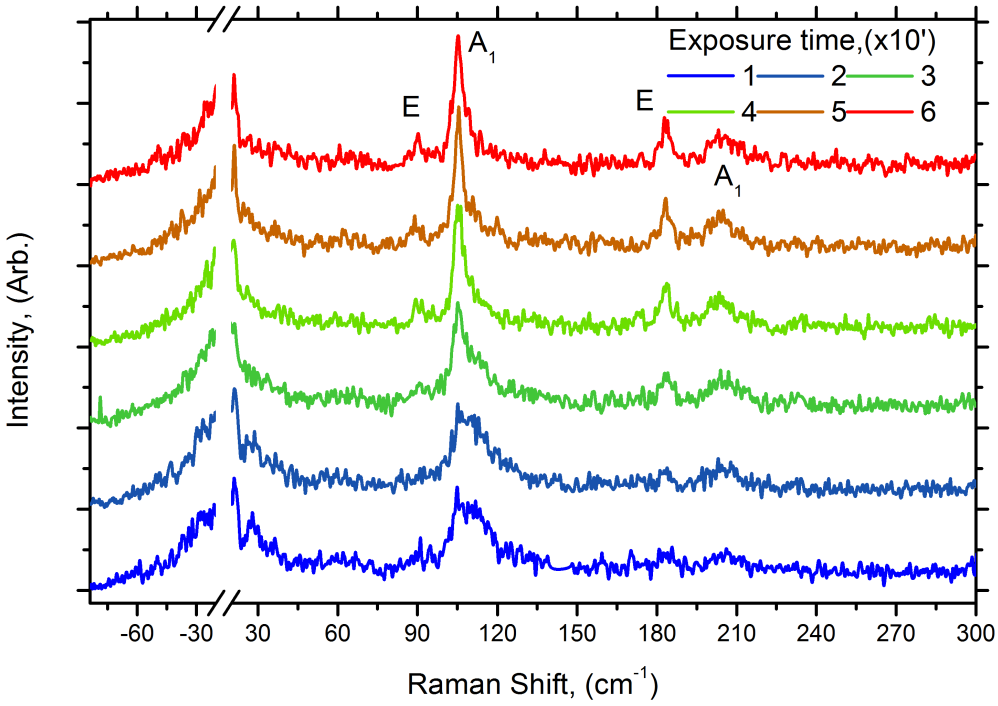

Figure 5.14(a): Co-polarised Raman spectra showing a photo annealing effect as a function of exposure time; the redshift of the A_1 peak at 109 cm^{-1} to 105 cm^{-1} is indicative of an $\beta \rightarrow \alpha$ In_2Se_3 phase transition.

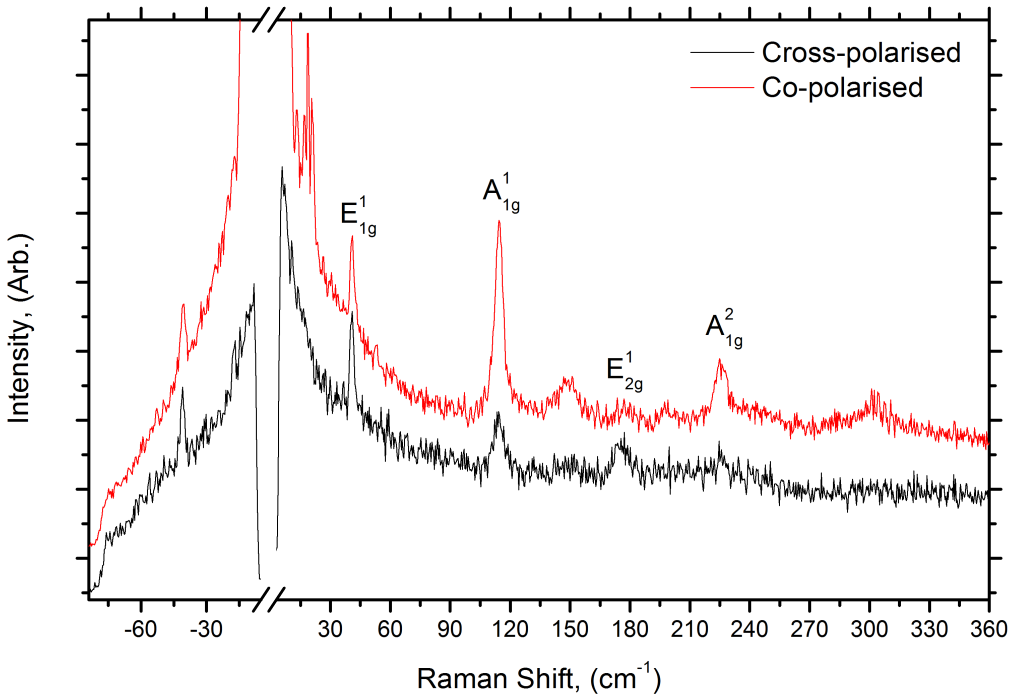

Figure 5.14(b): Co-, and cross-polarised Raman spectra of a region of InSe growth as could be found grown on thin GaSe flake regions.

5.3 Discussion

5.3.1 PDMS Exfoliated InSe

The observed peak shifts and FWHM broadening for the A^1_{1g} modes figure 5.3, agree with a previous study which also demonstrated the monolayer to be absent of crystalline phonon modes, whilst the bilayer lacked all but the A^1_{1g} mode, which was significantly broadened relative to thicker flakes [50]. The reason for this FWHM broadening and reduction in relative intensity of principal phonon modes is most likely due to degradation of the InSe flakes due to reaction with atmospheric species. Whilst InSe has been shown to be more stable under atmospheric exposure than GaSe, and GaS [51]–[53], it is, nevertheless vulnerable to reaction with H_2O at selenium vacancy sites [54]. The monolayer case, having the greatest surface area to volume ratio, is the least stable of the various thicknesses. The broad Raman peak at 303 cm^{-1} is likely to be related to the disorder, and evidence of chemical degradation, and it is known that In_2O_3 manifests a peak close to this value [55]–[57]. The match with other Raman modes of this oxide is poor, and without specific knowledge of the lattice vibration responsible for the peak around 303 cm^{-1} the plausibility of this assignment cannot be discussed further.

The presence of an A symmetric mode at 199.5 cm^{-1} is due to the A_1(LO) [32], this peak has previously been used as evidence of the presence of the ε-polytype InSe in spectra taken in backscattering geometry without polarisation resolution [50], due to previous observation of such a peak observed in near-right-angle scattering geometry work [28]. The observations in the present study demonstrate the care required in assigning Raman peaks in metal-monochalcogenides, the ambiguity is due to resonance effects at excitation energies around 2.4 eV activating infrared TO & LO modes, which are present in the non-resonant Raman spectra of non-centrosymetric InSe polytypes [58]. The PDMS bulk spectrum shows the same A symmetric mode at 194 cm^{-1} which is assigned as the A(LO) mode on the basis of the resonance effect of 532 nm excitation wavelngth, and the coincidence of the frequency of the mode observed in infrared spectroscopy [33]. The frequency shift between bulk and few layer could be explained by the fact that long range Coulomb interactions are responsible for the splitting of TO-LO modes; layer thinning alters the long-range dielectric environment, altering the frequency of the A_1(LO) mode.

Considering the low frequency modes below 45 cm^{-1} shown in figure 5.5; the E^1_{1g} peak appears to have a low frequency shoulder, this feature agrees with the conjugate mode due to Davydov splitting i.e. the splitting between two or more identical, coupled vibrational modes in a unit cell. This would be the case if one were to imagine an extended unit cell above the 2 layer thickness of the ε- or β- phase, as could be the case in longer range stacking sequences, or weakly-coupled stacks.

The frequency of the mode with out-of-phase vibration is given by $\nu_c = \sqrt{\nu_0^2 + \delta\bar{\nu}^2}$ [43], where the frequency ν_0 is that of the in-phase coupled mode, whilst the interlayer coupling

frequency $\delta\bar{\nu}$ is taken to be the frequency of the correct symmetry of rigid interlayer mode, for the lowest frequency Raman-active trilayer E^1_{1g} mode, this is the shear mode with frequency 12.3 cm^{-1}. For the E^1_{1g} mode in trilayer at 40.9 cm^{-1}, which should be the frequency of the mode with out-of-phase vibration, the lowest frequency Raman-active Davydov-split mode should be 38.9 cm^{-1}, this matches well with the observed frequency at (38.7±0.1) cm^{-1}. The laser excitation close to the excitonic resonance at 2.4 eV [59]–[61] is likely to be a contributing factor in the observation of Davydov splitting in InSe, as is the case with other metal-chalcogenides WSe_2 [35], $MoSe_2$ [35], & $MoTe_2$ [62], [63].

The E^1_{1g} peak in the bilayer InSe flake is seen to be greatly reduced, relative to tri- and bulk samples. The remnant of the peak is observed more easily in the full-range spectrum in figure 5.3, its reduction is approximately commensurate with the other normal modes of the lattice suggesting that chemical degradation of the lattice is responsible for the reduction in Raman intensity.

The remaining ultra low frequency modes, below the E^1_{1g} are exclusively E-symmetric, demonstrating that no interlayer breathing modes are observed. The highest frequency shear mode peak shifts for, bilayer, trilayer, and bulk InSe are 33%, 35% & 46% less than in the TMD MoS_2 of 23 cm^{-1}, 26 cm^{-1} , 31.8 cm^{-1}, respectively. For the bilayer, by considering the change in mass due to InSe atoms relative to those of MoS_2, scaling yields a value of 14.8 cm^{-1}, which agrees well with the value experimentally determined, 15.5 cm^{-1}. The increasing discrepancy in the trilayer, and bulk suggests that long range, multilayer coupling is much weaker than in TMDs, theoretical studies of GaSe shear and breathing modes concluded the interlayer coupling to be “Ultra-weak” [64]. For the same mass scaling arguments, the GaSe bilayer shear mode is estimated to be 16.9 cm^{-1}, which gives a 33% discrepancy with the value calculated by DFT [64], indicating that the interlayer coupling between different metal-monochalcogenides varies significantly due to the metal species, likely due to the change of ionicity owing to the differences in electronegativities, or a modification of the long range forces, requiring consideration of next-nearest-neighbour interactions.

In the trilayer sample two shear mode peaks are present, these are the two shear mode frequencies, with outer layers vibrating in phase; 17.0 cm^{-1} and out-of-phase; 12.3 cm^{-1}. The fact that that these two peaks should be observed in the trilayer, and with the lower frequency mode manifesting greater intensity is indicative of mixed 2H/3R polytypism, as has been observed in $MoSe_2$ [65].

In the figure 5.6, where additional InSe thicknesses are plotted, it can be seen that for a given layer number, N; $(N-1)$ modes are observed. Group theory considerations of the symmetries of few layer InSe structures excludes the Raman activity of the modes along even index branches in even layer number β-phase flakes, whilst the backscattering configuration should reduce the observed modes to only those along odd index branches. For ε-phase flakes, all shear modes

should be Raman active, with the backscattering configuration preventing observation of even index branches in odd layer number flakes. Such a phenomenon has been observed in CVD grown $MoSe_2$ flakes where stacking orders deviated from 2H, 3R, but remained uncharacterised [65]. Bond polarisability models were able to confirm non-zero Raman activity for all shear modes, without the constraints of Group theory [41]. As in the case with the observed Davydov doublet of the E^1_{1g} mode, the laser excitation close to the excitonic resonance at 2.4 eV [59] is likely to be a significant contributing factor to the observation of such a high proportion of interlayer shear mode peaks.

In re-stacked graphene multi-layers, the relatively weak interlayer coupling at the stacking interface, alowed the observation of the shear modes of the constituent thicknesses, superposed, rather than the shear mode of the resulting thickness flake [66], thus demonstrating how stacking faults can influence the observed interlayer modes of multilayer samples. It is along these lines that the shear mode band of bulk InSe can be understood; that the weak interlayer coupling in InSe is unable to maintain a single stacking order over long ranges, allowing concurrent observation of multiple shear modes in bulk flakes.

The trends for the low frequency shear modes are plotted in figure 5.6 b, the observed modes fall into branches highlighted by differing plot colours, also branches of a linear chain model's (LCM) have been plotted as green curves, due to the equation 5.2. There is good agreement between the LCM and the highest frequency shear mode branch, but this concordance decreases along the branch index with the LCM under-predicting the frequency of the branch's modes. What this discrepancy suggests is that there may be some additional restoring force for shear modes with layers vibrating with relative phases less than π, i.e. those other than the highest frequency branch. Next-nearest neighbour, intralayer interactions, or anharmonicities are not considered in the linear chain model. A candidate lattice mode to consider as a source of some additional restoring force would be the E^1_{1g} mode which manifests a Davydov splitting due to the interlayer coupling. Nearest neighbour interactions might play a more significant role in InSe and other metal monochalcogenides due to the difference in the ionicity of the intralayer bonding, altering the interlayer bonding and the relative long range forces, in comparrison with TMDs such as MoS_2 where interlayer bonding is not exclusively vdW type, but displays some covalent character [41].

The bulk sample in figure 5.4 shows two obvious shear modes peaks, with a higher frequency shoulder in both the Stokes and anti-stokes spectra. The bulk is not expected to have more than a single Raman active shear mode, and the presence of three is suggestive of some decoupling within the flake, so as to render the topmost layers uncoupled from the bulk flake. The mechanism of this decoupling is likely mixed polytypism in the InSe bulk flake.

5.3.2 Hexagonal Boron Nitride Encapsulated InSe

It might be expected that h-BN encapsulated InSe should behave in a manner equivalent to PDMS exfoliated samples, only with greater environmental stability due to the boron nitride encapsulation in an argon atmosphere. Indeed, it can be seen that the agreement of the fre-

quencies of the lattice normal modes is quite close above the ultra low frequency region. What may be inferred, however, from the behaviour of the A_{1g} mode at ≈ 115 cm^{-1} is that the h-BN capping masks the modification due to the reduction of InSe layer thinning of this out-of -plane mode, as it shows no variation over a thickness change of a factor of 10, between 3.5 nm and 30 nm.

The E^1_{1g} mode manifests a very similar behaviour to the PDMS samples; the frequencies are in good agreement, and the shifts between the 4 nm and 30 nm flakes are comparable to those between trilayer and bulk PDMS samples.

The absence of the E^1_{1g} mode in the 3.5 nm flake is in agreement with the PDMS bilayer flake, although this is perhaps due to the presence of the Raman modes of air present in this region, rather than some intrinsic Raman inactivity, which would be unexpected. Considering the broad feature around 303 cm^{-1} which appears to increase in prominence in reduced-thickness samples, and is indicative of atmospheric reaction, being the only mode common between the PDMS exfoliated monolayer and thicker flakes.

The hBN encapsulation under inert atmosphere was intended to prevent reaction between InSe and air, but according to the observation of the peak at ≈ 303 cm^{-1}, this method of passivation is not effective for InSe.

The reason as to why the hBN encapsulation did not prevent the degradation might be explained by the evidence of air trapped within the samples seen most easily in figure 5.8. This air is unlikely to have become trapped during the encapsulation, given the argon glovebox atmosphere, rather – and more likely – is that during transport of the bulk materials, which seldom takes place in vacuum or under inert gas, air could have been adsorbed into either of the component materials. It is also possible that the presence of air is due to absorption by the adhesive of the tape used to exfoliate the materials, which could be the source of hydrocarbon residues detected in vdW Heterostructures [67].

No un-encapsulated exfoliated samples have been reported to show adsorbed air, but in similar hBN encapsulated TMD heterobilayers there are identifiable O_2 & N_2 Raman peaks, albeit at much lower concentrations than in these hBN encapsulated InSe samples, meaning the assignment of air Raman modes was not possible previously. The question of why InSe encapsulated samples contain much greater concentrations of air, than comparably fabricated h-BN encapsulated TMD heterobilayers might be due once again, to the "Ultra Weak" interlayer coupling in InSe allowing intercalation of O_2 and N_2 molecules.

AFM images in figure 5.9 show multiple bubble-like features, which are likely to be the contamination responsible for the presence of air. The flakes in figures 5.9c & 5.9a appear to show the contamination preferentially occurring on the InSe flake. The thinnest flake in figure 5.9b meanwhile shows a more even distribution between the InSe and the hBN, but with distinct sizes, the InSe contamination appearing to have aggregated into fewer, larger bubble regions.

Regarding the ultra low frequency Raman modes, which in hBN-encapsulated InSe show the greatest variation with thickness; similar to the PDMS exfoliated flakes, only E-symmetric modes i.e. shear modes are observed. In the 3.5 nm flake only one shear mode is observed at 15.8 cm^{-1} which is a similar in its isolation, and frequency to the PDMS bilayer flake. AFM of TMDs is known to produce height measurements with systematic errors of ≈ 0.7 nm even in correctly calibrated instruments, due to contamination of the substrate or flake; given this error, the flake could be assigned as a bilayer.

The 4 nm flake might then be expected to be a trilayer, given its measured thickness, 0.5 nm greater than the assigned bilayer flake. The low frequency modes in this case disagree with those of the PDMS trilayer, there being only a single shear mode peak at 10.1 cm^{-1}, which should correspond to the lowest frequency shear mode branch, but is present in spite of the lack of Raman activity of the highest frequency, out-of-phase interlayer layer vibration, which should have considerably greater scattering intensity. Considering the low frequency shear modes of TMDs, it is observed in 3R-polytypes that the lowest frequency shear mode branch is the only Raman active mode, consequently this trilayer can be assigned as being exclusively 3R-polytype.

The 15 nm thickness lacks any identifiable shear modes and manifests stronger Rayleigh scattering tails which may obscure any modes present. Alternatively, if the flake is of 3R-polytype, with odd-layer number, then the only Raman active shear mode should be the lowest frequency phase shear mode, then at a thickness of 15 nm the mode would be expected to occur below the cut off frequency of the Bragg notch filters, and thus not observed.

The 30 nm flake displays two shear modes with frequency 11.6 cm^{-1} & 16.4 cm^{-1}, such a thickness of TMD would be expected to have values very close to the bulk. Comparing with the values for PDMS exfoliated bulk InSe, yields difference of 3.5 cm^{-1} & 0.8 cm^{-1} for the lower and higher frequency modes, respectively. The higher frequency mode of the two can be assigned as the highest frequency, out-of-phase interlayer layer vibration, whilst the lower frequency mode may be a Davydov-split mode occurring between neighbouring 2-layer unit cells, or – more likely – an indicator of mixed polytypism, but with a distinct ordering to the PDMS exfoliated flake.

5.3.3 Epitaxially grown In_2Se_3 on GaSe

In_2Se_3 growth on β-GaSe resulted in regions where each of the following three phases of In_2Se_3 could be observed, namely the α-, β-, and γ-polytypes. Whilst for a single growth temperature, and over a very limited spatial dimension, it might be expected that only a single phase of In_2Se_3 should be observed, previous substrate selectivity has been observed for In_2Se_3 polytypes [68].

γ-In_2Se_3 appears to grow preferentially at the GaSe flake discontinuities, as seen by the resulting red contrast areas in the 5.11b In_2Se_3/GaSe optical micrograph, similar to reference [68], where the substrate selected for the In_2Se_3 phase and the film morphology. It is also known that GaSe is not stable under atmospheric conditions [69], thus crystal plateaux, are likely to have oxidised to some degree before they are placed in an evacuated furnace chamber for InSe growth, whilst the cracked area may only become exposed by a chemical etching under the

furnace conditions. This idea of etching is evidenced by the reduced abruptness of the GaSe flake edges between panels (a) & (b) of figure 5.11, and the AFM height image in panel (c). These same regions upon which γ-In_2Se_3 grows also manifest higher concentrations of selenium relative to the plateau regions, whilst the indium concentrations are higher in these areas also, the difference above the mean and background (substrate) areas is less obvious.

It was remarkable that throughout the study no observation of the Raman modes of GaSe was made; the initially 150 nm thick GaSe flake, might have been expected to survive the growth process, but the gallium EDX in figure 5.11 h, shows a concentration close to the background level of the substrate, and largely appears to have been substituted by indium. The EDX technique has a penetration depth of 1-2 μm, i.e. sufficient to detect gallium though the indium selenide growth. Both gallium and indium are known to diffuse large distances, ($\approx$ 200 nm) through crystalline lattices at elevated temperatures [68], [70], [71].

The Raman modes for γ-phase are not entirely understood and there exist some discrepancies in the modes below 100 cm^{-1} [20], [44], [49], [72], [73]. These modes have been attributed to folded acoustic phonon modes due to finite domain sizes in films assumed to be amorphous [44] creating a superlattice-like folded zone scheme, the evidence for this, however, is weak. Most measured γ-phase samples were determined to be crystaline [20], [49], [72], [73], and so discrepancies in the observed frequencies are more likely due to the effects of the vacancy ordering the in the defect-wurtzite structure.

Figure ?? shows multiple accumulations with increasing exposure time; the A mode at 110 cm^{-1} is seen to redshift to 105 cm^{-1}, whilst the two modes at 183 & 204 cm^{-1} grow slightly in intensity.

This redshift has previously been used as evidence of a $\beta \rightarrow \alpha$ phase change, detailed calculations confirm the experimental observation that the Raman active A_1 mode undergoes a blue shift when the In_2Se_3 structure transforms from the α-phase to the β-phase [22]. It has been established that the β-phase is the ground state of the In_2Se_3 system at standard temperatures [22], and thermal annealing serves to drive a phase change only in the $\alpha \rightarrow \beta$ direction. Thus the photo-annealing phase change from $\beta \rightarrow \alpha$ should not be due to a thermal effect since elevated temperatures transform in the opposite direction, instead the restructuring is a result of some other mechanism. Comparison with the observed Raman modes rhombohedral and trigonal phases of S_6 molecules [45] rules out evaporation of Indium resulting in a residual Selenium film. Previously observation has been made of an intrapolytypic transformation at -125 °C, due to a CDW-like softening and freezing in of a phonon mode, creating a periodic Peierls-like distortion of the lattice due to indium atom bunching along $x - y$ [18], [19].

InSe-like growth was observed with a representative spectrum in figure ??, the Raman peak shifts are tabulated along with those from previous observations made in bulk InSe, table 5.1. There is small discrepancy between the values of the Raman wavenumbers of this growth and

the bulk values, with the closest match being the β-phase. The redshift of the A^1_{1g} peak at 114.3 cm^{-1} relative to the β-phase bulk value at 115.4 cm^{-1} may indicate few-layer growth, or decreased interlayer coupling, as seen in reduced thickness of PDMS samples in 5.3. It has previosly been shown that GaS doping of InSe has the effect of redshifting the A^1_{1g} mode from 117 cm^{-1} to 114 cm^{-1} at GaS concentration of 2.5 ppm [74]. The effect off GaSe dopants could account for this redshift. The linewidth of the InSe-like growth A^1_{1g} is (5.0±0.1) cm^{-1} mode is double that of the PDMS exfoliated A^1_{1g}; (2.5±0.1) cm^{-1} suggesting reduced crystalline order. This is reduction in crystalline is corroborated by the presence of the A^1_{1g} peak in the $(z(xy)\bar{z})$ cross polarisation, which should not be Raman active in this configuration. The presence of a peak at 149 cm^{-1} does not correspond to any InSe vibrational mode at Γ; Raman, or infrared active. but does match closely to the A symmetric mode of γ-In_2Se_3.

5.4 Summary

Presented here are Raman measurements of diverse indium-selenium compounds, isolated by novel means, which demonstrate the suitability of Raman spectroscopy as a tool to discriminate and characterise this group of compounds. The differences between InSe and the TMDs' is highlighted by the poly-polytypism i.e. the weak interlayer coupling resulting in the coexistence of multiple stacking orders in a single flake, which is studied here with ultra low frequency Raman spectroscopy for the first time. The excitation resonance near 2.4 eV [59] allows observation of all existing interlayer shear modes, even those forbidden in back scattering geometry providing determination of the PDMS exfoliated stacking order to be of ε-, AB type. The linear chain mode is implemented to compare the interlayer shear modes of InSe with those predicted for GaSe; agreement of the highest frequency branch is good, but discrepancies compound when advancing along the branch index with the LCM under-predicting the frequencies of these modes.

In InSe flakes encapsulated in hexagonal boron nitride, the high frequency Raman (>100 cm^{-1}) provide no indication of the interlayer interaction, but the low frequency Raman provides insight into the interlayer coupling. This valuable information provides means by which InSe can be understood when integrated in vdW heterostructures. The presence of air is reported in the encapsulated samples, which given the argon atmosphere in which the fabrication took place, is unexpected. This finding suggests that contamination of the bulk source materials, and the adhesive tapes used of exfoliation needs to be carefully considered for the fabrication of ultra-clean vdW heterostructures.

In_2Se_3 films grown epitaxially on GaSe are shown to be poly-morphic, and these phases are linked to the regions of GaSe substrate where they grow, α-, β-, & γ- phases are identified, in addition to regions of InSe. Laser photo-annealing is shown to drive a phase change from the groundstate $\beta \rightarrow \alpha$ phase, which is against the thermodynamic gradient. The Raman spectra

provide a basis on which growth procedures may be evaluated in order to produce any of the desired compounds, all of which present a technological importance.

References

[1] L. Y. Kharkhalis, K. E. Glukhov, and M. Sznajder, "Peculiarities of chemical bonding in crystals of the In–Se system," *Acta Physica Polonica A*, vol. 126, no. 5, pp. 1146–1148, 2014, ISSN: 1898794X. DOI: 10.12693/APhysPolA.126.1146.

[2] R. Frisenda, E. Navarro-Moratalla, P. Gant, D. Pérez De Lara, P. Jarillo-Herrero, R. V. Gorbachev, and A. Castellanos-Gomez, "Recent progress in the assembly of nanodevices and van der Waals heterostructures by deterministic placement of 2D materials," *Chemical Society Reviews*, 2018, ISSN: 0306-0012. DOI: 10.1039/C7CS00556C. [Online]. Available: http://xlink.rsc.org/?DOI=C7CS00556C.

[3] F. Bonaccorso, A. Lombardo, T. Hasan, Z. Sun, L. Colombo, and A. C. Ferrari, "Production and processing of graphene and 2d crystals," *Materials Today*, vol. 15, no. 12, pp. 564–589, Dec. 2012, ISSN: 13697021. DOI: 10.1016/S1369-7021(13)70014-2. [Online]. Available: http://linkinghub.elsevier.com/retrieve/pii/S1369702113700142.

[4] N. Balakrishnan, C. R. Staddon, E. F. Smith, J. Stec, D. Gay, G. W. Mudd, O. Makarovsky, Z. R. Kudrynskyi, Z. D. Kovalyuk, L. Eaves, A. Patanè, and P. H. Beton, "Quantum confinement and photoresponsivity of β -In_2Se_3 nanosheets grown by physical vapour transport," *2D Materials*, vol. 3, no. 2, p. 025 030, Jun. 2016, ISSN: 2053-1583. DOI: 10.1088/2053-1583/3/2/025030. [Online]. Available: http://stacks.iop.org/2053-1583/3/i=2/a=025030?key=crossref.6f4238c64447132c5b5718bedbefd5de.

[5] N. Balakrishnan, Z. R. Kudrynskyi, E. F. Smith, M. W. Fay, O. Makarovsky, Z. D. Kovalyuk, L. Eaves, P. H. Beton, and A. Patanè, "Engineering p – n junctions and bandgap tuning of InSe nanolayers by controlled oxidation," *2D Materials*, vol. 4, no. 2, p. 025 043, Mar. 2017, ISSN: 2053-1583. DOI: 10.1088/2053-1583/aa61e0. [Online]. Available: http://stacks.iop.org/2053-1583/4/i=2/a=025043?key=crossref.e7427e14a004eca2c4bd6d2655ddcadf.

[6] V. Zólyomi, N. D. Drummond, and V. I. Fal'ko, "Electrons and phonons in single layers of hexagonal indium chalcogenides from ab initio calculations," *Physical Review B*, vol. 89, no. 20, p. 205 416, May 2014, ISSN: 1098-0121. DOI: 10.1103/PhysRevB.89.205416. [Online]. Available: http://link.aps.org/doi/10.1103/PhysRevB.89.205416%20https://link.aps.org/doi/10.1103/PhysRevB.89.205416.

[7] A. Kuhn, A. Chevy, and R. Chevalier, "Crystal structure and interatomic distances in GaSe," *Physica Status Solidi (a)*, vol. 31, no. 2, pp. 469–475, Oct. 1975, ISSN: 00318965. DOI: 10.1002/pssa.2210310216. [Online]. Available: http://doi.wiley.com/10.1002/pssa.2210310216.

[8] A. Chevy, "Growth of indium selenides by vapour phase chemical transport; polytypism of indium monoselenide," *Journal of Crystal Growth*, vol. 51, no. 2, pp. 157–163, Feb. 1981, ISSN: 00220248. DOI: 10.1016/0022-0248(81)90296-7. [Online]. Available: http://linkinghub.elsevier.com/retrieve/pii/0022024881902967.

[9] C. De Blasi, D. Manno, and S. Mongelli, "The stacking of polytypes in InSe crystals," *physica status solidi (a)*, vol. 90, no. 1, K5–K6, Jul. 1985, ISSN: 00318965. DOI: 10.1002/pssa.2210900145. [Online]. Available: http://doi.wiley.com/10.1002/pssa.2210900145.

[10] H. Lee, D. H. Kang, and L. Tran, "Indium selenide (In2Se3) thin film for phase-change memory," *Materials Science and Engineering B: Solid-State Materials for Advanced Technology*, vol. 119, no. 2, pp. 196–201, 2005, ISSN: 09215107. DOI: 10.1016/j.mseb.2005.02.060.

[11] B. Yu, S. Ju, X. Sun, G. Ng, T. D. Nguyen, M. Meyyappan, and D. B. Janes, "Indium selenide nanowire phase-change memory," *Applied Physics Letters*, vol. 91, no. 13, p. 133 119, Sep. 2007, ISSN: 0003-6951. DOI: 10.1063/1.2793505. [Online]. Available: http://aip.scitation.org/doi/10.1063/1.2793505.

[12] A. M. Rasmussen, E. Mafi, W. Zhu, Y. Gu, and M. D. McCluskey, "High pressure γ-to-β phase transition in bulk and nanocrystalline In 2 Se 3," *High Pressure Research*, vol. 7959, no. November 2017, pp. 1–8, 2016, ISSN: 0895-7959. DOI: 10.1080/08957959.2016.1214729. [Online]. Available: https://www.tandfonline.com/doi/full/10.1080/08957959.2016.1214729.

[13] G. Han, Z. G. Chen, J. Drennan, and J. Zou, "Indium selenides: Structural characteristics, synthesis and their thermoelectric performances," *Small*, vol. 10, no. 14, pp. 2747–2765, 2014, ISSN: 16136829. DOI: 10.1002/smll.201400104.

[14] J. Ye, S. Soeda, Y. Nakamura, and O. Nittono, "Crystal Structures and Phase Transformation in In 2 Se 3 Compound Semiconductor," *Japanese Journal of Applied Physics*, vol. 37, no. Part 1, No. 8, pp. 4264–4271, Aug. 1998, ISSN: 0021-4922. DOI: 10.1143/JJAP.37.4264. [Online]. Available: http://stacks.iop.org/1347-4065/37/4264.

[15] A. Likforman, P. H. Fourcroy, M. Guittard, J. Flahaut, R. Poirier, and N. Szydlo, "Transitions de la forme de haute température α de In2Se3, de part et d'autre de la température ambiante," *Journal of Solid State Chemistry*, vol. 33, no. 1, pp. 91–97, 1980, ISSN: 1095726X. DOI: 10.1016/0022-4596(80)90551-4.

[16] A. Pfitzner and H. Lutz, "Redetermination of the Crystal Structure of γ-In2Se3by Twin Crystal X-Ray Method," *Journal of Solid State Chemistry*, vol. 124, no. 2, pp. 305–308, 1996, ISSN: 00224596. DOI: 10.1006/jssc.1996.0241. [Online]. Available: http://www.sciencedirect.com/science/article/pii/S0022459696902418.

[17] S. Popović, A. Tonejc, B. Gržeta-Plenković, B. Čelustka, R. Trojko, and IUCr, "Revised and new crystal data for indium selenides," *Journal of Applied Crystallography*, vol. 12, no. 4, pp. 416–420, 1979, ISSN: 0021-8898. DOI: 10.1107/S0021889879012863. [Online]. Available: http://scripts.iucr.org/cgi-bin/paper?S0021889879012863.

[18] J. van Landuyt, G. van Tendeloo, and S. Amelinckx, "Phase transitions in In2Se3 as studied by electron microscopy and electron diffraction," *Physica Status Solidi (a)*, vol. 30, no. 1, pp. 299–314, Jul. 1975, ISSN: 00318965. DOI: 10.1002/pssa.2210300131. [Online]. Available: http://doi.wiley.com/10.1002/pssa.2210300131.

[19] ——, "Electron diffraction study of inter- and intrapolytypic phase transitions in transition metal dichalcogenides. I. Electron diffraction patterns," *Physica Status Solidi (a)*, vol. 26, no. 1, pp. 359–376, Nov. 1974, ISSN: 00318965. DOI: 10.1002/pssa.2210260138. [Online]. Available: http://doi.wiley.com/10.1002/pssa.2210260138.

[20] S. Marsillac, A. Combot-Marie, J. Bernède, and A. Conan, "Experimental evidence of the low-temperature formation of γ-In2Se3 thin films obtained by a solid-state reaction," *Thin Solid Films*, vol. 288, no. 1-2, pp. 14–20, 1996, ISSN: 00406090. [Online]. Available: http://www.sciencedirect.com/science/article/pii/S0040609096087998.

[21] L. Debbichi, O. Eriksson, and S. Lebègue, "Two-Dimensional Indium Selenides Compounds: An Ab Initio Study," *Journal of Physical Chemistry Letters*, vol. 6, no. 15, pp. 3098–3103, 2015, ISSN: 19487185. DOI: 10.1021/acs.jpclett.5b01356.

[22] W. Ding, J. Zhu, Z. Wang, Y. Gao, D. Xiao, Y. Gu, Z. Zhang, and W. Zhu, "Prediction of intrinsic two-dimensional ferroelectrics in In2Se3 and other III2-VI3 van der Waals materials," *Nature Communications*, vol. 8, p. 14 956, Apr. 2017, ISSN: 2041-1723. DOI: 10.1038/ncomms14956. [Online]. Available: http://www.nature.com/doifinder/10.1038/ncomms14956.

[23] A. M. Rasmussen, S. T. Teklemichael, E. Mafi, Y. Gu, and M. D. McCluskey, "Pressure-induced phase transformation of In 2 Se 3," *Applied Physics Letters*, vol. 102, no. 6, p. 062 105, Feb. 2013, ISSN: 0003-6951. DOI: 10.1063/1.4792313. [Online]. Available: http://aip.scitation.org/doi/10.1063/1.4792313.

[24] X. Tao and Y. Gu, "Crystalline–Crystalline Phase Transformation in Two-Dimensional In_2Se_3 Thin Layers," *Nano Letters*, vol. 13, no. 8, pp. 3501–3505, Aug. 2013, ISSN: 1530-6984. DOI: 10.1021/nl400888p. [Online]. Available: http://pubs.acs.org/doi/abs/10.1021/nl400888p%20http://pubs.acs.org/doi/10.1021/nl400888p.

[25] M. Osman, Y. Huang, W. Feng, G. Liu, Y. Qiu, and P. Hu, "Modulation of opto-electronic properties of InSe thin layers via phase transformation," *RSC Advances*, vol. 6, no. 74, pp. 70 452–70 459, 2016, ISSN: 2046-2069. DOI: 10.1039/C6RA13543A. [Online]. Available: http://xlink.rsc.org/?DOI=C6RA13543A.

[26] C.-H. Ho, Y.-C. Chen, and C.-C. Pan, "Structural phase transition and erasable optically memorized effect in layered γ-In_2Se_3 crystals," *Journal of Applied Physics*, vol. 115, no. 3, p. 033 501, Jan. 2014, ISSN: 0021-8979. DOI: 10.1063/1.4862184. [Online]. Available: http://aip.scitation.org/doi/10.1063/1.4862184.

[27] J.-U. Lee, J. Park, Y.-W. Son, and H. Cheong, "Anomalous excitonic resonance Raman effects in few-layered MoS_2," *Nanoscale*, vol. 7, no. 7, pp. 3229–3236, 2015, ISSN: 2040-3364. DOI: 10.1039/C4NR05785F. [Online]. Available: http://xlink.rsc.org/?DOI=C4NR05785F.

[28] S. Jandl and C. Carlone, "Raman spectrum of crystalline InSe," *Solid State Communications*, vol. 25, no. 1, pp. 5–8, 1978, ISSN: 00381098. DOI: 10.1016/0038-1098(78)91157-2.

[29] T. Ikari, S. Shigetomi, and K. Hashimoto, "Crystal Structure and Raman Spectra of InSe," *physica status solidi (b)*, vol. 111, no. 2, pp. 477–481, Jun. 1982, ISSN: 03701972. DOI: 10.1002/pssb.2221110208. [Online]. Available: http://doi.wiley.com/10.1002/pssb.2221110208.

[30] K. Kumazaki and K. Imai, "Far-Infrared Reflection and Raman Scattering Spectra in γ-InSe," *physica status solidi (b)*, vol. 149, no. 2, K183–K186, Oct. 1988, ISSN: 03701972. DOI: 10.1002/pssb.2221490263. [Online]. Available: http://doi.wiley.com/10.1002/pssb.2221490263.

[31] G. L. Belenkii, L. N. Alieva, R. K. Nani, and E. Y. Salaev, "Vibrational Spectrum of InSe," *Physica Status Solidi (b)*, vol. 82, no. 2, pp. 705–709, Aug. 1977, ISSN: 03701972. DOI: 10.1002/pssb.2220820238. [Online]. Available: http://doi.wiley.com/10.1002/pssb.2220820238.

[32] N. M. Gasanly, B. M. Yavadov, V. I. Tagirov, and E. A. Vinogradov, "Infrared and Raman Spectra of Layer InSe Single Crystals," *physica status solidi (b)*, vol. 89, no. 1, K43–K48, 1978, ISSN: 15213951. DOI: 10.1002/pssb.2220890155.

[33] G. L. Belenkii and V. B. Stopachinskiĭ, "Electronic and vibrational spectra of III-VI layered semiconductors," *Soviet Physics Uspekhi*, vol. 26, no. 6, pp. 497–517, Jun. 1983, ISSN: 0038-5670. DOI: 10.1070/PU1983v026n06ABEH004420. [Online]. Available: https://doi.org/10.1070/PU1983v026n06ABEH004420.

[34] O. A. Balitskii, V. P. Savchyn, and V. O. Yukhymchuk, "Raman investigation of InSe and GaSe single-crystals oxidation," *Semiconductor Science and Technology*, vol. 17, no. 2, pp. L1–L4, 2002, ISSN: 0268-1242. DOI: 10.1088/0268-1242/17/2/101. [Online]. Available: http://stacks.iop.org/0268-1242/17/i=2/a=101?key=crossref.9de00979d2116ff0dcbef1982cd8c42a.

[35] S. Kim, K. Kim, J.-U. Lee, and H. Cheong, "Excitonic resonance effects and Davydov splitting in circularly polarized Raman spectra of few-layer WSe_2," *2D Materials*, vol. 4, no. 4, p. 045 002, Aug. 2017, ISSN: 2053-1583. DOI: 10.1088/2053-1583/aa8312. arXiv: 1612.05879. [Online]. Available: https://arxiv.org/ftp/arxiv/papers/1708/1708.00126.pdf%20http://stacks.iop.org/2053-1583/4/i=4/a=045002?key=crossref.081d6ef1060602b8c7c7aa9c344b2858.

[36] J. B. Wu, Z. X. Hu, X. Zhang, W. P. Han, Y. Lu, W. Shi, X. F. Qiao, M. Ijias, S. Milana, W. Ji, A. C. Ferrari, and P.-H. Tan, "Interface Coupling in Twisted Multilayer Graphene by Resonant Raman Spectroscopy of Layer Breathing Modes," *ACS Nano*, vol. 9, no. 7, pp. 7440–7449, 2015, ISSN: 1936086X. DOI: 10.1021/acsnano.5b02502. arXiv: arXiv:1505.00095v1.

[37] H. Wang, Y. Liu, M. Li, H. Huang, H. M. Xu, R. J. Hong, and H. Shen, "Review on the Raman spectroscopy of different types of layered materials," *Optoelectronics and Advanced Materials, Rapid Communications*, vol. 4, no. 8, pp. 1166–1169, 2016, ISSN: 18426573. DOI: 10.1039/b000000x. [Online]. Available: http://dx.doi.org/10.1039/c5nr07205k.

[38] Q. J. Song, Q.-H. Tan, X. Zhang, J. B. Wu, B. W. Sheng, Y. Wan, X. Q. Wang, L. Dai, and P.-H. Tan, "Physical origin of Davydov splitting and resonant Raman spectroscopy of Davydov components in multilayer $MoTe_2$," *Physical Review B*, vol. 93, no. 11, p. 115 409, Mar. 2016, ISSN: 2469-9950. DOI: 10.1103/PhysRevB.93.115409. [Online]. Available: https://link.aps.org/doi/10.1103/PhysRevB.93.115409.

[39] Q.-H. Tan, Y.-J. Sun, X.-L. Liu, Y. Zhao, Q. Xiong, P.-H. Tan, and J. Zhang, "Observation of forbidden phonons and dark excitons by resonance Raman scattering in few-layer WS_2," *2D Materials*, vol. 4, p. 1704.01315, 2017. DOI: https://doi.org/10.1088/2053-1583/aa79bb. arXiv: arXiv:1704.01315v1. [Online]. Available: https://arxiv.org/pdf/1704.01315.pdf.

[40] X.-F. Qiao, J.-B. Wu, L.-W. Zhou, J.-S. Qiao, W. Shi, T. Chen, X. Zhang, J. Zhang, W. Ji, and P.-H. Tan, "Polytypism and unexpected strong interlayer coupling in two-dimensional layered ReS_2," *Nanoscale*, vol. 8, no. 15, pp. 8324–8332, 2016, ISSN: 2040-3364. DOI: 10.1039/C6NR01569G. arXiv: 1512.08935. [Online]. Available: http://arxiv.org/abs/1512.08935%0A%20http://dx.doi.org/10.1039/c6nr01569g%20http://xlink.rsc.org/?DOI=C6NR01569G.

[41] X. Luo, X. Lu, C. Cong, T. Yu, Q. Xiong, and S. Ying Quek, "Stacking sequence determines Raman intensities of observed interlayer shear modes in 2D layered materials-A general bond polarizability model," *Scientific Reports*, vol. 5, no. April, pp. 1–13, 2015, ISSN: 20452322. DOI: 10.1038/srep14565. arXiv: 1504.04947. [Online]. Available: http://dx.doi.org/10.1038/srep14565.

[42] J. Irwin, R. Hoff, B. Clayman, and R. Bromley, "Long wavelength lattice vibrations in GaS and GaSe," *Solid State Communications*, vol. 13, no. 9, pp. 1531–1536, Nov.

1973, ISSN: 00381098. DOI: 10.1016/0038-1098(73)90205-6. [Online]. Available: http://linkinghub.elsevier.com/retrieve/pii/0038109873902056.

[43] T. J. Wieting and J. L. Verble, "Interlayer Bonding and the Lattice Vibrations of β-GaSe," *Physical Review B*, vol. 5, no. 4, pp. 1473–1479, Feb. 1972, ISSN: 0556-2805. DOI: 10.1103/PhysRevB.5.1473. [Online]. Available: https://link.aps.org/doi/10.1103/PhysRevB.5.1473.

[44] J. Weszka, P. Daniel, A. Burian, A. M. Burian, and A. T. Nguyen, "Raman scattering in In2Se3 and InSe2 amorphous films," *Journal of Non-Crystalline Solids*, vol. 265, no. 1, pp. 98–104, 2000, ISSN: 00223093. DOI: 10.1016/S0022-3093(99)00710-3.

[45] K. Nagata, K. Ishibashi, and Y. Miyamoto, "Raman and Infrared Spectra of Rhombohedral Selenium," *Japanese Journal of Applied Physics*, vol. 20, no. 3, pp. 463–469, Mar. 1981, ISSN: 0021-4922. DOI: 10.1143/JJAP.20.463. [Online]. Available: http://iopscience.iop.org/article/10.1143/JJAP.20.463/meta.

[46] R. Lewandowska, R. Bacewicz, J. Filipowicz, and W. Paszkowicz, "Raman scattering in alpha-In2Se3 crystals," *Materials Research Bulletin*, vol. 36, no. 15, pp. 2577–2583, 2001, ISSN: 00255408. DOI: 10.1016/S0025-5408(01)00746-2.

[47] J. Zhou, Q. Zeng, D. Lv, L. Sun, L. Niu, W. Fu, F. Liu, Z. Shen, C. Jin, and Z. Liu, "Controlled Synthesis of High-Quality Monolayered α-In2Se3 via Physical Vapor Deposition," *Nano Letters*, vol. 15, no. 10, pp. 6400–6405, 2015, ISSN: 15306992. DOI: 10.1021/acs.nanolett.5b01590.

[48] F. Ke, C. Liu, Y. Gao, J. Zhang, D. Tan, Y. Han, Y. Ma, J. Shu, W. Yang, B. Chen, H.-K. Mao, X.-J. Chen, and C. Gao, "Interlayer-glide-driven isosymmetric phase transition in compressed In 2 Se 3," *Applied Physics Letters*, vol. 104, no. 21, p. 212 102, May 2014, ISSN: 0003-6951. DOI: 10.1063/1.4879832. [Online]. Available: http://aip.scitation.org/doi/10.1063/1.4879832.

[49] K. Kambas, C. Julien, M. Jouanne, A. Likforman, and M. Guittard, "Raman Spectra of α- and γ-In2Se3," *physica status solidi (b)*, vol. 124, no. 2, K105–K108, Aug. 1984, ISSN: 03701972. DOI: 10.1002/pssb.2221240241. arXiv: arXiv:1011.1669v3. [Online]. Available: http://ebooks.cambridge.org/ref/id/CBO9781107415324A009%20http://doi.wiley.com/10.1002/pssb.2221240241.

[50] Z. Chen, K. Gacem, M. Boukhicha, J. Biscaras, and A. Shukla, "Anodic bonded 2D semiconductors: from synthesis to device fabrication," *Nanotechnology*, vol. 24, no. 41, p. 415 708, 2013, ISSN: 0957-4484. DOI: 10.1088/0957-4484/24/41/415708. [Online]. Available: http://stacks.iop.org/0957-4484/24/i=41/a=415708?key=crossref.22693abfa0c9d6a138d5b316aed61c04.

[51] O. Del Pozo-Zamudio, S. Schwarz, J. Klein, R. C. Schofield, E. A. Chekhovich, O. Ceylan, E. Margapoti, A. I. Dmitriev, G. V. Lashkarev, D. N. Borisenko, N. N. Kolesnikov, J. J. Finley, and A. I. Tartakovskii, "Photoluminescence and Raman investigation of stability of InSe and GaSe thin films," pp. 1–6, Jun. 2015. arXiv: 1506.05619. [Online]. Available: http://arxiv.org/abs/1506.05619.

[52] D. A. Bandurin, A. V. Tyurnina, G. L. Yu, A. Mishchenko, V. Zólyomi, S. V. Morozov, R. K. Kumar, R. V. Gorbachev, Z. R. Kudrynskyi, S. Pezzini, Z. D. Kovalyuk, U. Zeitler, K. S. Novoselov, A. Patanè, L. Eaves, I. V. Grigorieva, V. I. Fal'ko, A. K. Geim, and Y. Cao, "High electron mobility, quantum Hall effect and anomalous optical response in atomically thin InSe," *Nature Nanotechnology*, vol. 12, no. 3, pp. 223–227, 2016, ISSN: 1748-3387. DOI: 10.1038/nnano.2016.242. arXiv: 1608.08950. [Online]. Available: http://www.nature.com/doifinder/10.1038/nnano.2016.242.

[53] A. Politano, G. Chiarello, R. Samnakay, G. Liu, B. Gürbulak, S. Duman, A. A. Balandin, and D. W. Boukhvalov, "The influence of chemical reactivity of surface defects on ambient-stable InSe-based nanodevices," *Nanoscale*, vol. 8, no. 16, pp. 8474–8479, 2016, ISSN: 2040-3364. DOI: 10.1039/C6NR01262K. [Online]. Available: http://xlink.rsc.org/?DOI=C6NR01262K.

[54] L. Shi, Q. Zhou, Y. Zhao, Y. Ouyang, C. Ling, Q. Li, and J. Wang, "Oxidation Mechanism and Protection Strategy of Ultrathin Indium Selenide: Insight from Theory," *The Journal of Physical Chemistry Letters*, vol. 8, no. 18, pp. 4368–4373, Sep. 2017, ISSN: 1948-7185. DOI: 10.1021/acs.jpclett.7b02059. [Online]. Available: http://pubs.acs.org/doi/abs/10.1021/acs.jpclett.7b02059%20http://pubs.acs.org/doi/10.1021/acs.jpclett.7b02059.

[55] C. H. Lee, M. Kim, T. Kim, A. Kim, J. Paek, J. W. Lee, S.-Y. Choi, K. Kim, J.-B. Park, and K. Lee, "Ambient Pressure Syntheses of Size-Controlled Corundum-type In 2 O 3 Nanocubes," *Journal of the American Chemical Society*, vol. 128, no. 29, pp. 9326–9327, Jul. 2006, ISSN: 0002-7863. DOI: 10.1021/ja063227o. [Online]. Available: http://pubs.acs.org/doi/abs/10.1021/ja063227o.

[56] B. Garcia-Domene, H. M. Ortiz, O. Gomis, J. A. Sans, F. J. Manjón, A. Muñoz, P. Rodríguez-Hernández, S. N. Achary, D. Errandonea, D. Martínez-García, A. H. Romero, A. Singhal, and A. K. Tyagi, "High-pressure lattice dynamical study of bulk and nanocrystalline In 2 O 3," *Journal of Applied Physics*, vol. 112, no. 12, p. 123 511, Dec. 2012, ISSN: 0021-8979. DOI: 10.1063/1.4769747. [Online]. Available: http://aip.scitation.org/doi/10.1063/1.4769747.

[57] C. Kranert, R. Schmidt-Grund, and M. Grundmann, "Raman active phonon modes of cubic In_2O_3," *physica status solidi (RRL) - Rapid Research Letters*, vol. 8, no. 6, pp. 554–559, Jun. 2014, ISSN: 18626254. DOI: 10.1002/pssr.201409004. [Online]. Available: http://doi.wiley.com/10.1002/pssr.201409004.

[58] C. Carlone, S. Jandl, and H. R. Shanks, "Optical Phonons and Crystalline Symmetry of InSe," *physica status solidi (b)*, vol. 103, no. 1, pp. 123–130, Jan. 1981, ISSN: 03701972. DOI: 10.1002/pssb.2221030112. [Online]. Available: http://doi.wiley.com/10.1002/pssb.2221030112.

[59] J. F. Sánchez-Royo, G. Muñoz-Matutano, M. Brotons-Gisbert, J. P. Martínez-Pastor, A. Segura, A. Cantarero, R. Mata, J. Canet-Ferrer, G. Tobias, E. Canadell, J. Marqués-Hueso, and B. D. Gerardot, "Electronic structure, optical properties, and lattice dynamics in atomically thin indium selenide flakes," *Nano Research*, vol. 7, no. 10, pp. 1556–1568, 2014, ISSN: 19980000. DOI: 10.1007/s12274-014-0516-x.

[60] N. Kuroda and Y. Nishina, "Resonant raman scattering at higher m0 exciton edge in layer compound inse," *Solid State Communications*, vol. 28, no. 6, pp. 439–443, 1978, ISSN: 0038-1098. DOI: https://doi.org/10.1016/0038-1098(78)90834-7. [Online]. Available: http://www.sciencedirect.com/science/article/pii/0038109878908347.

[61] I.-H. Choi and P. Y. Yu, "Properties of phase-pure InSe films prepared by metalorganic chemical vapor deposition with a single-source precursor," *Journal of Applied Physics*, vol. 93, no. 8, pp. 4673–4677, Apr. 2003, ISSN: 0021-8979. DOI: 10.1063/1.1561584. [Online]. Available: http://aip.scitation.org/doi/10.1063/1.1561584.

[62] Q. J. Song, Q. H. Tan, X. Zhang, J. B. Wu, B. W. Sheng, Y. Wan, X. Q. Wang, L. Dai, and P.-H. Tan, "Physical origin of Davydov splitting and resonant Raman spectroscopy of Davydov components in multilayer MoTe2," *Physical Review B - Condensed Matter and Materials Physics*, vol. 93, no. 11, pp. 1–9, 2016, ISSN: 1550235X. DOI: 10.1103/PhysRevB.93.115409. arXiv: 1602.05692.

[63] G. Froehlicher, E. Lorchat, F. Fernique, C. Joshi, A. Molina-Sánchez, L. Wirtz, and S. Berciaud, "Unified Description of the Optical Phonon Modes in N -Layer MoTe 2," *Nano Letters*, vol. 15, no. 10, pp. 6481–6489, Oct. 2015, ISSN: 1530-6984. DOI: 10.1021/acs.nanolett.5b02683. [Online]. Available: http://pubs.acs.org/doi/10.1021/acs.nanolett.5b02683.

[64] R. Longuinhos and J. Ribeiro-Soares, "Ultra-weak interlayer coupling in two-dimensional gallium selenide," *Physical Chemistry Chemical Physics*, vol. 18, no. 36, pp. 25 401–25 408, 2016, ISSN: 1463-9076. DOI: 10.1039/C6CP03806A. [Online]. Available: http://dx.doi.org/10.1039/c6cp03806a%20http://xlink.rsc.org/?DOI=C6CP03806A.

[65] X. Lu, M. I. B. Utama, J. Lin, X. Luo, Y. Zhao, J. Zhang, S. T. Pantelides, W. Zhou, S. Y. Quek, and Q. Xiong, "Rapid and Nondestructive Identification of Polytypism and Stacking Sequences in Few-Layer Molybdenum Diselenide by Raman Spectroscopy," *Advanced Materials*, vol. 27, no. 30, pp. 4502–4508, 2015, ISSN: 15214095. DOI: 10.1002/adma.201501086.

[66] J.-B. Wu, X. Zhang, M. Ijaas, W.-P. Han, X.-F. Qiao, X.-L. Li, D.-S. Jiang, A. C. Ferrari, and P.-H. Tan, "Resonant Raman spectroscopy of twisted multilayer graphene," *Nature Communications*, vol. 5, p. 5309, Nov. 2014, ISSN: 2041-1723. DOI: 10.1038/ncomms6309. arXiv: 1408.6017. [Online]. Available: http://arxiv.org/abs/1408.6017%20http://dx.doi.org/10.1038/ncomms6309%20http://www.nature.com/doifinder/10.1038/ncomms6309.

[67] S. J. Haigh, A. Gholinia, R. Jalil, S. Romani, L. Britnell, D. C. Elias, K. S. Novoselov, L. A. Ponomarenko, A. K. Geim, and R. Gorbachev, "Cross-sectional imaging of individual layers and buried interfaces of graphene-based heterostructures and superlattices," *Nature Materials*, vol. 11, no. 9, pp. 764–767, Jul. 2012, ISSN: 1476-1122. DOI: 10.1038/nmat3386. [Online]. Available: https://www.nature.com/articles/nmat3386%20http://www.nature.com/doifinder/10.1038/nmat3386.

[68] Y. Takagaki, B. Jenichen, U. Jahn, M. Ramsteiner, and K. Biermann, "In 2 Se 3 films produced by Bi substitution in the hot-wall-epitaxy growth of Bi 2 Se 3 films on In-containing surfaces," *Semiconductor Science and Technology*, vol. 28, no. 11, p. 115 013, 2013, ISSN: 0268-1242. DOI: 10.1088/0268-1242/28/11/115013. [Online]. Available: http://stacks.iop.org/0268-1242/28/i=11/a=115013.

[69] O. D. Pozo-Zamudio, S. Schwarz, M. Sich, I. A. Akimov, M. Bayer, R. C. Schofield, E. A. Chekhovich, B. J. Robinson, N. D. Kay, O. V. Kolosov, A I Dmitriev, G. V. Lashkarev, D. N. Borisenko, N. N. Kolesnikov, and a. I. Tartakovskii, "Photoluminescence of two-dimensional GaTe and GaSe films," *2D Materials*, vol. 2, no. 3, p. 035 010, 2015, ISSN: 2053-1583. DOI: 10.1088/2053-1583/2/3/035010. [Online]. Available: http://stacks.iop.org/2053-1583/2/i=3/a=035010?key=crossref.98db210163d985be6abd1b89e87cd71e.

[70] O. Lundberg, J. Lu, A. Rockett, M. Edoff, and L. Stolt, "Diffusion of indium and gallium in Cu(In,Ga)Se2 thin film solar cells," *Journal of Physics and Chemistry of Solids*, vol. 64, no. 9-10, pp. 1499–1504, 2003, ISSN: 00223697. DOI: 10.1016/S0022-3697(03)00127-6.

[71] C. Dion, P. Desjardins, F. Schiettekatte, M. Chicoine, M. D. Robertson, N. Shtinkov, P. J. Poole, X. Wu, and S. Raymond, "Vacancy-mediated intermixing in InAs/InP(001) quantum dots subjected to ion implantation," *Journal of Applied Physics*, vol. 104, no. 4, p. 043 527, Aug. 2008, ISSN: 0021-8979. DOI: 10.1063/1.2970093. [Online]. Available: http://aip.scitation.org/doi/10.1063/1.2970093.

[72] K. Kambas and C. Julien, "Preparation and some optical and electrical measurements of a new phase α'-In2Se3," *Materials Research Bulletin*, vol. 17, no. 12, pp. 1573–1579, Dec. 1982, ISSN: 00255408. DOI: 10.1016/0025-5408(82)90214-8. [Online]. Available: http://linkinghub.elsevier.com/retrieve/pii/0025540882902148.

[73] I. Watanabe and T. Yamamoto, "Electrical and Structural Properties of Amorphous In-Se Films Prepared by Flash Evaporation," *Japanese Journal of Applied Physics*, vol. 24, no. Part 1, No. 10, pp. 1282–1287, Oct. 1985, ISSN: 0021-4922. DOI: 10.1143/JJAP.24.1282. [Online]. Available: http://stacks.iop.org/1347-4065/24/1282.

[74] M. Zolfaghari, K. Jain, H. Mavi, M. Balkanski, C. Julien, and A. Chevy, "Raman investigation of InSe doped with GaS," *Materials Science and Engineering: B*, vol. 38, no. 1-2, pp. 161–170, Mar. 1996, ISSN: 09215107. DOI: 10.1016/0921-5107(95)01375-X. [Online]. Available: http://dx.doi.org/10.1016/0921-5107(95)01375-X%20http://linkinghub.elsevier.com/retrieve/pii/092151079501375X.

Chapter 6

Raman Studies of Twisted $MoSe_2/WS_2$ Heterobilayers

6.1 Introduction

2-dimensional van der Waals materials offer a unique route to fabricating atomically abrupt interfaces in the building of electronic and optoelectronic devices. The epitaxial constraints are greatly relaxed in comparison to existing semiconductor technologies, allowing more diverse materials to be incorporated in devices [1], previously not directly compatible [2]. In TMD heterobilayers, the possibility of forming type II heterojunctions with spatially direct absorption but spatially indirect emission offers a new family of semiconductor heterostructures with tunable optoelectronic properties by substitution of composite layers [3]. Observation of interlayer excitons with long lifetimes $\approx$ 1.8 ns [4], and ultrafast charge transfer $\approx$ 50 fs at the interface [5], are useful in the realisation of room temperature observation of many-body effects such as exciton condensation, and comparable phenomena in coupled quantum well structures long studied in other materials systems [6], [7]. Heterobilayers also offer a further route in the exploration of vallyetronic based technologies [8].

Between different 2D materials there exist differences in the lattice constants and inter-layer bond strengths [9]; This chapter implements ultra-low-frequency Raman spectroscopy in order to characterise the interactions between layers of disparate vdW materials, through investigations of both the ULF modes and high frequency modes. The samples are produced by chemical vapour deposition of WS_2 crystals directly on to a SiO_2/Si substrate with a $\approx$ 300 nm thick SiO_2 layer. For heterostructure fabrication, $MoSe_2$ monolayers grown on c-plane sapphire substrates were transferred onto the substrate containing WS_2 flakes using PMMA-assisted transfer. They were grown in the laboratories of Hyeon Suk Shin at the Department of Energy Engineering and Department of Chemistry, Ulsan National Institute of Science and Technology (UNIST), Republic of Korea, in a process described in detail in the supplementary material of reference [10].

6.2 Results

Ultra low frequency Raman response data is shown in figures 6.2 & 6.1. For ordinary 2H (AA′-stacked) homo-bilayers in co-polarised backscattering configuration, both shear and breathing layer modes are expected. However, at the excitation wavelength of this study, 532 nm, the breathing mode is weak at 30.5 cm^{-1} in $MoSe_2$ and obscured by a resonant peak for WS_2 (fig. 6.1 (c)) though it is usually observed at 30.3 cm^{-1}. In $MoSe_2$ the shear mode is clearly observed in figure 6.2 (a) at 19.2 cm^{-1} and for WS_2 at 18.4 cm^{-1}. In the cross-polarised spectrum only the shear modes are expected at the frequencies discussed.

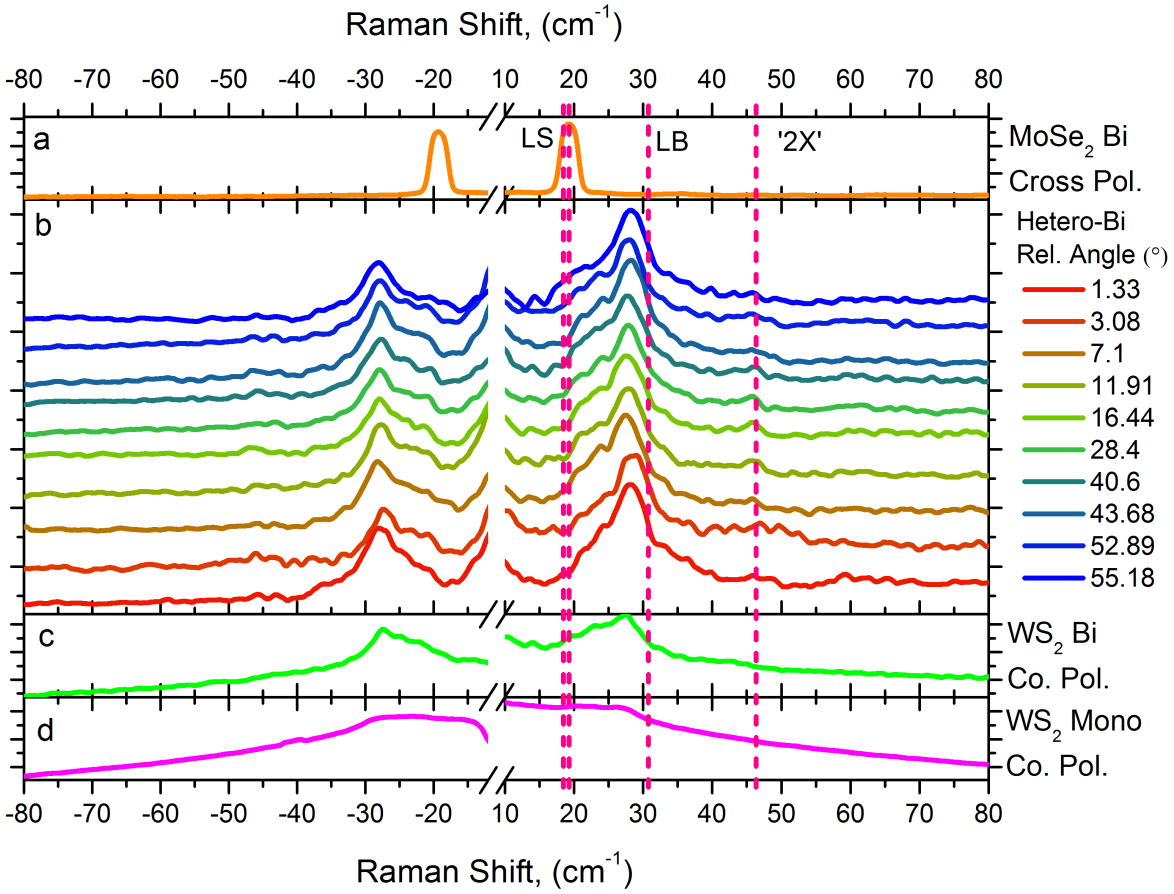

Figure 6.1: Linearly co-polarised ($\bar{z}(xx)z$) Raman responses of: (a) $MoSe_2$ bilayer showing the shear peak at approximately 18 cm^{-1}. (b) $WS_2/MoSe_2$ twisted heterobilayers with the monolayer spectrum in (d) subtracted , present is the 'Peak X' resonant feature from WS_2 and subtle shoulder modifications as a function of angle. (c) WS_2 Bilayer with 'Peak X' and the Fano resonance of the shear mode at 19 cm^{-1}. (d) WS_2 monolayer displaying unmodified 'Peak X' feature which has been subtracted from the raw data. The dashed vertical lines signify, from lower to higher wavenumber; WS_2 bi-layer shear, MoS_2 bi-layer shear, MoS_2& WS_2 bi-layer breathing, and Peak 2X.

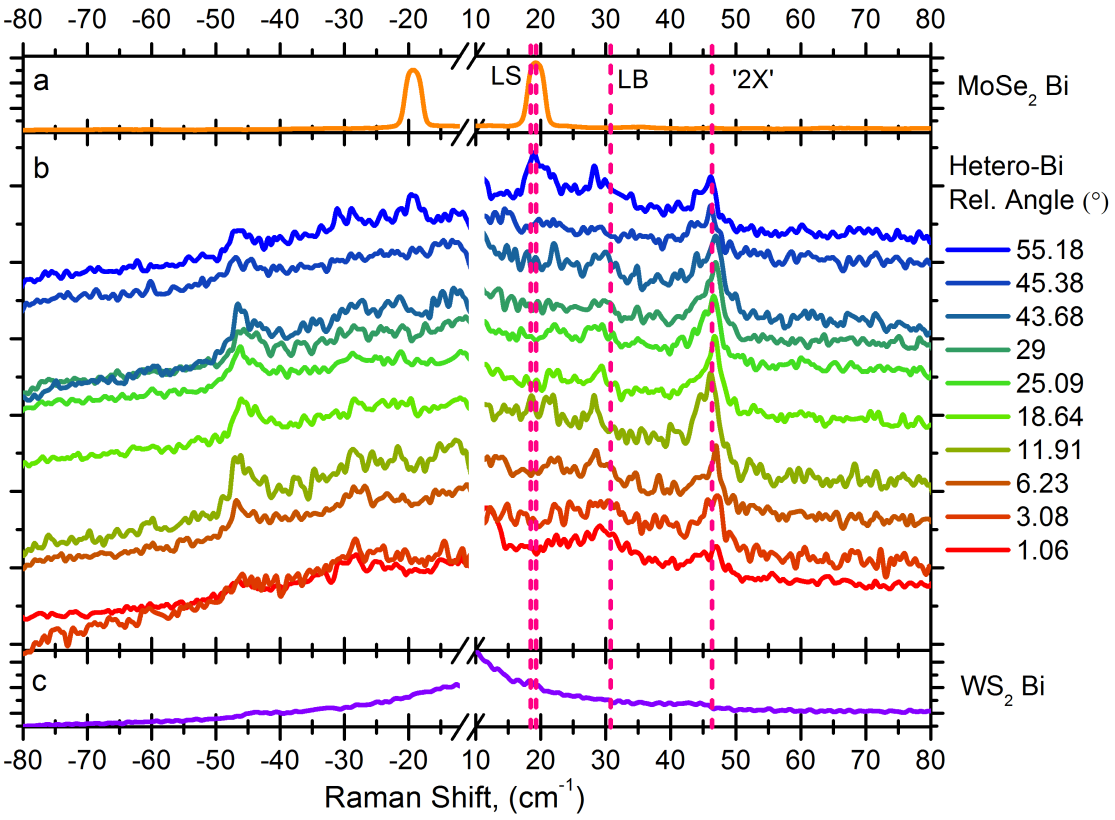

Figure 6.2: Linearly cross-polarised $(\bar{z}(xy)z)$ Raman responses of: (a) $MoSe_2$ bilayer showing the shear peak at approximately 18 cm^{-1}. (b) $WS_2/MoSe_2$ twisted heterobilayers, present is some residual of the 'Peak X' resonant feature at 28 cm^{-1} and the 2X feature at 45 cm^{-1} both from WS_2 in the 55.18° spectrum the appearance of a shear mode. (c) WS_2 bilayer with Fano resonances of the shear mode at 19 cm^{-1}, and 2X at 45 cm^{-1}. The dashed vertical lines signify, from lower to higher wavenumber; WS_2 bi-layer shear, MoS_2 bi-layer shear, MoS_2 & WS_2 bi-layer breathing, and Peak 2X.

For the co-polarised hetero-bilayer spectra in figure 6.1 (b), the WS_2 monolayer spectrum (fig. 6.1 (d)) containing only B-exciton hot-luminescence and the resonant feature at 28 cm^{-1} has been subtracted to aid the viewing of the interlayer Raman modes. The spectra are plotted from the lowest angle, 1.06° at the bottom to the largest angle 55.18° at the top, the spectra are dominated by the resonant peak at 28 cm^{-1} but subtle modifications take place close to 0° and 60°, in particular a breathing layer mode at 32 cm^{-1} in the 1.06° spectrum and a shear mode at $\approx$ 20 cm^{-1} in the 55.18° spectrum. The results of the fitting shown in figure 6.3 can be seen in figure 6.4 where a softening of (0.56±0.36) cm^{-1} is shown to occur between 0° and 60° .

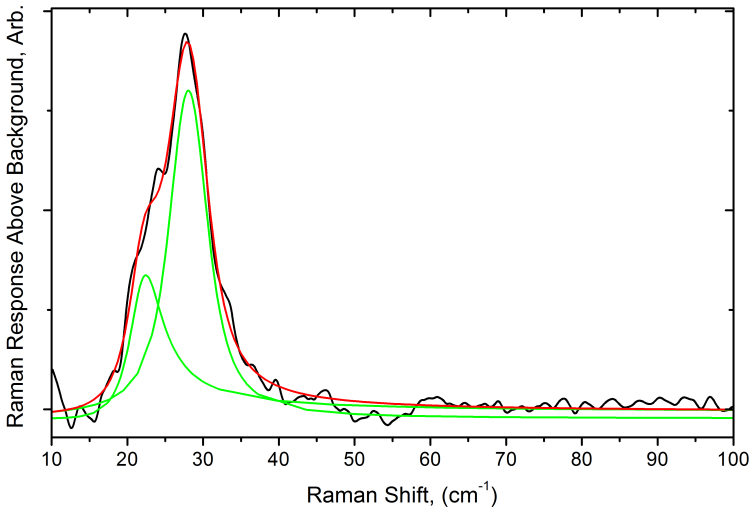

Figure 6.3: A fit example of the co-polarised low frequency Stokes spectrum of 25.09° showing the contributions of the Breit-Wigner-Fano shear mode around 22 cm^{-1} and the Voigt profile peak X at 25 cm^{-1}. Figure 6.4 shows the dependence of the peak centres on the twist angle.

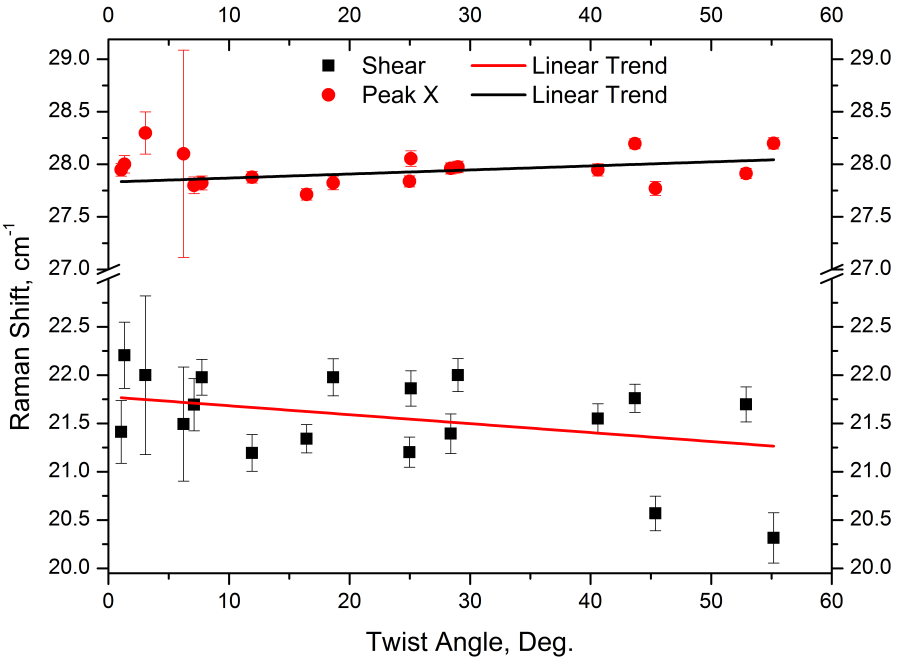

Figure 6.4: Linearly co-polarised ($\bar{z}(xx)z$) Raman responses fitting results from the peak positions extracted from figure 6.1 showing the shear mode variation as a function of angle, towards the AB stacking order at 60° there's a softening of this mode. An example fit is provided in figure 6.3.

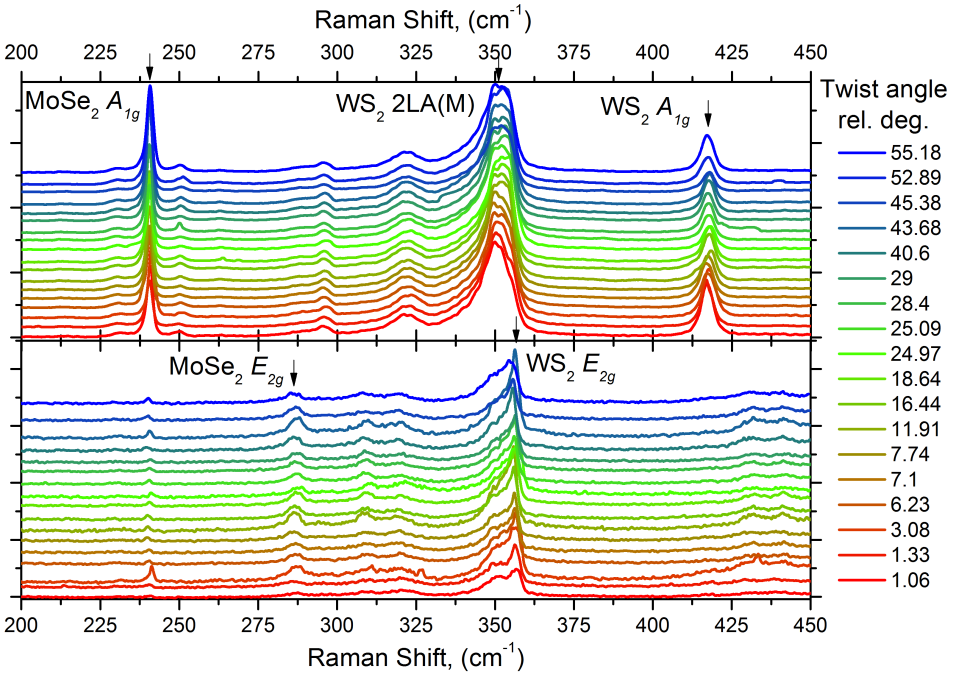

Figure 6.6: High-frequency linearly co-polarised Raman response of $WS_2/MoSe_2$ twisted Hetero-bilayers with 18 angles between 0° and 60° . Left-hand panel co-polarised $(\bar{z}(xx)z)$, right-hand panel cross-polarised $(\bar{z}(xy)z)$. Peak positions are plotted in figures 6.9 – 6.10

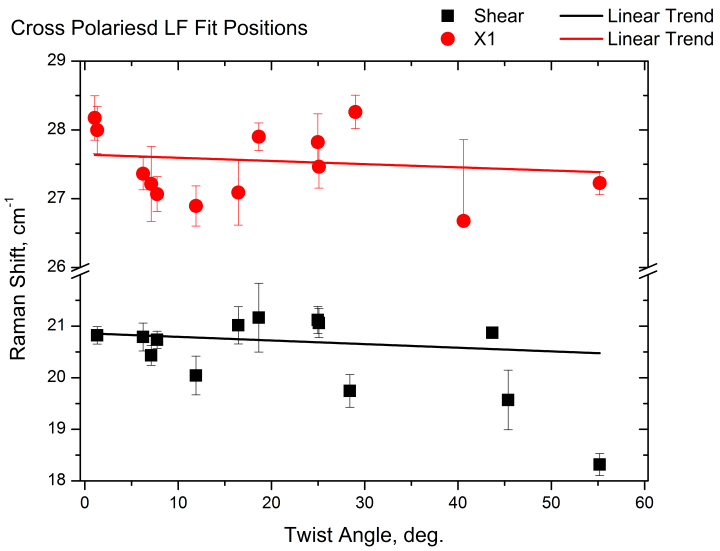

Figure 6.5: Linearly cross-polarised $(\bar{z}(xy)z)$ Raman responses of fitting results from the peak positions extracted from figure 6.2 showing the shear mode variation as a function of angle, towards the AB stacking order at 60° this mode softens.

For the cross-polarised hetero-bilayer spectra in figure 6.2(b), the spectra are plotted from the lowest angle, 1.06° at the bottom to the largest angle 55.18° at the top. The spectra show the

presence of shear modes around those expected for homo-bilayers at ≈ 20 cm^{-1}, some residual presence of peak X at 28 cm^{-1} and scattering from peak 2X at 46 cm^{-1} The results of the fitting can be seen in figure 6.5 where a softening of (0.4±0.6) cm^{-1} is shown to occur between 0° and 60° .

High frequency Raman spectra are presented in figure 6.6, the most prominent features corresponding to the principal optical intra-layer modes (A_{1g} at ≈ 240 cm^{-1} & ≈ 418 cm^{-1}, E_{2g} at ≈ 287 cm^{-1} & ≈ 256 cm^{-1}) and a resonant feature 2LA(M) at ≈ 253 cm^{-1} are labelled. The E modes appear in both polarisation configurations, co-polarised ($\bar{z}(xx)z$), and cross-polarised ($\bar{z}(xy)z$), but have much lower Raman susceptibility, and are more easily observed in cross-polarised configuration, where the A symmetric modes and 2LA(M) modes are blocked. At this scale of this figure, the differences as a function of angle are difficult to observe and the dependences are highlighted in figures 6.9 – 6.10.

Figure 6.7 shows the dependence, for WS_2, of the A_{1g} and E_{2g} modes as a function of angle, the A_{1g} mode (≈ 418 cm^{-1}) remains stable as a function of angle, whilst the E_{2g} (≈ 356 cm^{-1}) mode softens towards AB stacking at 60° the difference shows the increase in the splitting between the two modes. For the E_{2g} mode there is no significant difference between the distinct mono-, and homo-bi- layers, whilst for the A_{1g} mode there is a discrepancy of ≈ 2 cm^{-1}.

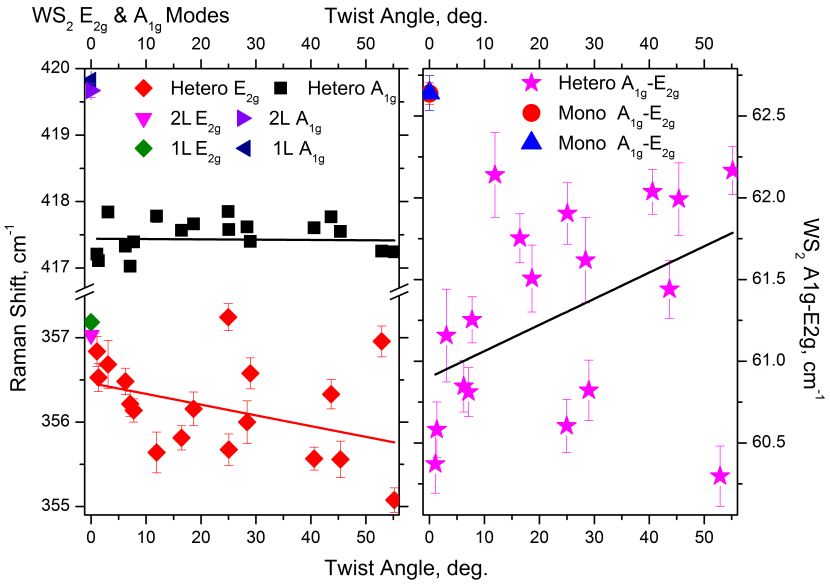

Figure 6.7: Left-hand panel; fitted peak centres for the A_{1g} and E_{2g} peaks of WS_2, with the difference plotted in the right hand panel. The peak positions for exfoliated homo-bilayers are also marked, by symbols shown in the legends.

For $MoSe_2$, the dependence of the splitting of the A_{1g} and E_{2g} modes as a function of angle is shown in Figure 6.8. The splitting can be seen to increase towards the most disordered stacking at 30° before softening back towards the value of the splitting at 0° this has been fitted with a

$\sin^2$ function, with fixed period of 60° the results of which can be seen in table 6.1.

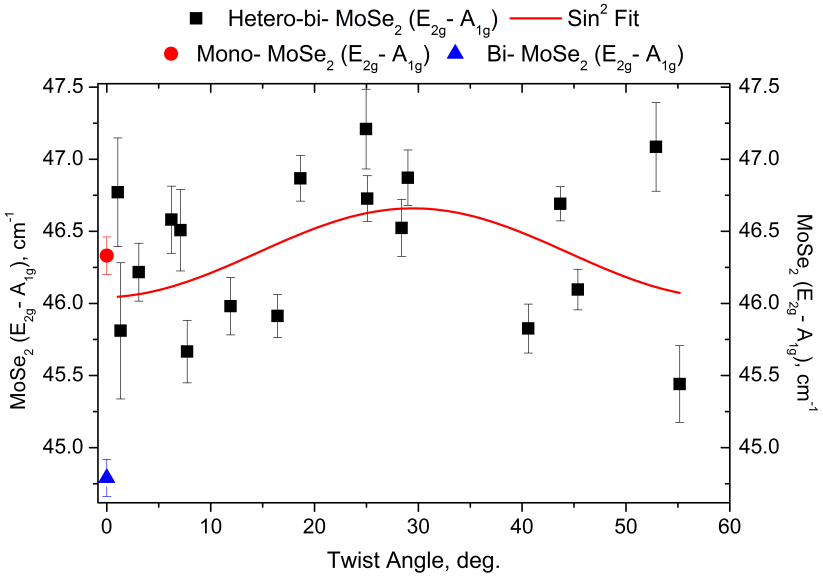

Figure 6.8: Fitted peak centre differences for the A_{1g} and E_{2g} peaks of $MoSe_2$, including exfoliated homo bi-layer peak differences.

Fit equation	$y = y_0 + A * (\sin(\pi \frac{x-x_c}{w}))^2$	
Variable	Value	Standard Error
y_0	46.0429	0.21386
x_c	119.48598	4.1763
w	60 0	0
A	0.61651	0.34235
Reduced Chi sqr.	5.39108	
Adj. R-Square	0.0681	

Table 6.1: Fit results from the Raman A_{1g}, E_{2g} peak difference *versus* twist angle data in figure 6.8.

Figure 6.9 shows the results of a 2 peak fit of the WS_2 2LA(M) resonant feature, the two components show dependences of both the peak areas and peak centres as a function of angle. The high frequency component has a stable peak centre, but the peak area grows linearly with twist angle towards the AB stacking at 60° . The lower frequency component has a reversed behaviour, where the peak area, which is the dominant component of the 2LA(M) peak, is stable, and the peak centre increases towards the AB stacking at 60° , the separation of the two components is shown as an insert in the left-hand panel, and is seen to decrease as a function of angle.

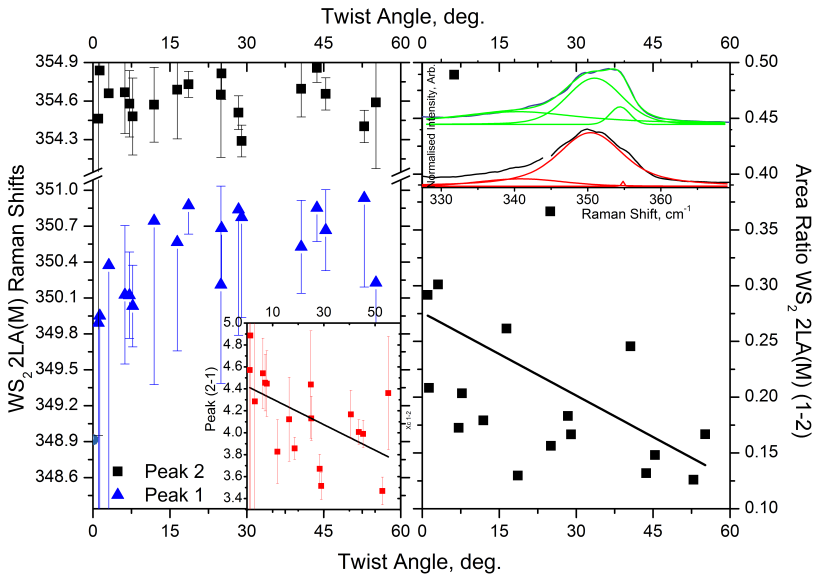

Figure 6.9: Left-hand panel; Fitted peak centres for components of the 2LA(M) peak, with the difference in the inset, $\Delta = (16 \pm 5)$ % in the peak separation between 0° and 60°. Right-hand panel shows the variation in the peak areas. Fit examples can be seen as an inset in the right-hand panel.

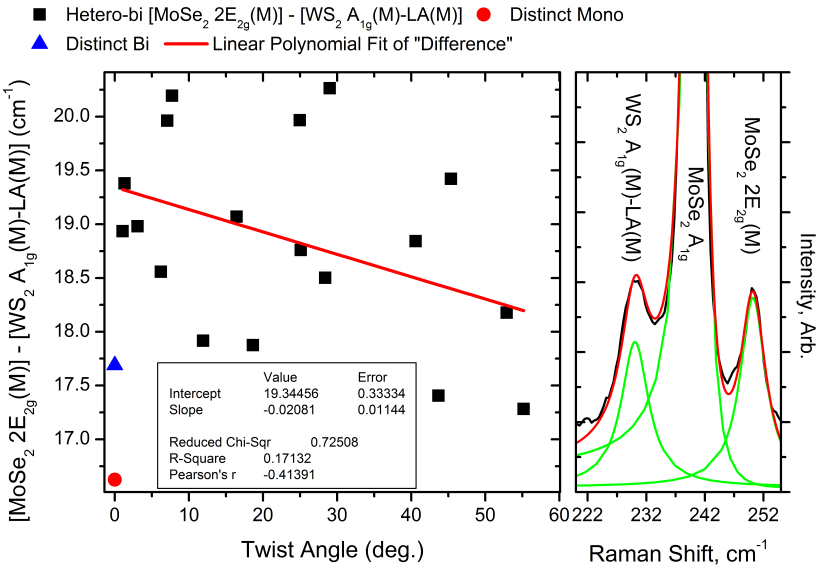

Figure 6.10: Left-hand panel shows the difference of $MoSe_2$ $2E_{2g}$(M) and WS_2 [A_{1g}−LA(M)] satellite peaks of the $MoSe_2$ A_{1g} plotted as a function of twist angle, the inset displays the linear fit parameters. The right-hand panel shows an example fit from the 29° spectrum.

Figure 6.10 shows the dependence of the splitting of the $MoSe_2$ $2E_{2g}(M)$ and WS_2 [A_{1g}-LA(M)] modes as a function of angle. The splitting of these two modes in hetero bi-layer is compared to the values for mono-layer and homo bi-layer, and is observed to decrease towards the AB stacking order at 60°.

6.3 Discussion

The inter-layer modes in figures 6.2 – 6.4 reflect quite directly the coupling between the molecular layers and are modified by different stacking orders in homo-structures [11]. For the $MoSe_2$ undistorted lattice $a = (3.288 \pm 0.001)$ Å and gap height h=(3.23 ± 0.01) Å [12]; for WS_2 it is $a = (3.1532 \pm 0.0004)$ Å and for the gap height h=(3.53 ± 0.01) Å [13]. These differences in the lattice parameter a of $\approx 4\%$ and the weak nature of the interlayer vdW forces prevents epitaxy between the materials and a moiré pattern of differing stacking orders results, with nm scale supercells even at zero twist angle [14]. Even in commensurate-lattice bilayers, twist angle produces a spatial variation in stacking order [15], thus it is expected that there should be some angle dependence of the ULF modes, whereby increased interlayer separation decreases the frequency of the observed Raman shifts, as was observed for breathing layers in other heterobilayers [16].

The breathing mode observation at 1.06° with Raman shift of 32 cm^{-1} is at a higher frequency than either of the constituent material's homo-bilayers suggests that at 1.06° the interlayer coupling is higher than might be expected. The shear mode observed at 19 cm^{-1} in the 55.18° sample is the first observed in such a large lattice-mismatched heterobilayer, and again, occurs at a frequency to suggest stronger interlayer coupling than in homo-bilayers, it is possible that there could be some additional restoring force between the two molecular layers, perhaps due to the moiré pattern supercell edges. This would be unexpected since previously it had been assumed that shear modes should be present only with alignments close to AA′ or AB, since otherwise there should be no net restoring force [17]. The fitted shear modes in figures 6.5 & 6.5 do show a decrease in frequency towards the AA stacking order at 60° which does support the hypothesis that inter-layer modes soften with increasing inter-layer separation.

In the high-frequency Raman spectrum, figure 6.6, the peaks correspond to intra-layer modes of the materials and are thus expected to be less sensitive to inter-layer coupling effects, there is, however, a previous report of such a dependence on layer number [18]. High frequency Raman modes have been fitted and the peak positions and separations plotted in figures 6.7 – 6.10.

Figure 6.7 shows that the out of plane plane A_{1g} mode of WS_2 shows no dependence on twist angle, this could perhaps be substrate effects anchoring the WS_2 layer, there is a definite discrepancy between the distinct mono-layer and the homo-bi-layer A_{1g} mode.

The WS_2 E_{2g} in-plane mode shows a definite softening towards the AB stacking order at 60° . This shift suggests that there is some in-plane modification of the lattice due to the presence of the top $MoSe_2$, and that the effective restoring force decreases towards the AB stacking order at 60° . This change in frequency with increasing twist angle is in the same direction as increasing thickness; additional layers provide an anomalous softening which was previously attributed to

modifications in long-range Coulomb interactions [18], [19], which cannot be the case in this system.

The trend for the separation of the optical phonon modes of $MoSe_2$ are shown in 6.8 with an accompanying table outlining the results of the $\sin^2$ fit of the data, table 6.1. The function $\sin^2$ was chosen as an arbitrary periodic function, there is however a basis for this choice; the angular tunneling of quantum dots is described by the same function [20]. Again, the majority of the separation of the two modes is due to the variation in the E_{2g} in plane mode, in contrast to WS_2 the AA′ (0°) and AB (60°) stacking orders have the same value, indicating that the $MoSe_2$ mono-layer is only modified in the intermediate stacking orders, where strain due to moiré patterns is greatest. Modifications of the spacing of the A_{1g} and E_{2g} modes for MoS_2 and WS_2 heterostructures predicts that the spacing is lessened in the case heterobilayers, relative to homobilayers [21], as is the case in WS_2, but not for $MoSe_2$ due to the A_{1g} mode occurring at a lower frequency than the E_{2g} mode.

Where graphene/MoS_2 heterostructures have been studied using computational methods, post-relaxation strain values were predicted as +1.9 % & -4.0 % for graphene and MoS_2, respectively [22].2 These values could be considered as the strains present in the limit of zero defects, or contamination, between materials of large lattice mismatch.

Second order modes due to resonant Raman are also modified with twist angle, in figure 6.9 the WS_2 2LA(M) peak can be decomposed into two peaks which show changes in both area and peak centre. The 2LA(M) mode scatters electrons between conduction band valleys of the Brillouin zone, and modification here suggests that band structure changes are taking place in WS_2 [23].

The two second order modes around the $MoSe_2$ A_{1g} mode; $MoSe_2$ $2E_{2g}(M)$, and WS_2 [A_{1g}-LA(M)]. Show dependence on twist angle, shown by the plot in figure 6.10 where the mode separation is plotted.

6.4 Summary

This chapter has discussed the first detailed report of polarisation resolved ultra-low-frequency (ULF) Raman studies in the $MoSe_2/WS_2$ twisted hetero-bi-layer structures on SiO_2. Difficulty in observing trends in the ULF shear and breathing layer modes, due to the presence of resonant Raman features from WS_2 has been mitigated using careful peak fitting of this region. The results of this fitting show a linear softening towards the AB stacking at 60° indicating reduced interlayer coupling, as expected from the interlayer differences of AA′ and AB stacking at 0°, and 60°, respectively.

Additional to the study of the ULF Raman spectra, high frequency modes were also studied with unprecedented detail. This data shows definite trends of these modes as a function of

twist angle, for the first time the softening of the in-plane E_{2g} mode, due to reduced inter-layer coupling towards 60° twist angle, and without the influence of long range coulomb forces from additional layers is observed in the bottom WS_2 layer. The $MoSe_2$ layer shows modification of the in-plane E_{2g} mode, but unlike the WS_2, the trend in $MoSe_2$ shows that the E_{2g} mode takes the same value at AA′ and AB stacking, and is stiffened at intermediate twist-angles. This behaviour is attributed the lack of substrate coupling in the top layer allowing strains due to moiré patterns to modify the lattice.

The second order 2LA(M) mode of WS_2 shows an unexpected dependence on the twist-angle, since this mode is related to scattering processes between conduction band valleys, it suggests a modification of this process due to the coupling between the layers.

References

[1] K. S. Novoselov, D. Jiang, F. Schedin, T. J. Booth, V. V. Khotkevich, S. V. Morozov, and A. K. Geim, "Two-dimensional atomic crystals," *Proceedings of the National Academy of Sciences*, vol. 102, no. 30, pp. 10 451–10 453, Jul. 2005, ISSN: 0027-8424. DOI: 10.1073/pnas.0502848102. [Online]. Available: http://www.pubmedcentral.nih.gov/articlerender.fcgi?artid=1180777%7B%5C&%7Dtool=pmcentrez%7B%5C&%7Drendertype=abstract%20http://www.pnas.org/cgi/doi/10.1073/pnas.0502848102.

[2] A. K. Geim and I. V. Grigorieva, "Van der Waals heterostructures.," *Nature*, vol. 499, no. 7459, pp. 419–25, Jul. 2013, ISSN: 1476-4687. DOI: 10.1038/nature12385. [Online]. Available: http://www.ncbi.nlm.nih.gov/pubmed/23887427.

[3] E. V. Calman, C. J. Dorow, M. M. Fogler, L. V. Butov, S. Hu, A. Mishchenko, and A. K. Geim, "Control of excitons in multi-layer van der Waals heterostructures," *Applied Physics Letters*, vol. 108, no. 10, p. 101 901, Mar. 2016, ISSN: 0003-6951. DOI: 10.1063/1.4943204. arXiv: 1510.04410. [Online]. Available: http://aip.scitation.org/doi/10.1063/1.4943204.

[4] H. Fang, C. Battaglia, C. Carraro, S. Nemsak, B. Ozdol, J. S. Kang, H. A. Bechtel, S. B. Desai, F. Kronast, A. A. Unal, G. Conti, C. Conlon, G. K. Palsson, M. C. Martin, A. M. Minor, C. S. Fadley, E. Yablonovitch, R. Maboudian, and A. Javey, "Strong interlayer coupling in van der Waals heterostructures built from single-layer chalcogenides," *Proceedings of the National Academy of Sciences*, vol. 111, no. 17, pp. 6198–6202, 2014, ISSN: 0027-8424. DOI: 10.1073/pnas.1405435111. arXiv: 1403.3754. [Online]. Available: http://www.pnas.org/cgi/doi/10.1073/pnas.1405435111.

[5] X. Zhu, N. R. Monahan, Z. Gong, H. Zhu, K. W. Williams, and C. A. Nelson, "Charge Transfer Excitons at van der Waals Interfaces," *Journal of the American Chemical Society*, vol. 137, no. 26, pp. 8313–8320, Jul. 2015, ISSN: 0002-7863. DOI: 10.1021/jacs.5b03141. [Online]. Available: http://pubs.acs.org/doi/10.1021/jacs.5b03141.

[6] A. M. Fox, D. A. B. Miller, G. Livescu, J. E. Cunningham, and W. Y. Jan, "Excitonic effects in coupled quantum wells," *Phys. Rev. B*, vol. 44, pp. 6231–6242, 12 Sep. 1991. DOI: 10.1103/PhysRevB.44.6231. [Online]. Available: https://link.aps.org/doi/10.1103/PhysRevB.44.6231.

[7] M. M. Fogler, L. V. Butov, and K. S. Novoselov, "High-temperature superfluidity with indirect excitons in van der Waals heterostructures.," *Nature communications*, vol. 5, no. May, p. 4555, 2014, ISSN: 2041-1723. DOI: 10.1038/ncomms5555. arXiv: 1404.1418. [Online]. Available: http://www.ncbi.nlm.nih.gov/pubmed/25065343.

[8] H. Yu, Y. Wang, Q. Tong, X. Xu, and W. Yao, "Anomalous Light Cones and Valley Optical Selection Rules of Interlayer Excitons in Twisted Heterobilayers," *Physical Review Letters*, vol. 115, no. 18, p. 187 002, Oct. 2015, ISSN: 0031-9007. DOI: 10.1103/PhysRevLett.115.187002. arXiv: 1504.01215. [Online]. Available: https://link.aps.org/doi/10.1103/PhysRevLett.115.187002.

[9] J. Wilson and A. Yoffe, "The transition metal dichalcogenides discussion and interpretation of the observed optical, electrical and structural properties," *Advances in Physics*, no. May 2012, pp. 37–41, 1969. DOI: http://dx.doi.org/10.1080/00018736900101307. [Online]. Available: http://www.tandfonline.com/doi/abs/10.1080/00018736900101307.

[10] E. M. Alexeev, A. Catanzaro, O. V. Skrypka, P. K. Nayak, S. Ahn, S. Pak, J. Lee, J. I. Sohn, K. S. Novoselov, H. S. Shin, and A. I. Tartakovskii, "Imaging of Interlayer Coupling in van der Waals Heterostructures Using a Bright-Field Optical Microscope," *Nano Letters*, vol. 17, no. 9, pp. 5342–5349, Sep. 2017, ISSN: 1530-6984. DOI: 10.1021/acs.nanolett.7b01763. arXiv: 1612.07969. [Online]. Available: http://pubs.acs.org/doi/10.1021/acs.nanolett.7b01763.

[11] J.-U. Lee, K. Kim, S. Han, G. H. Ryu, Z. Lee, and H. Cheong, "Raman Signatures of Polytypism in Molybdenum Disulfide," *ACS Nano*, vol. 10, no. 2, pp. 1948–1953, Feb. 2016, ISSN: 1936-0851. DOI: 10.1021/acsnano.5b05831. [Online]. Available: http://dx.doi.org/10.1021/acsnano.5b05831%20http://pubs.acs.org/doi/10.1021/acsnano.5b05831.

[12] P. B. James and M. T. Lavik, "The crystal structure of $MoSe_2$," *Acta Crystallographica*, vol. 16, no. 11, pp. 1183–1183, Nov. 1963, ISSN: 0365110X. DOI: 10.1107/S0365110X6300311X. [Online]. Available: http://scripts.iucr.org/cgi-bin/paper?S0365110X6300311X.

[13] W. Schutte, J. De Boer, and F. Jellinek, "Crystal structures of tungsten disulfide and diselenide," *Journal of Solid State Chemistry*, vol. 70, no. 2, pp. 207–209, Oct. 1987, ISSN: 00224596. DOI: 10.1016/0022-4596(87)90057-0. [Online]. Available: http://linkinghub.elsevier.com/retrieve/pii/0022459687900570.

[14] J. Kang, J. Li, S.-S. Li, J.-B. Xia, and L.-W. Wang, "Electronic Structural Moiré Pattern Effects on MoS 2 /MoSe 2 2D Heterostructures," *Nano Letters*, vol. 13, no. 11, pp. 5485–5490, Nov. 2013, ISSN: 1530-6984. DOI: 10.1021/nl4030648. [Online]. Available: http://pubs.acs.org/doi/abs/10.1021/nl4030648.

[15] S. Huang, L. Liang, X. Ling, A. A. Puretzky, D. B. Geohegan, B. G. Sumpter, J. Kong, V. Meunier, and M. S. Dresselhaus, "Low-Frequency Interlayer Raman Modes to Probe Interface of Twisted Bilayer MoS 2," *Nano Letters*, vol. 16, no. 2, pp. 1435–1444, Feb.

2016, ISSN: 1530-6984. DOI: 10.1021/acs.nanolett.5b05015. [Online]. Available: http://pubs.acs.org/doi/10.1021/acs.nanolett.5b05015.

[16] C. H. Lui, Z. Ye, C. Ji, K.-C. Chiu, C.-T. Chou, T. I. Andersen, C. Means-Shively, H. Anderson, J.-M. Wu, T. Kidd, Y.-H. Lee, and R. He, "Observation of interlayer phonon modes in van der Waals heterostructures," *Physical Review B*, vol. 91, no. 16, p. 165 403, Apr. 2015, ISSN: 1098-0121. DOI: 10.1103/PhysRevB.91.165403. arXiv: 1410.4224. [Online]. Available: https://link.aps.org/doi/10.1103/PhysRevB.91.165403.

[17] J. Zhang, J. Wang, P. Chen, Y. Sun, S. Wu, Z. Jia, X. Lu, H. Yu, W. Chen, J. Zhu, G. Xie, R. Yang, D. Shi, X. Xu, J. Xiang, K. Liu, and G. Zhang, "Observation of Strong Interlayer Coupling in MoS 2 /WS 2 Heterostructures," *Advanced Materials*, vol. 28, no. 10, pp. 1950–1956, Mar. 2016, ISSN: 09359648. DOI: 10.1002/adma.201504631. [Online]. Available: http://www.ncbi.nlm.nih.gov/pubmed/26708256%7B%5C%%7D5Cnhttp://onlinelibrary.wiley.com.gaelnomade.ujf-grenoble.fr/doi/10.1002/adma.201504631/full%20http://doi.wiley.com/10.1002/adma.201504631.

[18] C. Lee, H. Yan, L. E. Brus, T. F. Heinz, J. Hone, and S. Ryu, "Anomalous Lattice Vibrations of Single- and Few-Layer MoS 2," *ACS Nano*, vol. 4, no. 5, pp. 2695–2700, May 2010, ISSN: 1936-0851. DOI: 10.1021/nn1003937. arXiv: 1005.2509. [Online]. Available: http://pubs.acs.org/doi/abs/10.1021/nn1003937.

[19] K.-G. Zhou, F. Withers, Y. Cao, S. Hu, G. Yu, and C. Casiraghi, "Raman Modes of MoS 2 Used as Fingerprint of van der Waals Interactions in 2-D Crystal-Based Heterostructures," *ACS Nano*, vol. 8, no. 10, pp. 9914–9924, Oct. 2014, ISSN: 1936-0851. DOI: 10.1021/nn5042703. [Online]. Available: http://pubs.acs.org/doi/abs/10.1021/nn5042703%20http://pubs.acs.org/doi/10.1021/nn5042703.

[20] Y.-Q. Zhou, R.-Q. Wang, B. Wang, and D. Y. Xing, "Angle-dependent tunneling through quantum dots coupled to noncollinearly oriented magnetic leads and subject to magnetic fields," *Physical Review B*, vol. 76, no. 7, p. 075 343, Aug. 2007, ISSN: 1098-0121. DOI: 10.1103/PhysRevB.76.075343. [Online]. Available: https://link.aps.org/doi/10.1103/PhysRevB.76.075343.

[21] L. Liang and V. Meunier, "First-principles Raman spectra of MoS_2, WS_2 and their heterostructures," *Nanoscale*, vol. 6, no. 10, p. 5394, 2014, ISSN: 2040-3364. DOI: 10.1039/c3nr06906k. [Online]. Available: http://www.ncbi.nlm.nih.gov/pubmed/24710269%20http://xlink.rsc.org/?DOI=c3nr06906k.

[22] N. B. Le, T. D. Huan, and L. M. Woods, "Interlayer Interactions in van der Waals Heterostructures: Electron and Phonon Properties," *ACS Applied Materials and Interfaces*, vol. 8, no. 9, pp. 6286–6292, 2016, ISSN: 19448252. DOI: 10.1021/acsami.6b00285.

[23] A. Berkdemir, H. R. Gutiérrez, A. R. Botello-Méndez, N. Perea-López, A. L. Elías, C.-I. Chia, B. Wang, V. H. Crespi, F. López-Urías, J.-C. Charlier, H. Terrones, and M. Terrones, "Identification of individual and few layers of WS_2 using Raman Spectroscopy," *Scientific*

Reports, vol. 3, no. 1, p. 1755, Dec. 2013, ISSN: 2045-2322. DOI: 10.1038/srep01755. [Online]. Available: http://www.nature.com/doifinder/10.1038/srep01755%20http://www.nature.com/articles/srep01755.

Chapter 7

Conclusion

7.1 Results

This thesis presents the results of optical characterisation of 2-dimensional van der Waals materials by means of ultra low frequency Raman spectroscopy. Transition metal dichalocgenides, the III–VI metal chalcogenides InSe and In_2Se_3 have been studied in their basic exfoliated forms, and structures synthesised by means of chemical growth. Raman studies of these materials can be concluded as follows:

1. $Mo_xW_{(1-x)}S_2$ alloys have been demonstrated to provide a means of tuning the bandgap and band-offsets, following the previously established, empirically derived, quadratic dependence. The spin orbit coupling follows the same behaviour, demonstrating bowing not previously observed in transition metal sulphide compounds in previous studies. The Indirect exciton in trilayer samples is also observed to follow this trend.

   High frequency Raman studies were conducted with unprecedented resolution and accuracy, allowing observation of bi-modal behaviour of both the A_{1g} and E_{2g} lattice normal modes, where previously study only recognised this in the E_{2g} mode, using a modified random element iso-displacemnt (MREI) model. Non-linearity is observed in the peak frequencies of the two components of a given lattice normal mode, this is explained by the presence of strain due to the mixing of molybdenum and tungsten atoms for which the differing electronegativities alter the metal–chalcogen bond lengths and strengths, and reduced phonon correlation lengths as a consequence of the increased disorder.

   The relative intensities of the A_{1g} mode were shown to have sigmoidal dependence on the molybdenum concentration demonstrating the instability of the phonon modes at high entropy.

   Ultra low frequency Raman uncovered new evidence for the study of the resonance 'Peak X' – that with increasing [Mo] the peak tunes away from its value in MoS_2 and

persists as the hot-luminescence from the B-exciton resonance reduces as the B-exciton tunes away from the excitation energy.

In bilayer and trilayer samples the shear and breathing interlayer modes were shown to tune according to the square-density of the molecular layer, indicating that the interlayer coupling is dominated by the chalcogen–chalcogen interaction.

2. Indium-selenium compounds represent a frontier in the 2 dimensional materials community, and have undergone relatively little scrutiny in comparison to other materials such as Graphene and TMDs. The first ultra low frequency Raman spectra of these materials are presented in this thesis and observation of behaviours similar to those made in TMDs are made.

   In PDMS exfoliated InSe flakes the presence of interlayer shear modes, and redshift of the A^1_{1g} phonon mode with reduction in layer number is demonstrated. The InSe flakes manifest Davydov peaks for the E_{1g} mode, owing to the much lower frequency in comparison to TMDs, allowing the Davydov peak to be resolved in spite of the weaker interlayer coupling. In InSe flakes of thicknesses above bilayer, the weak coupling allows the existence of high order polytypes with stacking sequences greater than 2H and 3R observed in TMDs, multiple polytypes were observed in flakes up to bulk thickness.

   Hexagonal boron nitride encapsulated InSe fabricated in an argon atmosphere glovebox by boron nitride pickup was expected to manifest the same behaviour as the PDMS exfoliated InSe, without and markers of disorder in the Raman spectrum. There were, however, discrepancies in the spectra, first of which was the lack of softening of the A^1_{1g} mode with decreasing thickness, this was attributed to the additional thickness of the hBN encapsulation providing additional coupling, causing the encapsulated InSe intralayer modes to behave as in bulk samples. In the ultra low frequency, again only shear modes were observed, with the 4 nm flake assigned as trilayer manifesting 3R, rather than mixed 2H/3R stacking order, and the 30 nm flake demonstrating mixed polytypism.

   The most unexpected finding was that in spite of the use of the cleanest deterministic vdW transfer method, hBN pickup in inert atmosphere, the structures were seen to have the rotational Raman modes of air (O_2 & N_2) present, with intensities comparable to those of the InSe crystalline normal modes in the thinnest 3.5 nm sample.

   The AFM micrographs show contamination bubbles, which have previously been shown to be predominately hydrocarbon residues, the exact reason for their presence is unknown, but it is possible that they are adsorbed when the bulk materials are transported under ambient conditions.

   In_2Se_3 chemically grown on GaSe, was revealed to comprise multiple In_2Se_3 phases - α, β, & γ, and InSe, with dependence on the region of GaSe flake on which the growth

occurred. Raman modes from the GaSe substrate flakes were not detected at any positions on the flakes, suggesting a significant substitution of gallium by indium. With this knowledge, the substrate GaSe could be engineered to target a particular growth of In_2Se_3 or InSe.

Further to the as-grown In_2Se_3 phases, it was seen that a phase change from $\beta \rightarrow \alpha$ occurred under moderate laser power for an extended time under vacuum at room temperature. Such a phase change has not been previously reported and occurs in a direction opposite to the thermally driven phase change in In_2Se_3, inviting the question of an alternative mechanism.

3. In twisted $MoSe_2/WS_2$ heterobilayers, the study revealed that besides the resonant 'Peak X' and 2X, from monolayer WS_2 there exist interlayer Raman modes due to the coupling between non-lattice-matched 2 dimensional van der Waals materials. The observed interlayer modes were exclusively shear modes due to the linearly co-polarised Raman spectra being dominated by Peak X, they were shown to tune in frequency with twist-angle indicating variations in the interlayer distance and coupling. Additionally, high frequency modes were studied in detail for the first time, and were shown to exhibit small tunings in their frequencies as a function of twist-angle.

7.2 Outlook

The field of 2-dimensional materials offers fecund ground for the advancement of condensed matter physics, and possible routes to develop technologically novel devices for the betterment of society. The 2D materials field has grown to the extent that results are generated at rates orders of magnitude greater now, as compared with those at the outset of this work.

It is encouraging that the prototypical 2D material, graphene, regularly features in the media's reports of approaching technologies, one of the first realisations of the material's promise [1]. Noting that not far behind are the semiconducting TMDs which offer a novel route to building semiconductor devices, with the suggestion of high performance flexible electronics.

Considering more blue-sky concepts, 2D materials perhaps offer more exciting prospects. Multiple many body phenomena have already been observed, allowing greater insight into the consequences of fundamental physics, the promise of generating synthetic superconductors is one of great personal interest. The discovery of 2D superconductivity allows new routes to understanding the nature of the superconducting state [2], building novel superconductors with liquid N_2 temperatures or even room temperatures would result in a revolution in infrastructures and the possibility of superconducting sensors in consumer electronics.

Specific questions that this work invites are:

- $Mo_xW_{(1-x)}S_2$ alloys are conclusively studied in this work and the most prominent remaining question is that of 'Peak X'. The observation that 'Peak X' tunes in frequency from its

value in WS_2 with increasing [Mo] away from its value in MoS_2 was unexpected. A study required to elucidate this effect would be with the implementation of a spectrometer stage to filter out a tunable laser used to resonantly excite the exciton complexes in each alloy composition, and observing the behaviour of 'Peak X'. The temperature dependence of 'Peak X' might also be of some interest; observing the Stokes:anti-Stokes ratio of the resonance peaks in comparison to the lattice phonon peak S:aS ratio might give important information as to the mechanism behind its Raman activity.

- Indium-selenium compounds offer a promising route to novel publications, given their relatively low scrutiny they've experienced in comparison with TMDs thus far. From the perspective of this work and the specifics of the ultra low frequency Raman, an obvious question would be on the nature of the $\alpha \rightarrow \alpha'$ transition in In_2Se_3 which takes place at $-125°C$, and how this impacts the ferroelectric effect in this material's monolayer. How this transition compares to the Pierls transition in the charge density wave conductor $NbSe_2$, and the recently discovered Excitonic condensate phase in 1T-$TiSe_2$ [3] would be an exciting route to understanding the role of electron phonon coupling in low dimensional condensed matter physics. In principle the experiment could be quite simple; at relatively easily obtainable cryogenic temperatures, from bulk to exfoliated monolayer α-In_2Se_3, the transition from $\alpha \rightarrow \alpha'$ should be detectable by Raman spectroscopy, owing to the role of an (as yet unspecified) phonon mode responsible for transition.

- In twisted $MoSe_2/WS_2$ heterobilayers non-resonant excitation to avoid hot luminescence and 'Peak X' contribution from the WS_2 layer would allow a clearer picture of the interlayer modes that is possible using resonant excitation. Study of other stacks would be a more general continuation of this work, following the tunable photoluminescence response in $Mo_xW_{(1-x)}S_2$ alloys, the use of ferroelectric α-In_2Se_3 molecular layers has been demonstrated as a route to tuning the dielectric environment, Raman studies of these structures and the dependence on alignment angle would be an interesting route of study.

References

[1] S. Jung-a, *Samsung hails 'graphene ball' battery success*, 2017. [Online]. Available: https://www.ft.com/content/5a6693f0-d349-11e7-8c9a-d9c0a5c8d5c9 (visited on 11/29/2017).

[2] Y. Saito, T. Nojima, and Y. Iwasa, "Highly crystalline 2D superconductors," *Nature Reviews Materials*, vol. 2, no. 1, p. 16094, Dec. 2016, ISSN: 2058-8437. DOI: 10.1038/natrevmats.2016.94. [Online]. Available: http://dx.doi.org/10.1038/natrevmats.2016.94%20http://www.nature.com/articles/natrevmats201694.

[3] A. Kogar, M. S. Rak, S. Vig, A. A. Husain, F. Flicker, Y. I. Joe, L. Venema, G. J. MacDougall, T. C. Chiang, E. Fradkin, J. van Wezel, and P. Abbamonte, "Signatures of exciton condensation in a transition metal dichalcogenide," *Science*, vol. 358, no. 6368, pp. 1314–1317, Dec. 2017, ISSN: 0036-8075. DOI: 10.1126/science.aam6432. [Online]. Available: http://www.sciencemag.org/lookup/doi/10.1126/science.aam6432.